

THE EFFECTS OF ELECTROSTATIC CHARGE ON PARTICLE FLOWS AND
DEPOSITION

By

PONGPUMIN POOM BUNCHATHEERAVATE

A DISSERTATION PRESENTED TO THE GRADUATE SCHOOL
OF THE UNIVERSITY OF FLORIDA IN PARTIAL FULFILLMENT
OF THE REQUIREMENTS FOR THE DEGREE OF
DOCTOR OF PHILOSOPHY

UNIVERSITY OF FLORIDA

2012

© 2012 Pongpumin Poom Bunchatheeravate

To my family and friends for their support

ACKNOWLEDGMENTS

I thank my advisor, Dr. Jennifer Curtis for her constant guidance, supervision, and encouragement throughout the year. Under her guidance I had gain new prospective on my research. Thank you to Dr. Scott Brown for all his input and help over the year. Those input were significant in my progress. Thank you to Dr. Shuji Matsusaka for letting me into his group at the Kyoto University in Japan. During my stay in Japan I lad gain many viewpoints that would not had been possible elsewhere. Thank you to Dr. Jan Marijnissen and Dr. Caner Yurteri for their constant guidance of electrospraying technique. And lastly thank you to all my friends, co-worker, and family members who had supported me. And lastly the work presented in this manuscript is made possible through the funding from NSF-PIRE, project number NSF OISE 0968313, Grant-in-Aid for Scientific Research (B) (No. 23360341) from the Japan Society for the Promotion of Science, and the Department of Education's GAANN fellowship program.

TABLE OF CONTENTS

	<u>page</u>
ACKNOWLEDGMENTS.....	4
LIST OF TABLES.....	8
LIST OF FIGURES.....	10
ABSTRACT.....	14
CHAPTER	
1 INTRODUCTION.....	16
Particle Charging During Transport.....	17
Particle Deposition to Pulmonary Airways.....	19
2 PREDICTION OF PARTICLE CHARGING IN A DILUTE PNEUMATIC CONVEYING SYSTEM.....	20
Background.....	20
Theory.....	23
Charge Transfer Model for Metal-Metal Systems.....	23
Charge Transfer Model for Metal-Insulator and Insulator-Insulator Systems....	25
Charge Transfer Model for Repeated Impacts.....	26
Experiments.....	27
Experimental Setup.....	27
Short Pipe Experimentation with Varying Initial Charge.....	29
Validation Experiments with Longer Pipes.....	30
Particles and Pipes.....	30
Results and Discussion.....	30
Varying Initial Charge in the Particle Charger.....	30
Short Pipe Experimentation with Varying Initial Charge.....	31
Predicting Particle Charging using Stair-Stepping Procedure.....	32
Predicting Particle Charging using the Semi-Theoretical Equations.....	32
Technique Validation.....	34
Summary.....	34
3 CHARGE PREDICTION USING COMPUTATIONAL FLUIDS DYNAMICS (CFD) SIMULATION.....	46
Background.....	46
Model Description.....	47
Governing Equations.....	47
Drag Models.....	47

Gas Phase Stress	48
Solid Stress	49
Turbulence Interaction.....	50
Computer Simulation.....	51
Determining Collision Number.....	51
Experiments.....	53
Simulation	53
Results and Discussion.....	54
Particle-Wall Collision.....	54
Determining nT, O^*	56
Comparisons to Experimental Results	56
Expanding the Prediction Model	57
Scale Up the Pipe-Line.....	57
Monitoring the Environmental Condition.....	58
Scaling the Particle Size.....	59
Accounting for the Complex Flow Geometry	60
Summary	61
4 DEPOSITION OF CHARGED PARTICLES IN BIFURCATING AIRWAY	69
Background.....	69
Electrospray Technique.....	71
Production of Charged, Spherical Particles	71
Production of Charged, Non-Spherical Particles.....	73
Near Infrared (NIR) Spectroscopy	74
Experiments.....	74
Bifurcating Model.....	74
Generation of Spherical Particles	75
Generation of Non-Spherical Particles	76
Experimental Setup.....	77
Characterizing Neutrally-Charged Particles.....	79
Particle Deposition	80
NIR Imaging.....	80
Results.....	82
Deposition of “Neutral” Spheres	82
Deposition of Positively-Charged Spheres	83
Deposition of Non-Spherical Particles	84
Concentration of the Deposited Particles	85
Summary	86
5 DEPOSITION OF NON-SPHERICAL PARTICLES IN BIFURCATING AIRWAY..	106
Background.....	106
Deposition Efficiency	108
Deposition Mechanisms	109
Particle Characterization	111
Boundary Layer	112

Experiments.....	112
Particle Characterization	112
Airway Model.....	113
Particle Deposition	113
Quantifying the Deposition	114
Results.....	115
Particle Characteristics.....	115
Particle Deposition	116
Deposition Model.....	117
Model Validation.....	120
Summary	121
6 CONCLUSION AND RECOMMENDATION.....	137
Particle Charging During Transport	137
Particle Deposition in Pulmonary Airways.....	138
Use of NIR Fluorescence	138
Effect of Electrostatic charge on Particle Deposition	139
Deposition of Charged Spheres	139
Deposition of Charged, Rod-Shaped Particles	139
Deposition of Charged Hollow, Balloon-Shaped Particles	139
Future Experiments.....	140
Deposition of Non-Spherical Particles	140
Future applications to simulation	141
 APPENDIX	
A EFFECT OF V_{EX} ON THE CONTACT POTENTIAL.....	143
B RAW DATA FOR PARTICLE CHARGING EXPERIMENT	146
C PARAMETRIC STUDY	156
D ADDITIONAL COMPARISON FOR CHARGE MODEL VALIDATION.....	169
E ADDITIONAL IVIS IMAGES FOR DIFFERENT PARTICLE SHAPE	187
LIST OF REFERENCES	195
BIOGRAPHICAL SKETCH.....	203

LIST OF TABLES

<u>Table</u>		<u>page</u>
2-1	Characteristics of particles used in the experiment	36
2-2	Characteristic of pipes used in the experiment	36
2-3	Characteristic values for each particle in 1-m pipe	37
3-1	Term used in the turbulence and solid stress model	62
3-2	Inputs and outputs for the simulation	63
3-3	Air flow in each type of pipe at each pressure setting.....	63
3-4	Characteristics of particles used in the experiment	64
3-5	Characteristic of pipes used in the experiment	64
3-6	Characteristic values for each particle in 1-m pipe	64
4-1	Dimension of the bifurcating airway model	88
4-2	Electrospray solution properties	88
4-3	Mass percent deposition of particles	88
4-4	The average deposition concentration of particles	89
5-1	Dimension of the bifurcating airway model	122
5-2	Flow parameter in the bifurcating airway model	122
5-3	Characterization for each type of particle	122
5-4	The percentage of deposition in each generation of the airway model.....	123
5-5	Deposition parameter for each particle in each airway	124
5-6	Contribution of deposition from each mechanism.....	125
B-1	Raw data for borosilicate particle-copper pipe system	146
B-2	Raw data for borosilicate particle-stainless steel pipe system.....	146
B-3	Raw data for borosilicate particle-natural glass pipe system	147
B-4	Raw data for borosilicate particle-pyrex pipe system.....	147

B-5	Raw data for soda lime particle-copper pipe system	148
B-6	Raw data for soda lime particle-stainless steel pipe system.....	148
B-7	Raw data for soda lime particle-natural glass pipe system	149
B-8	Raw data for soda lime particle-pyrex pipe system	149
B-9	Raw data for PMMA particle-copper pipe system.....	150
B-10	Raw data for PMMA particle-stainless steel pipe system	150
B-11	Raw data for PMMA particle-natural glass pipe system	151
B-12	Raw data for PMMA particle-pyrex pipe system	151
B-13	Raw data for crushed soda lime particle-copper pipe system	152
B-14	Raw data for crushed soda lime particle-copper pipe system	152
B-15	Raw data for crushed soda lime particle-copper pipe system	153
B-16	Raw data for crushed soda lime particle-copper pipe system	153
B-17	Raw data for JSC-1A particle-copper pipe system	154
B-18	Raw data for JSC-1A particle-Stainless steel pipe system	154
B-19	Raw data for JSC-1A particle-natural glass pipe system.....	155
B-20	Raw data for JSC-1A particle-pyrex pipe system	155
C-1	Inputs and outputs for the simulation.....	158

LIST OF FIGURES

<u>Figure</u>	<u>page</u>
2-1 Schematic of experimental units.....	38
2-2 Experimental setup for measuring particle charge.....	39
2-3 Specific charge of particles leaving the particle charger.....	40
2-4 $q_m(L=1)$ vs. $q_{m,0}$ for borosilicate particles in 1m natural glass pipe.....	41
2-5 $q_m(L=1)$ vs. $q_{m,0}$ for borosilicate particles in 1m copper pipe.....	42
2-6 Predicting particle charge using stair-step method.....	43
2-7 Predicting charging profile for borosilicate particles.....	44
2-8 Comparison of the experimental data with predicted charging profile	45
3-1 Comparison of single phase prediction to benchmark data.	65
3-2 Collision number for soda lime particle in copper pipe	66
3-3 Collision number along the pipe for soda lime particle in copper pipe	66
3-4 Predicted charging profile for soda lime particles in copper pipe.....	67
3-5 Predicted charging profile for JSC-1A particles in natural glass pipe	68
4-1 Schematic of electrospray	90
4-2 Schematic of the bifurcating airway model	91
4-3 Properties of spherical particles.....	92
4-4 PLGA particles generated in various solvents	93
4-5 Microscopic images of rod-shaped particles.....	94
4-6 Microscopic images of hollow, balloon-shaped particles	95
4-7 Experimental setup.....	96
4-8 Experimental setup using a parallel plate capacitor.....	97
4-9 Voltage build-up rates in the Faraday cup at different plate voltages	98
4-10 Emission spectra from solid PLGA film embedded with NIR dye.....	99

4-11	Compilation of IVIS Lumina images showing no photons in the airway model .	100
4-12	Example of individual regions of interest for generation 1 airway	100
4-13	IVIS Lumina images of “neutral” sphere	101
4-14	Evolution of deposition patterns for “neutral” sphere	102
4-15	IVIS Lumina images of positively-charged sphere.....	103
4-16	Evolution of deposition patterns for positively-charged sphere.....	104
4-17	Deposition of rod-shaped particles.	105
5-1	Shape and characteristic dimensions of different types of particles	126
5-2	Schematic of the bifurcating airway model	127
5-3	Schematic of the inverse cyclone seeder setup.....	128
5-4	Particle viewed under optical microscope.....	129
5-5	IVIS Lumina images of glass spheres	131
5-6	IVIS Lumina images of glass flakes 1	132
5-7	Plot of the η^* against Stokes number	133
5-8	Deposition efficiency of the secondary mechanism	134
5-9	η_{pre}^* vs. η_{Exp}^*	136
A-1	Different cases of contact charge transfer in applied electric field.....	145
C-1	The effect of mass loading	159
C-2	The effect of pipe radius	160
C-3	The effect of mean gas velocity	161
C-4	The effect of maximum solid volume fraction.....	162
C-5	The effect of particle diameter	163
C-6	The effect of particle density.....	164
C-7	The effect of particle sphericity	165
C-8	The effect of particle-particle coefficient of restitution.....	166

C-9	The effect of particle-wall coefficient of restitution	167
C-10	The effect of wall specularly coefficient	168
D-1	Comparison for borosilicate particles and copper pipe	169
D-2	Comparison for borosilicate particles and stainless steel pipe.....	170
D-3	Comparison for borosilicate particles and natural glass pipe.....	171
D-4	Comparison for borosilicate particles and Pyrex pipe.....	172
D-5	Comparison for soda lime particles and stainless steel pipe	173
D-6	Comparison for soda lime particles and natural glass pipe	174
D-7	Comparison for soda lime particles and Pyrex pipe.....	175
D-8	Comparison for PMMA particles and copper pipe	176
D-9	Comparison for PMMA particles and stainless steel pipe	177
D-10	Comparison for PMMA particles and natural glass pipe	178
D-11	Comparison for PMMA particles and Pyrex pipe	179
D-12	Comparison for crushed soda lime particles and copper pipe	180
D-13	Comparison for crushed soda lime particles and stainless steel pipe.....	181
D-14	Comparison for crushed soda lime particles and natural glass pipe.....	182
D-15	Comparison for crushed soda lime particles and Pyrex pipe	183
D-16	Comparison for JSC-1A particles and copper pipe.....	184
D-17	Comparison for JSC-1A particles and stainless steel pipe	185
D-18	Comparison for JSC-1A particles and Pyrex pipe.....	186
E-1	IVIS Lumina images of hollow glass particles.....	187
E-2	IVIS Lumina images of glass rod particles.....	188
E-3	IVIS Lumina images of glass flake 1 particles	189
E-4	IVIS Lumina images of glass flake 2 particles	190
E-5	IVIS Lumina images of crushed glass particles	191

E-6	IVIS Lumina images of silver flake particles	192
E-7	IVIS Lumina images of Aluminum Oxide particles	193
E-8	IVIS Lumina images of JSC-1A particles	194

Abstract of Dissertation Presented to the Graduate School
of the University of Florida in Partial Fulfillment of the
Requirements for the Degree of Doctor of Philosophy

THE EFFECTS OF ELECTROSTATIC CHARGE ON PARTICLE FLOWS AND
DEPOSITION

By

Pongpumin Poom Bunchatheeravate

December 2012

Chair: Jennifer S. Curtis
Major: Chemical Engineering

Particulate matters have a wide range of applications in industry. Particle processes range from mixing to transportation. Electrostatic charge and particle morphologies are two parameters that remain relatively unknown, yet they are very important in all processes. The understanding of these two parameters can improve the efficiency of particle processes and their applications. Particle charging occurs during transport; charged particles deposit more readily than neutral particles. The non-spherical shape of the particles can cause differences in flow and charging characteristics. This investigation seeks to expand the knowledge in charging and deposition of spherical and non-spherical particles through two different applications: pneumatic conveying and pulmonary deposition.

Transporting particles in a pipe from one location to another is a simple yet essential process; this process is called pneumatic conveying. Dilute pneumatic conveying is a specific case when the particle concentration in the flow is very low. During transport, particles gain electrostatic charge upon contact with the pipe wall. A method coupling small scale experimentation and computer simulation was devised to

predict a particle's charge in pneumatic conveying systems. Using this predictive method it was possible to accurately predict particle charging for both spherical and non spherical particles in any given pipe length, under different air flow rates and particle mass flow rates.

The particle charge and morphology can lead to different depositions as seen by uncharged spherical particles. These two parameters can lead to an improvement in the field of pulmonary deposition. A technique using near-infrared fluorescence was devised to visualize and quantify particle deposition in a complex airway. Particles of various shapes and charges were sent into a bifurcating airway model. Deposition of the charged particles depended upon the charge distribution of all the particles. When uncharged particles were used, the deposition indicated that low momentum particle deposition was a combination between inertial impaction and diffusion; whereas high momentum particles deposited through inertial impaction and sedimentation.

CHAPTER 1 INTRODUCTION

Particulate matters are essential in many processes in industry. Examples of these processes include transporting particles in a production line, using catalytic particles in fluidized beds to increase the production yield, filtration of dust to minimize contamination, and aerosolizing medicinal particles for use in inhalation therapy. The knowledge of each individual process is well developed. However, there is a characteristic of particulate matter that still remains relatively unknown in all processes. The effect of electrostatic charges on particles in many of these processes still remains elusive.

In particle suspension, particles gain electrostatic charge when they come into contact with other surfaces. The most appropriate process to study particle charging is during particle transport in pipe flow. The study of how charges are generated in a pipeline system can lead to the understanding of particle charging during contact. Once particles become charged, the electrostatic force draws particles toward the wall where they deposit. The best scenario to understand the effect on the enhancement of deposition is in a series of branching airways. With these goals in mind, two sets of experiments were devised in order to:

- Measure particle charging in diluted pneumatic conveying systems
- Accurately predict particle charging in diluted pneumatic conveying systems
- Gauge the use of near infrared fluorescence to quantify particle deposition
- Determine the effect of particle charging on particle deposition
- Determine the effect of particle morphology on particle deposition

These experiments were performed using both spherical and non-spherical particles to determine the influence of particle shape.

The work presented in the following chapters seeks to investigate the particle charging and the deposition of charged particles in the pipeline. Initially, we have particles flowing through a pipeline. As particles flow in the pipeline, they can gain or lose electrostatic charges. The changes in electrostatic charge on the particles are investigated in Chapter 2 and Chapter 3. Electrostatic charges on the particles cause the particles to be more readily deposited on the surface of the pipe. A bifurcating airway model is used to understand the particle deposition in different geometries in a pipeline. Each bifurcating airway contains a section of straight pipe (representing a straight pipeline) and a branching section, where the pipe bifurcates into two airways (representing a split or bend in the pipeline). In addition, bifurcating airways have direct application in pulmonary drug delivery; the airways contain a structure similar to the human lung. The work in the next chapter includes developing a technique to visualize particle deposition in each region of the airway (Chapter 4). To understand particle deposition in the bifurcating airways, two different sets of experiments were performed. The first set of experiments investigated the effect of electrostatic charge on particle deposition (Chapter 4); the second set of experiments investigated the effect of particle morphology on particle deposition (Chapter 5). The work in Chapter 4 and Chapter 5 is used to isolate the effects of particle charge and particle shape.

Particle Charging During Transport

Particle transport (pneumatic conveying) is an essential component in many operations. Pneumatic conveying transports bulk particulate materials from one point to another with minimum cost. When the solid volume is very low compared to the gas volume (less than 1%), particles are suspended in the air during transport; this operating regime is known as dilute phase transport (Rhodes 2008). Airflow is sent into

the pipe at a high velocity to move the particle suspension. Understanding particle charging in pneumatic conveying can lead to a multitude of applications in many industries.

During particle transport, particles acquire electrostatic charge upon contact with the pipe wall. Neglecting electrostatic charge buildup on the particles will result in many serious issues. Some examples include: dust explosions or explosion hazards that are caused by spark discharges from excessively charged particles (Cartwright et al. 1985; Eckhoff 2011; Glor 1985). Charged particles can also accumulate in pipelines causing blockages and flow interferences (Forward et al. 2009). In pharmaceutical applications, charged particles can agglomerate and segregate, leading to uneven drug formulation and dosages (Peart et al. 2003; Supuk et al. 2011). Charged particles generated in medical inhalers can lead to drastically different deposition patterns in the lungs (Leong et al. 2009). On the other hand, there are benefits to having charged particles during transport. Particle charge is key to an online, non-intrusive monitoring system for flow information, including but not limited to mass loading, particle distribution and solid velocity (Matsusaka and Masuda 2006; Matsusaka et al. 2008a; Deng et al. 2011; Gajewski 1996; 2006). Regardless of application, there is a need to measure and control particle charge in pneumatic conveying systems. We presented here, in Chapter 2 and 3, a predictive method coupling a small scale experiment with computer simulation to predict charge on both spherical and non-spherical particles. Experiments were first performed to determine the charging properties and the charge of the particles was then predicted using CFD simulation.

Particle Deposition to Pulmonary Airways

Charged particles tend to deposit on surfaces. A straight pipe is less than ideal for understanding particle deposition. However, branching airways provide a perfect geometry to study particle deposition. Unlike a straight pipe airway, branching airways have multiple sections that use different deposition mechanisms. A direct application for deposition in a series of branching airways is pulmonary drug delivery. The human lungs contain multiple branching airways. Particle deposition in pulmonary airways has great importance in pulmonary medication. The lungs provide a large area for drug delivery. Particles deposited in the lungs can degrade and release drugs into the problematic area; if particles penetrate deep enough and deposit in the alveoli, the drugs can enter into the bloodstream. Understanding how charged particles and non-spherical particles deposit in the branching airways can greatly enhance pulmonary medication.

For this experiment we first investigate techniques using near-infrared (NIR) fluorescence to visualize and quantify particle deposition. Using the NIR fluorescence, we investigated the effect of charged particles (spherical and non-spherical), as well as uncharged (spherical and non-spherical) particles, in a series of bifurcating airways.

CHAPTER 2 PREDICTION OF PARTICLE CHARGING IN A DILUTE PNEUMATIC CONVEYING SYSTEM

Background

Particle charging is a common phenomenon that occurs naturally and frequently. Any process that uses dry powders will involve charged particles. Dilute-phase pneumatic conveying, in which particles are suspended in gas and transported in a pipeline, is such a process found in many particle processing and manufacturing industries. As particles are being transported, they acquire electrostatic charge upon contact with the pipe wall. Neglecting charges in design of particle handling processes may result in many serious issues. Examples include dust explosions or explosion hazards that are caused by spark discharge from overly charged particles (Cartwright et al. 1985; Eckhoff 2011; Glor 1985). Charged particles can also accumulate in pipelines causing blockage and flow interference (Forward et al. 2009). In pharmaceutical applications, charged particles can agglomerate and segregate, leading to changes in drug formulation and dosages (Peart et al. 2003; Supuk et al. 2011). Charged particles generated in medical inhalers can lead to drastically different deposition patterns in the lung (Leong et al. 2009). On the other hand, particle charging can be beneficial; it is possible to use the measured particle charge to create an online, non-intrusive monitoring system for flow information, including but not limited to mass loading, particle distribution and solid velocity (Matsusaka and Masuda 2006; Matsusaka et al. 2008a; Deng et al. 2011; Gajewski 1996; 2006).

Different methods have been used to study the effects of electrostatic charge, using both computer simulations and experimentation. Lim et al. (2012) used large eddy simulation and the discrete element method (DEM) to investigate the effects of

electrostatic charge on flowing granular materials. They found that charged particles exhibit a ring-like distribution during pipe flow with more particles found closer toward the pipe wall. They also investigated the effect on the drag force and the electric field generated due to the electrostatic force. Watano et al. (2003) performed DEM simulations as well as experiments to investigate electrostatic charging when a pile of PMMA particles was blown through a horizontal pipe. They found that the number of wall collisions and the vertical component of the impact velocity are important parameters for charging.

However, most of the research on particle charging has been experimental, focused on determining the overall dependency of electrostatic charging on specific parameters. Masuda et al. (1972) coated a section of a pipeline with a polymer film and used a galvanometer to measure the current transfer upon impact. The number of particle contacts with the wall was then related to the charge transfer. They found that the current transfer between particles and the pipe surface depends on the contact frequency, contact area, contact time, and particle size. Smeltzer et al. (1982) measured the charge buildup on glass beads flowing through plexi-glass pipes. Nickel wires were inserted into the plexi-glass pipe, and the charge was measured when particles came into contact with the wire. They found that the charge was linearly related to the collision frequency, which was measured in the various pipe sections. They also determined that impact charging was the primary mechanism for charge transfer in dilute pneumatic conveying. Yao et al. (2006) used electrical capacitance tomography, together with particle imaging velocimetry, to measure the time required for a flowing particle system to reach electrostatic equilibrium in a cyclic pipe flow. They

found that a longer time is required for a more complex geometry, and electrostatic equilibrium is reached faster in a horizontal pipe than a vertical pipe.

Rather than measuring the charge transfer between particles and pipe surfaces, it is also possible to directly measure the charge on particles using a Faraday cup, also known as a Faraday cage. In this method, when particles enter the Faraday cup, an electric current is sent to the electrometer. The current reading measured from the electrometer can then be directly related to the amount of charge possessed by the particles. Kanazawa et al. (1995) used an electrostatic voltmeter to measure the charge on the pipe surface and a Faraday cup to measure the particle charge in a flowing particle system. They found a bipolar distribution of charge for the irregularly shaped particles, but a single polar distribution of charge for spherical particles. Nieh and Nguyen (1988) also used a Faraday cup to determine the effect of humidity, particle velocity, and particle diameter on particle charging behavior. They found that humidity has a significant effect on particle charging, and particles are neutralized at high humidity. Smaller particles were also found to have a higher charge to mass ratio.

Only a handful of previous studies have investigated the charging behavior for a single particle impact (impact charging) and how the charging can be controlled. Matsusaka et al. (2000) performed experiments using a 31 mm rubber sphere impacting on a steel plate and came to the conclusion that the charge transferred in a single impact depends on the initial charge of the material, the impact velocity and the contact area. Matsuyama and Yamamoto (1995) performed experiments with 3 mm polymer particles and a metal plate; they found that the impact charge is linearly dependent on the initial charge of the particle. There is also a charge beyond which a particle will no

longer gain or lose charge upon further impact; this is known as the equilibrium charge and is independent of the impact conditions. Watanabe et al.(2007) studied 500-600 μm drug particles impacting a stainless steel plate; they found that the equilibrium charge is related to the contact potential difference. Matsusaka et al. (2002) also observed this equilibrium charging in a flowing particle system after a certain pipe length. Matsusaka et al. (2007) then confirmed in a flowing particle system that the amount of charge transfer is a function of the initial charge and the equilibrium charge. They observed that the amount of charge on the particles varies exponentially as a function of pipe length, and the charge transfer continues until particles reach equilibrium charge in the system. With this charging relationship, they were able to control the particle charge in pipe flow by changing the wall material with which the particles come in contact.

In an attempt to control particle charge, Matsusaka et al. (2008b; 2011) have designed and built particle chargers. As particles flow through a conical or cylindrical chamber, the centrifugal force directs the particles toward the wall where they impact and become charged. The particle chargers work on the principle of contact electrification; a particle can gain or lose charge depending on the state of the material with which it comes in contact. The important parameters for the particle charger are the electrostatic properties between the particles and the wall surface and the applied electric field (see Appendix A for the effect of the electric field on the charge transfer).

Theory

Charge Transfer Model for Metal-Metal Systems

In metal-metal contact electrification, electrons are transferred between the surfaces. As a result, one material becomes positively charged while the other becomes

negatively charged. The charge transfer Δq_M between the two metals after one contact, without the influence of external electric field, is given by:

$$\Delta q_M = C_0 V_c \quad (2-1)$$

where C_0 is the contact capacitance between the two metals and V_c is the contact potential difference that is directly dependent on the work function of the two metals.

The work function is related to the amount of energy that is required to strip electrons from the surface; this value is strongly influenced by the surface state (e.g., the amount of valance electrons on the surface). The contact potential difference between the two metals V_c is given by

$$V_c = -\frac{(\varphi_a - \varphi_b)}{e} \quad (2-2)$$

where φ is the work function for each metal, and e is the elementary charge of an electron. Electrons move from the metal with the lower work function to the metal with the higher work function.

Contact electrification for two metals is fairly straightforward; however, when an insulator is involved, the theory becomes more complex. Although controversy exists on the mechanism of the charge transfer for non-metal contact (e.g. electron transfer, ion transfer, or chemical reaction at the contact site), the concepts in Equation 2-2 can still be applied for an insulator-metal or insulator-insulator systems. The work function of an insulator cannot be directly measured. The surface state (e.g. roughness and geometry), the environment (e.g. air or vacuum), and other physical conditions directly influence the work function of an insulator. For an insulator, an 'effective work function', measured at a specific condition, is used in place of the metal work function (Castle 1997).

Charge Transfer Model for Metal-Insulator and Insulator-Insulator Systems

The typical charge transfer model that is applied for any two materials in contact is known as the condenser model (CM). The condenser model describes the contact between the two materials in terms of a capacitor. The contact surfaces are considered to be the two plates in the capacitor, and the charge is transferred due to the potential difference of the two plates or materials. The total potential difference associated with the condenser model (V_{CM}) when particles are in contact can be expressed as:

$$V_{CM}=V_c-V_e-V_b+V_{ex} \quad (2-3)$$

where V_C is calculated from Equation 2-1 and based on the effective work functions, V_e and V_b are the potential differences due to the image charge and the space charge, respectively, and V_{ex} is the potential difference caused by external factors, e.g. an imposed electric field (Matsusaka 2011; Matsusaka et al. 2010). Image charge occurs when the electric field from a point charge induces a charge on its surrounding. Space charge occurs when multiple point charges act together to form a cloud of charge. The terms V_e and V_b are both negative as both inhibit the charge transfer. The charge transfer in the condenser model can then be depicted as:

$$\Delta q_{CM}=k_c CV_{CM} \quad (2-4)$$

where k_c is the charging efficiency and C is the capacitance between the two materials. In the case of metal-metal contact, k_c is equal to one, C is equal to C_0 , and $V_e=V_b=0$. In addition, if $V_{ex}=0$, then Equation 2-4 reduces to Equation 2-1 which describes the charge transfer for metal-metal contacts in the absence of an external electric field.

Charge Transfer Model for Repeated Impacts

To obtain the charge of a particle q as a function of the number of contacts n with a wall, a continuous quantity $\frac{dq_{CM}}{dn}$ is used:

$$\frac{dq_{CM}}{dn} = k_c C V_{CM}(q) \quad (2-5)$$

Equation 2-5 is the continuous form of the single contact ($n=1$) equation depicted in Equation 2-4. During contact, V_e and V_b are proportional to q ; they are generally defined as:

$$V_e = k_e q \quad (2-6)$$

$$V_b = k_b q \quad (2-7)$$

where k_e and k_b are constants associated with the effect of the image charge and space charge respectively. The terms V_C and V_{ex} are not a function of q , and are treated as constants.

In addition to these contributions to charge transfer, Itakura et al. (1996) found that electrostatic leakage from the particle electric field to its surroundings, after the particles are no longer in contact, plays a significant role in the final charge of the particle. The charge leakage is caused by the redistribution of charge on the particle surface. This effect is directly proportional to q . This term is given as

$$\frac{dq_r}{dn} = -k_r q \quad (2-8)$$

where k_r is a constant associated with the effect of charge leakage. The total charge transfer $\frac{dq}{dn}$ can then be represented by

$$\frac{dq}{dn} = \frac{dq_{CM}}{dn} + \frac{dq_r}{dn} = -a q + b \quad (2-9)$$

where constant a includes the effects of the image charge, space charge, and charge relaxation, and b includes the effects of the work functions and the external electric fields. Equation 2-9 can be solved as a first-order, non-homogeneous differential equation with the initial conditions $n=0$ and $q=q_0$, resulting in

$$q = q_0 \exp(-an) + \frac{b}{a} \{1 - \exp(-an)\} \quad (2-10)$$

Equation 2-10 can be further generalized into the following form:

$$q = q_0 \exp\left(-\frac{n}{n_0}\right) + q_\infty \left\{1 - \exp\left(-\frac{n}{n_0}\right)\right\} \quad (2-11)$$

where q_0 is the initial charge of the particle, q_∞ is the equilibrium charge of the particle when n tends to infinity, and n_0 is a constant specific to the particle-wall system. When applying this model to particle flow in a pipe, it can be assumed that the frequency of the particle-wall impacts per unit pipe length is constant, and that the number of impacts n is proportional to the pipe length L . Therefore, Equation 2-11 can be rewritten as

$$q(L) = q_0 \exp\left(-\frac{L}{L_0}\right) + q_\infty \left\{1 - \exp\left(-\frac{L}{L_0}\right)\right\} \quad (2-12)$$

L_0 in Equation 2-12 is analogous to n_0 ; this term is known as the characteristic length.

Finally, dividing Equation 2-12 through by the particle mass and replacing q in Equation 2-12 by the charge-to-mass ratio q_m , i.e. the specific charge, yields the following equation which describes the particle charge as a function of pipe length:

$$q_m(L) = q_{m,0} \exp\left(-\frac{L}{L_0}\right) + q_{m,\infty} \left\{1 - \exp\left(-\frac{L}{L_0}\right)\right\} \quad (2-13)$$

Experiments

Experimental Setup

The experimental system is composed of four sections including a feeder, a particle charger, a pipe, and a Faraday cup electrometer as shown in Figure 2-1. Figure

2-1A gives a detailed diagram of the feeder section, which consists of a vibratory feeder and a particle ejector. The vibratory feeder was made by placing a long stem funnel on top of a stainless steel plate, and piezo-electric vibrators were connected to the funnel and plate. The particle mass flow rate was controlled by the electric signal sent from a feeder controller (VST-01 Control system, IMP Co. Ltd.). Particle mass flow rate in all experiments is approximately 0.05 mg/s. Particles leaving the feeder were drawn, by vacuum, into a particle ejector. The particle ejector consists of two sections - upstream where the particles enter and downstream where the particles mix with the air and exit. A nozzle opening was used to separate the two sections and functioned to direct the compressed air toward the exit; in doing so, the compressed air created suction in the upstream section. The air flow rate was controlled using a pressure controller; during the experiment, the flow rate was kept at 15 m/s. To prevent electrostatic disturbance, all components in the feeder section were grounded.

After leaving the ejector, particles were sent to the particle charger in order to control the particle charge. The particle charger used was the same one developed in Matsusaka's group (2008a; 2008b; Matsusaka 2011). A diagram of the particle charger with a conical chamber is shown in Figure 2-1B. Particles enter from the top and exit from the bottom of the charger; the broken line illustrates the particle flow path in the particle charger. The conical shape allows for maximum particle-wall contact as the particles flow through the charger. Within the particle charger, there is a cone shaped electrode at the center. The inner wall of the charger, i.e. inner electrode, was designed in such a way that the cavity was 0.01 m wide. The outer wall of the charger, i.e. the outer electrode, was grounded during operation. Both electrodes were made using

stainless steel. A high voltage source (Matsusada Precision Inc.) was connected to the inner electrode to generate an electric field between the inner and outer walls of the cavity. As particles come into contact with the outer electrode, the particles can gain or lose electrons as explained in Appendix A. The final charge of the particles leaving the charger directly depends upon the charge supplied to the inner electrode.

Upon exiting the particle charger (or pipe), the particle charge was measured using a Faraday cup electrometer. As shown in Figure 2-1C, the Faraday cup was connected to a vacuum system in order to collect particles into a thimble filter. The charge reading from the inner conductive surface was sent to the electrometer (Takeda Riken Co. Ltd.). The mass of the particles collected was determined using an analytical balance (least count of 0.001g). The specific charge was obtained from the total charge and mass information.

Short Pipe Experimentation with Varying Initial Charge

The schematics of the setups for these sets of experiments are shown in Figures 2-2A and 2-2B. The arrows on the left in Figure 2-2 represent particles exiting the particle ejector shown in Figure 2-1A. In Figures 2-2A and 2-2B, a 0.3m polyurethane tube connects the particle ejector to the particle charger. A 0.07 m glass tube was also used to direct the charged particles out of the particle charger. The Faraday cup was placed at the exit of the 0.07 m glass tube to measure $q_{m,0}$, as seen in Figure 2-2A. The Faraday cup was also placed after the 1m pipe to measure $q_m(L=1)$, seen in Figure 2-2B. Exit charge data ($q_m(L=1)$) for the particles were collected for each particle-pipe material combination by varying the initial charge applied to the particles using the particle charger.

Validation Experiments with Longer Pipes

In order to validate the proposed technique, the exit charge data for the particles were collected at different lengths of pipe. The experimental setups are shown in Figure 2-2C and 2-2D. In these setups, a 0.1 m brass pipe is placed after the particle ejector. The Faraday cup was positioned as seen in Figure 2-2C to measure $q_{m,0}$ for these validation experiments. The setup in Figure 2-2D was employed to collect particle charging data after 1-, 2-, 3-, and 4-m pipe length. The air flow rate in the pipes was measured after the ejector and after 1-, 2-, 3-, and 4-m pipe to ensure that there were no changes in the flow rate with each additional pipe length.

Particles and Pipes

A total of five different types of particles and four different types of pipe wall materials were tested. A summary of particles and pipes with their specifications are found in Table 2-1 and 2-2 respectively. Due to the extensive amount of data, only the results of borosilicate particles flowing in a natural glass pipe and in a copper pipe will be discussed as a representative example. The rest of the data are included in appendix B.

Results and Discussion

Varying Initial Charge in the Particle Charger

The initial charge of the particles entering the 1 m pipe was adjusted using the particle charger (Figure 2-2A). The initial charge was measured at different voltages applied to the inner electrode of the charger. Figure 2-3 shows the specific charge of the borosilicate particles as a function of electric field strength in the particle charger. The polarity of the particle charge could be changed from negative to positive. However, there is a limit to the particle charging with higher applied electric field because of

electrical discharge in the particle charger. Applying voltage higher than this limit causes a decrease in particle charge; this is demonstrated by the maximum in the curve shown in Figure 2-3.

Short Pipe Experimentation with Varying Initial Charge

Particle charge measurements were made using the setup in Figures 2-2A and 2-2B. The initial charge of the particles is denoted $q_{m,0}$, and the particle charge collected after flowing in the 1m pipe is denoted $q_m(L=1)$. The particle charge measurements were repeated three times. A relationship between $q_{m,0}$ and $q_m(L=1)$ for borosilicate particles in the natural glass pipe is shown in Figure 2-4. The $q_m(L=1)$ versus $q_{m,0}$ curve exhibits a linear relationship, which agrees with Equation 2-9 in the theory on the repeated impacts model. Matsuyama and Yamamoto (1995) observed similar behavior in their single particle impact experiments. Figure 2-4 also includes a broken line representing $q_{m,0}=q_m(L=1)$. The experimental data for $q_m(L=1)$ versus $q_{m,0}$ are higher than the broken line; this result indicates that the particles obtained a positive charge from the wall by contact electrification. In other words, the electrons on the particles were transferred to the wall.

Figure 2-5 shows the experimental results of $q_m(L=1)$ versus $q_{m,0}$ for borosilicate particles in a copper pipe. The $q_m(L=1)$ versus $q_{m,0}$ curve again exhibits a linear relationship. However, in this case, the experimental line intersects with a line representing $q_{m,0}=q_m(L=1)$ at a $q_{m,0}$ value of $-59 \mu\text{C}/\text{kg}$. This means that the equilibrium charge was within the range in initial particle charges tested, and the value of the equilibrium charge is $-59 \mu\text{C}/\text{kg}$. In other words, irrespective of initial (positive or

negative) charge, if borosilicate particles flow through an infinitely long pipe, the particles will consistently reach this equilibrium charge value.

Predicting Particle Charging using Stair-Stepping Procedure

A technique to predict particle charge in any given length of pipe is proposed in Figure 2-6. The solid curve, i.e. $q_m(L=1)$ versus $q_{m,0}$ line, is the same as that in Figure 2-4, which is the result for the borosilicate particles traveling through the natural glass pipe. First, an initial charge on the $q_{m,0}=q_m(L=1)$ line is found. This point is labeled as P_0 . From this point a vertical line to the $q_m(L=1)$ versus $q_{m,0}$ line is drawn. This vertical line represents the final charge on the particles after traveling through 1m of the natural glass pipe with initial charge P_0 . A horizontal line is then drawn to the $q_{m,0}=q_m(L=1)$ line in order to set a new initial charge P_1 . If this stair-stepping process is repeated, the final charge of the particles at any given pipe length can be determined.

The $q_m(L=1)$ versus $q_{m,0}$ line is not parallel to the $q_{m,0}=q_m(L=1)$ line; therefore, at a certain point the two lines will intersect. This intersection point represents the value of the particle charge when it has reached its equilibrium state, i.e. the particles will no longer gain or lose charge, regardless of continued interactions with the pipe surface.

Predicting Particle Charging using the Semi-Theoretical Equations

The experimental measurements in the short 1 m pipe can be used to determine the two constants $q_{m,\infty}$ and L_0 in the semi-theoretical Equation 2-13, which describes the particle charge as a function of pipe length. Those two parameters $q_{m,\infty}$ and L_0 are easily found using the relationship in Figure 2-4. In Figure 2-4, the specific charge of particles traveling through a pipe can be expressed as the following linear equation:

$$q_m(L=1) = c q_{m,0} + d \quad (2-14)$$

where c and d are constants, The equilibrium charge $q_{m,\infty}$ can be calculated by finding the intersection point between Equation 2-14 and line $q_{m,0}=q_m(L=1)$. Mathematically, this equilibrium charge is given by

$$q_{m,\infty} = \frac{d}{1-c} \quad (2-15)$$

To order to determine L_0 , a comparison of Equation 2-14 to Equation 2-13 results in:

$$c = \exp\left(-\frac{L}{L_0}\right) \quad (2-16)$$

or

$$L_0 = -\frac{L}{\ln c} \quad (2-17)$$

The resulting constants $q_{m,\infty}$ and L_0 for each type of particle in each pipe wall material are summarized in Table 2-3. The values of L_0 are 11.3 m and 3.9 m for the borosilicate-natural glass and the borosilicate-copper systems, respectively. In general, as the value of L_0 increases, the slower the charge transfers between the particles and the wall. Based on the values of L_0 in Table 2-3, the insulator-metal system exhibits higher charge transfer than the insulator-insulator system.

Figure 2-7A shows the predicted charging profiles for borosilicate particles in a natural glass pipe using Equation 2-13 with $q_{m,\infty}$ and L_0 determined from the short pipe experimentation. Figure 2-7B shows the predicted charging profiles for borosilicate particles in a copper pipe. The multiple lines in both figures show the predictions for different initial charges $q_{m,0}$. The particle charge approaches the equilibrium value more quickly (i.e. shorter pipe lengths) for the borosilicate-copper pipe (insulator-metal) system than for the borosilicate-glass (insulator-insulator) pipe system. The charging

profiles are symmetrical with respect to the equilibrium for the same absolute value of

$$q_{m,0} - q_{m,\infty}$$

Technique Validation

To validate the technique for predicting particle charging in any given pipe length, particle charging data were collected using different lengths of pipe as shown Figures 2-2C and 2-2D. Again, the particle charge measurements were repeated three times. These data were compared with the predicted charging profiles as given by equation-13 with values for $q_{m,\infty}$ and L_0 based on the short pipe experimentation. For all the particle-pipe wall material combinations tested, the comparisons between predicted and measured charging profiles are in good agreement. Figure 2-8A compares the predicted charging profile to the experimental data for borosilicate particles flowing in the natural glass pipe. Figure 2-8B shows the comparisons between predicted and measured charging profiles for borosilicate particles in the copper pipe. Two additional representative comparisons are shown in Figures 2-8C and 2-8D. Figure 2-8C presents the comparisons for PMMA spherical particles in a stainless steel pipe, and Figure 2-8D for non-spherical crushed soda lime glass particles in a Pyrex pipe. The small deviations are likely caused by variations in the surface state of pipes.

Summary

A predictive technique for particle charging behavior in pipes of any given length has been developed and tested for a range of particle characteristics and pipe wall materials. This predictive technique is based on experimentation in a short pipe section with varying initial particle charge. The predictive technique is applicable to any metal-metal, metal-insulator and insulator-insulator particle-wall system with two limitations.

First, particle charging must be via the impact charging mechanism. For example, this predictive technique would not be applicable to dense-phase pneumatic conveying where particles are in sustained contact with the wall. Second, the particle and pipe wall materials and the operating conditions (e.g. air and solids flow rate) in which $q_{m,\infty}$ and L_0 are determined from the short pipe experimentation must be the same as the case in which particle charging is being predicted in longer length pipes. Given these two limitations, this predictive technique should work well for a full range of particle characteristics (including initial charge) and pipe wall materials.

Table 2-1. Characteristics of particles used in the experiment

Type of particle	Shape	Mass median diameter (μm)	Mass mean diameter (μm)	Standard deviation (μm)
Borosilicate	Spherical	49	48	3
Soda lime	Spherical	79	78	8
PMMA	Spherical	67	67	16
Crush soda lime	Non-spherical	66	66	16
JSC-1A (30-90 μm) sieve fraction	Non-spherical	55	54	16

Table 2-2. Characteristic of pipes used in the experiment

Material of pipe	Inner diameter (m)
Copper	0.0070
Stainless steel	0.0070
Natural glass	0.0068
Pyrex	0.0068

Table 2-3. Characteristic values for each particle in 1-m pipe

Material of particle	Material of pipe	c (-)	d ($\mu\text{C}/\text{kg}$)	L_0 (m)	$q_{m,\infty}$ ($\mu\text{C}/\text{kg}$)
Borosilicate	Copper	0.77 ± 0.20	-13.4 ± 2.0	3.9 ± 0.3	-59 ± 4
	Stainless steel	0.26 ± 0.29	-83.8 ± 2.9	0.7 ± 0.7	-113 ± 11
	Natural glass	0.91 ± 0.47	60.2 ± 2.4	11.3 ± 0.5	711 ± 19
	Pyrex	0.95 ± 0.40	24.1 ± 3.2	19.1 ± 0.4	473 ± 14
Soda lime	Copper	0.73 ± 0.23	-4.7 ± 2.1	3.1 ± 0.4	-17 ± 3
	Stainless steel	0.24 ± 0.22	-42.3 ± 6.5	0.7 ± 0.6	-56 ± 7
	Natural glass	0.91 ± 0.20	19.5 ± 2.4	10.3 ± 0.3	212 ± 7
	Pyrex	0.92 ± 0.29	14.7 ± 3.9	11.4 ± 0.4	175 ± 8
PMMA	Copper	0.56 ± 0.56	339.8 ± 13.8	1.7 ± 0.7	766 ± 27
	Stainless steel	0.49 ± 0.64	736.8 ± 14.8	1.4 ± 0.7	1451 ± 43
	Natural glass	0.59 ± 0.53	204.8 ± 8.9	1.9 ± 0.6	504 ± 21
	Pyrex	0.70 ± 0.53	111.4 ± 9.2	2.8 ± 0.4	368 ± 13
Crush soda lime	Copper	0.80 ± 0.33	3.1 ± 1.2	4.4 ± 0.4	15 ± 3
	Stainless steel	0.59 ± 0.28	-2.5 ± 0.7	1.9 ± 0.4	-6 ± 2
	Natural glass	0.91 ± 0.35	15.9 ± 1.4	10.7 ± 0.4	179 ± 8
	Pyrex	0.96 ± 0.29	12.5 ± 1.0	22.2 ± 0.4	285 ± 9
JSC-1A (30-90 μm) sieve fraction	Copper	0.76 ± 0.27	-25.4 ± 1.7	3.6 ± 0.4	-105 ± 6
	Stainless steel	0.39 ± 0.33	-27.3 ± 1.0	1.1 ± 0.6	-45 ± 6
	Natural glass	0.88 ± 0.18	30.8 ± 1.9	8.1 ± 0.3	265 ± 7
	Pyrex	0.95 ± 0.32	10.3 ± 0.4	19.9 ± 0.4	211 ± 8

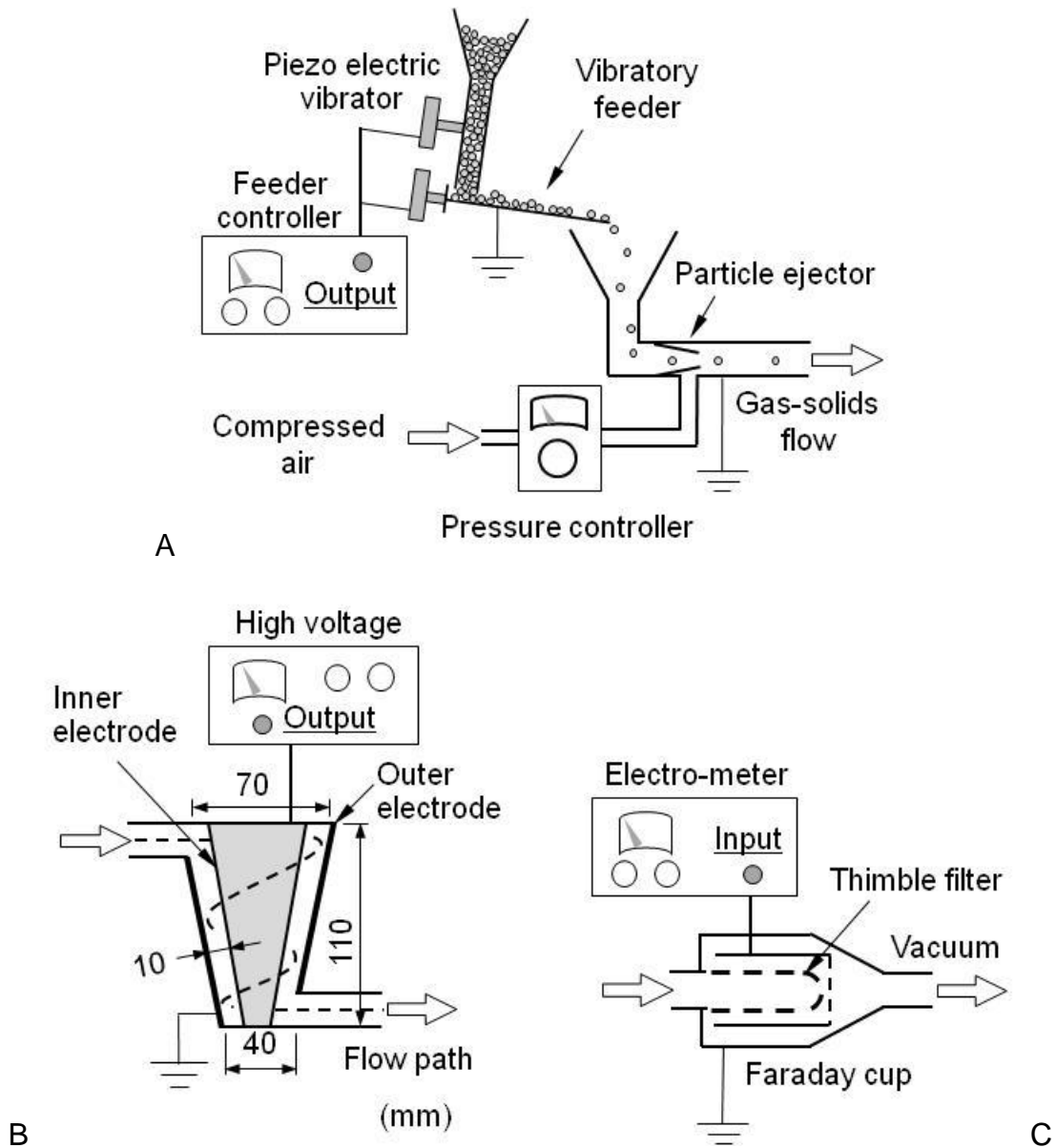


Figure 2-1. Schematic of experimental units. A) Particle feeder. B) Particle charger. C) Faraday cup electrometer. All units are in mm

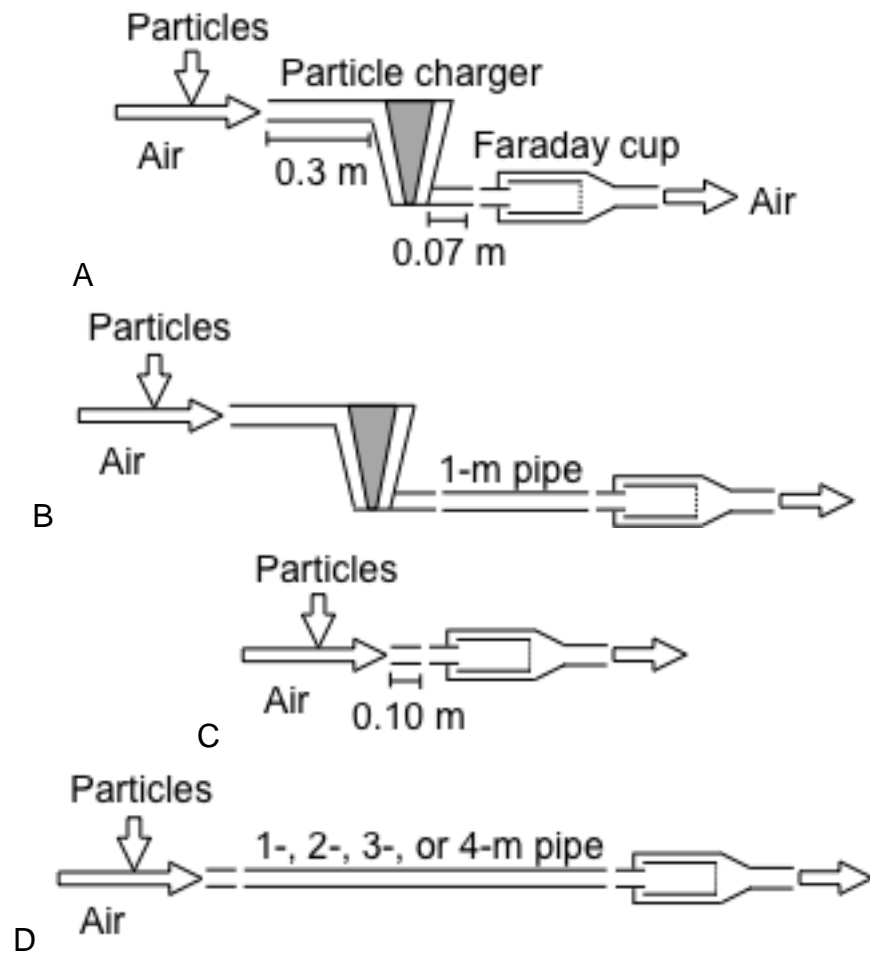


Figure 2-2. Experimental setup for measuring particle charge. A) After leaving the particle charger. B) After 1-m pipe length. C) After the ejector, D) After different pipe length.

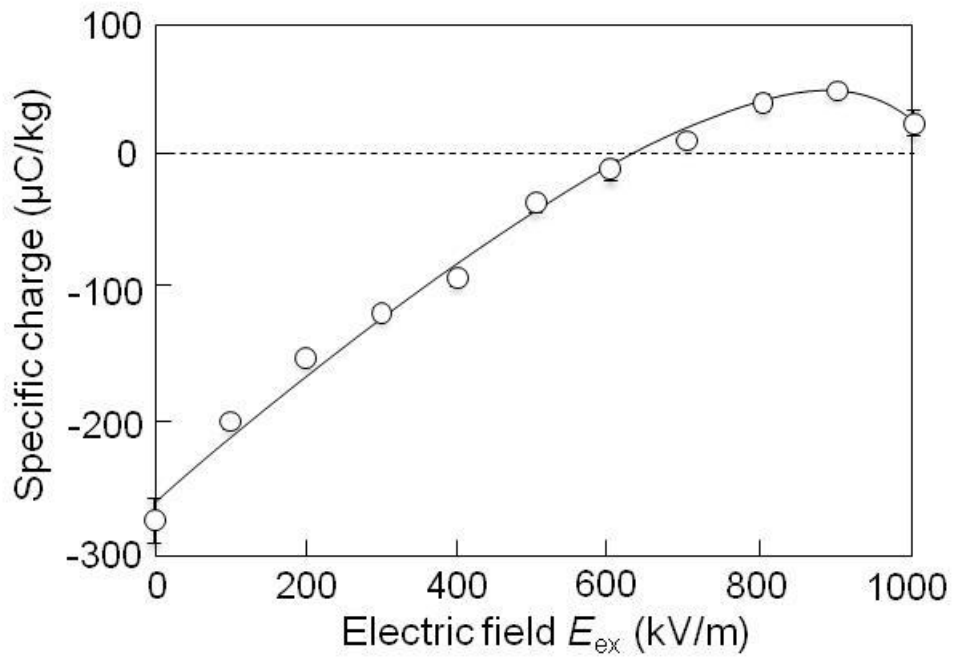


Figure 2-3. Specific charge of borosilicate particles leaving the particle charger as a function of applied electrical field in the particle charger

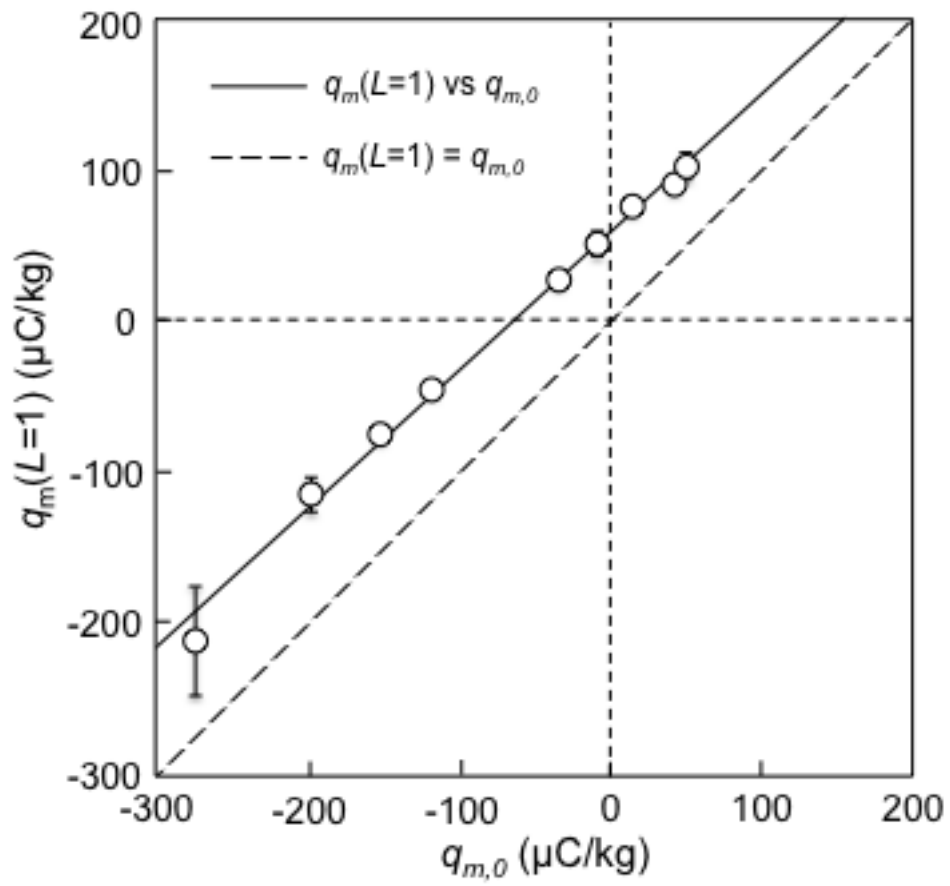


Figure 2-4. $q_m(L=1)$ vs. $q_{m,0}$ for borosilicate particles in 1m natural glass pipe

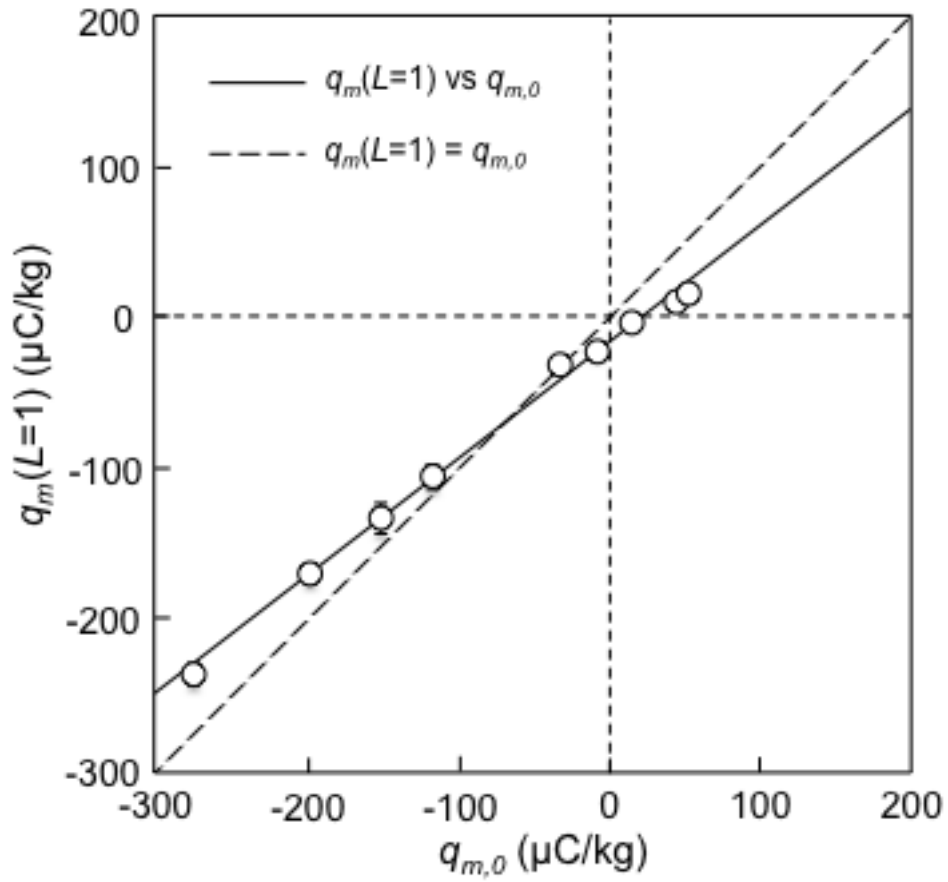


Figure 2-5. $q_m(L=1)$ vs. $q_{m,0}$ for borosilicate particles in 1m copper pipe

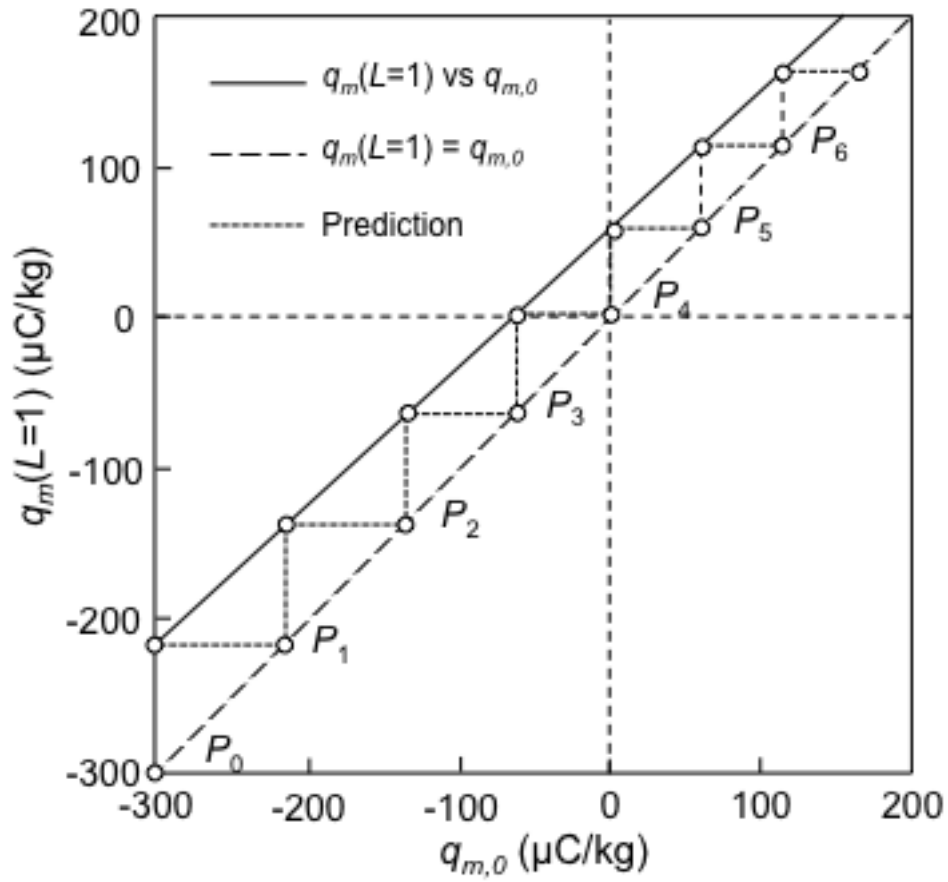
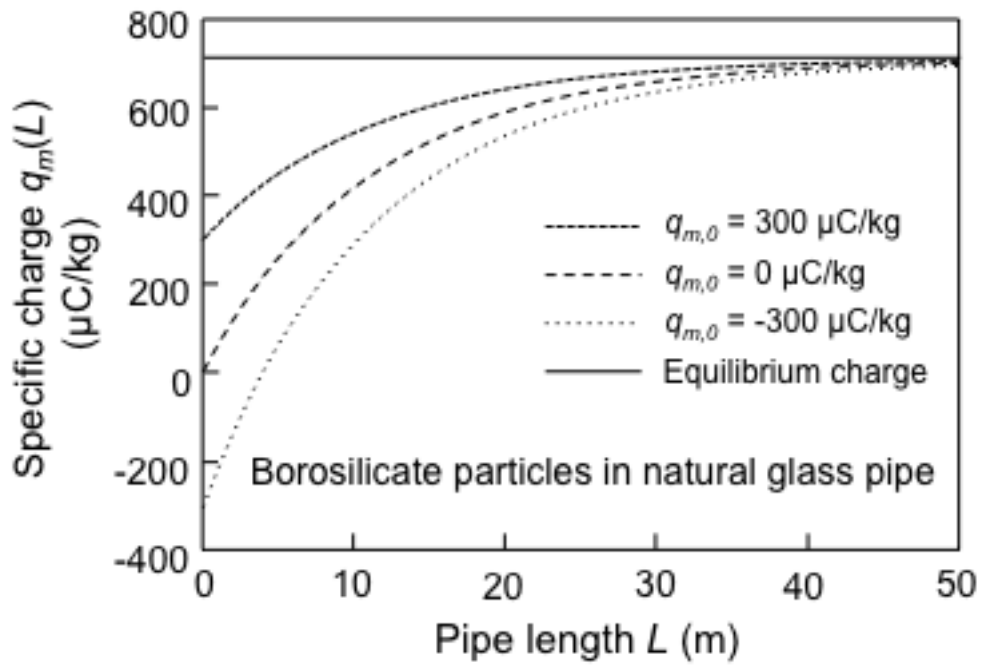
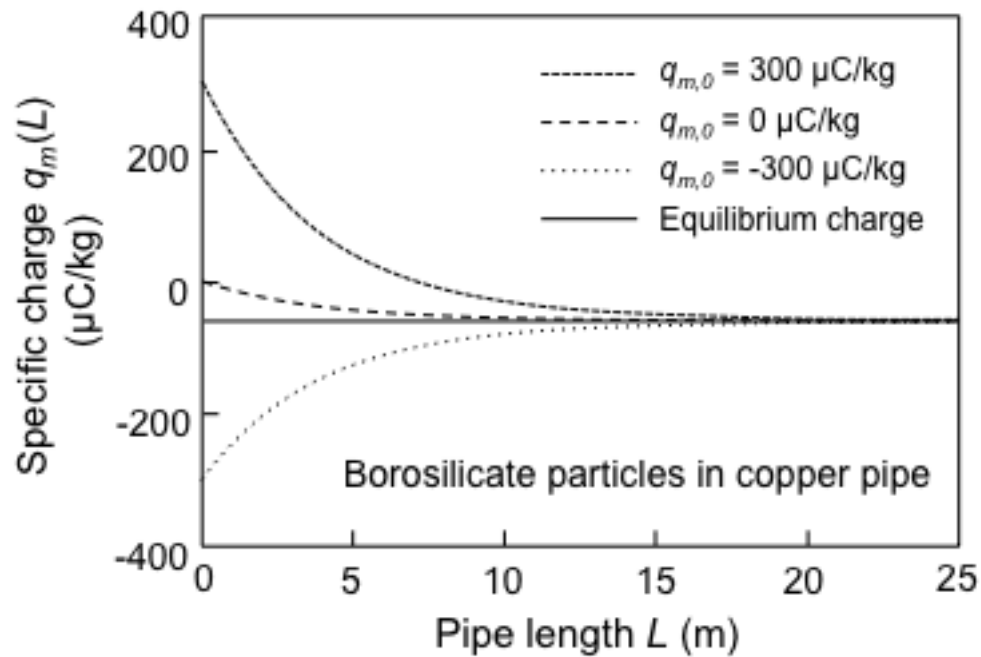


Figure 2-6. Predicting particle charge using stair-step method



A



B

Figure 2-7. Predicting charging profile for borosilicate particles. A) Natural glass pipe. B) Copper pipe

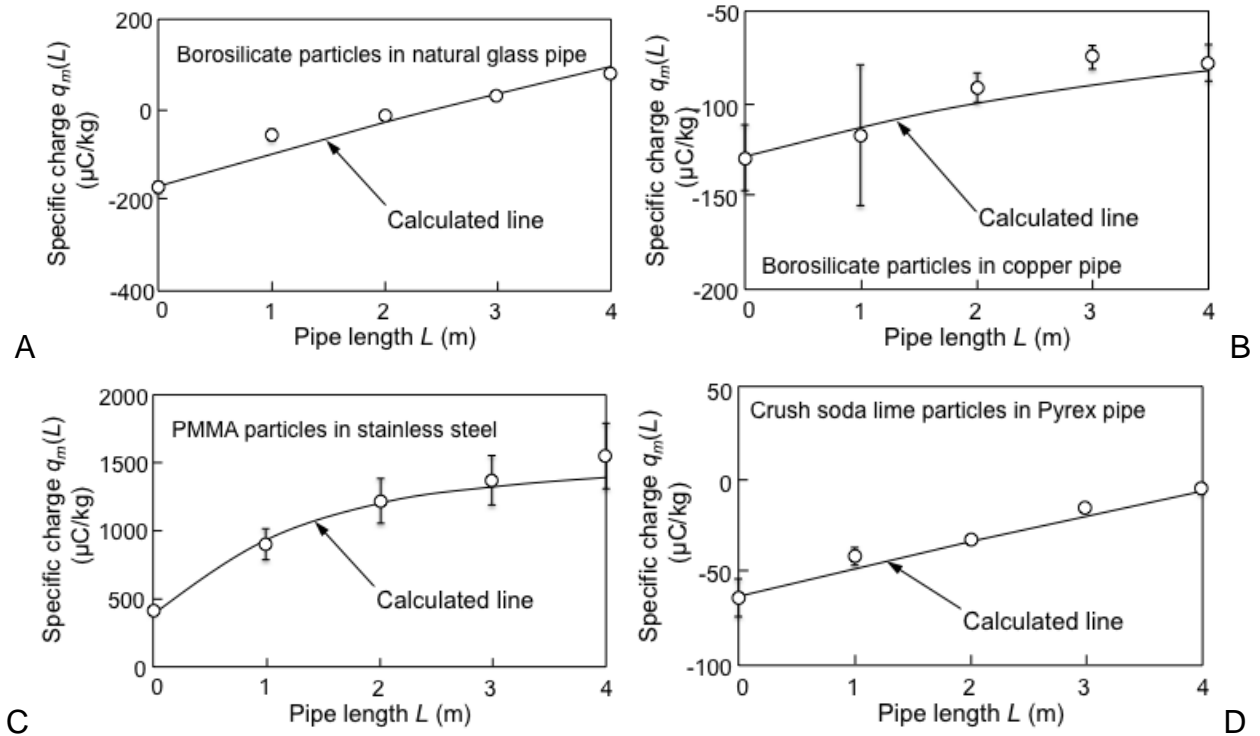


Figure 2-8. Comparison of the experimental data with predicted charging profile. A) Borosilicate particles in natural glass pipe. B) Borosilicate particles in copper pipe. C) PMMA particles in stainless steel pipe. D) Crush soda lime particle in Pyrex pipe.

CHAPTER 3 CHARGE PREDICTION USING COMPUTATIONAL FLUIDS DYNAMICS (CFD) SIMULATION

Background

Using the previously determined parameter (L_0 and q_∞) in Chapter 2, it is possible to determine the charging using computer simulation. Previously only a few attempts were made to create a predictive model for particle charging. Tanoue et al. (2001) used coupled CFD-DEM method to predict 2D particle trajectory. Turbulent gas-phase was model using Navier-stokes equations then solves the particle motion using force balances. The charge transfer at each collision was derived theoretically. They had found that the number of collision in pipe is a function of Stokes number. Cangialosi et al. (2006) used direct simulation Monte Carlo (DSMC) simulations to statistically determine the charge on particle and pipe at any time. In DSMC uses Boltzmann equation and Knudson number to determine the flow for fluid and particles. The DSMC simulation was able to predict particle charge in straight pipe; prediction for curve pipe was also possible with fitting parameter. These two types of simulation provide detail result but require high computational cost.

In this work the continuum CFD model was employed to determine the collision frequency in the pipe. Unlike DEM and DSMC simulation, the continuum model is performed with much lower computational cost, minimizing the computational time. The advantage makes the continuum model an attractive model for use in industry. With the parameters determine in the experiment and the collision frequency determined by CFD simulation, it is now possible to accurately predict the particle charge of the same particle pipe system under any operating condition (e.g. pipe length, pipe diameter, flow velocity, and particle loading).

Model Description

Governing Equations

A Eulerian model is used for modeling the diluted gas-solid particle system in a pipe. The governing equations follow the volume average equations of Anderson and Jackson (1967). The continuity equations are given as:

$$\frac{\partial}{\partial t}(1-v) + \nabla \cdot (1-v)V_g = 0 \quad (3-1)$$

$$\frac{\partial}{\partial t}v + \nabla \cdot vV_s = 0 \quad (3-2)$$

Where t is time, v is the solid volume fraction (Note that $1-v$ is the gas volume fraction), V_g is the mean gas velocity, and V_s is the mean solid velocity. Equation 3-1 is the gas phase continuity equation and Equation 3-2 is the solid phase continuity equation. The momentum equations are:

$$(1-v)\rho_g \left[\frac{\partial}{\partial t}V_g + V_g \cdot \nabla V_g \right] = -(1-v) \nabla P + \nabla \cdot \left((1-v)\tau_g \right) - F_D + (1-v)\rho_g g \quad (3-3)$$

$$v\rho_s \left[\frac{\partial}{\partial t}V_s + V_s \cdot \nabla V_s \right] = -v \nabla P + \nabla \cdot \sigma_s + F_D + v(\rho_s - \rho_g)g \quad (3-4)$$

P is pressure, ρ_g is the gas density, ρ_s is the solid density, and g is the acceleration due to gravity, τ_g is the gas-phase stress, σ_s is the solid-phase stress, and F_D is the drag force. Equation 3-3 is the gas momentum equation and Equation 3-4 is the solid momentum equation. Closure models are required to solve the continuity and momentum equations. The closure models will determine the drag force (F_D), the gas phase stress (τ_g), and solid stress (σ_s).

Drag Models

The drag models represent the momentum transfer between the gas phase and the solid phase. The drag force is define as

$$F_D = \beta(V_g - V_s) \quad (3-5)$$

The drag coefficient (β) are determined semi-theoretically. The drag coefficient follows the model by Haider and Levenspiel (1989). This model uses sphericity (Ψ) to model drag for both spherical and non-spherical particle. Sphericity refers to how spherical a particle is. It is express as the ratio of the surface area of sphere with the same volume as the particle to the surface area of the particle. The Haider and Levenspiel is given as

$$\beta = \frac{3}{4} \frac{C_D}{Re_p} \frac{v}{(1-v)^{2.65}} |V_g - V_s| \quad (3-6)$$

using

$$A_{HL} = \exp(2.3288 - 6.4581\Psi + 2.4486\Psi^2) \quad (3-7)$$

$$B_{HL} = 0.0964 + 0.5565\Psi \quad (3-8)$$

$$C_{HL} = \exp(4.905 - 13.844\Psi + 18.4222\Psi^2 - 10.2599\Psi^3) \quad (3-9)$$

$$D_{HL} = \exp(1.4681 + 12.2584\Psi - 20.7322\Psi^2 + 15.8855\Psi^3) \quad (3-10)$$

$$C_D = \frac{24}{Re_p} (1 + A_{HL} Re_p^{B_{HL}}) + \frac{C_{HL}}{1 + D_{HL}/Re_p} \quad (3-11)$$

Gas Phase Stress

The turbulent model employed is the standard k- ϵ model. The k- ϵ model balances the convective and diffusive energy transport with the generation and dissipation of turbulent kinetic energy. The k- ϵ model for two phase flow is

$$(1-v)\rho_g \left[\frac{\partial k}{\partial t} + V_g \cdot \nabla k \right] = \nabla \cdot \left[(1-v) \frac{\mu_g^t}{\sigma_k} \nabla k \right] + (1-v)T_g : \nabla V_g - (1-v)\rho_g \epsilon + I_k \quad (3-12)$$

$$(1-v)\rho_g \left[\frac{\partial \epsilon}{\partial t} + V_g \cdot \nabla \epsilon \right] = \nabla \cdot \left[(1-v) \frac{\mu_g^t}{\sigma_\epsilon} \nabla \epsilon \right] + (1-v) \frac{\epsilon}{k} \left(c_{T1} f_{T1} T_g : \nabla V_g - \rho_g c_{T2} f_{T2} \epsilon \right) + c_{T3} f_{T2} \frac{\epsilon}{k} I_k \quad (3-13)$$

The two-phase $k-\varepsilon$ model (Equation 3-14 and 3-15) is similar to the single-phase model. An additional term (I_k) is the interaction term cause by the solid phase. The addition of particle can result in enhancement or damping of the turbulent kinetic energy. The gas-phase stress is calculate using

$$\tau_g = (\mu_{eg} + \mu_T) \left[\nabla V_g + \nabla V_g^T - \frac{2}{3} (\nabla \cdot V_g) \underline{I} \right] \quad (3-14)$$

The gas-phase stress is made up of two parts the stress cause by the intrinsic viscosity of the fluid (μ_{eg}) and the stress cause by turbulent (μ_T). μ_{eg} is determine by using equation from Rao et al. (2011).

$$\mu_{eg} = \mu_g (1 + 2.5v + 7.6v^2) \left(1 - \frac{v}{v_0} \right) \quad (3-15)$$

and the turbulent stress contribution is

$$\mu_T = \rho_g c_\mu f_\mu \frac{k^2}{\varepsilon} \quad (3-16)$$

v_0 is the maximum solid volume fraction. The constants are summarized in Table 3-1.

Solid Stress

In the case of diluted pipe flow, the solid stress is separate out into the kinetic solid stress (σ^k) and the collisional solid stress (σ^c). The frictional solid stress is excluded from the model for diluted flow. The equation for solid stress is

$$\sigma_s = \omega \sigma^k + \sigma^c \quad (3-17)$$

The kinetic solid stress contains a damping function (ω) to limit this stress from approaching infinity. Both the kinetic and collisional solid stress are cause by the motion of particles; both stresses are depend on the particle fluctuating velocity (v'_s). The magnitude of particle fluctuating velocity is call granular temperature (T).

$$v'_s = \sqrt{3T} \quad (3-18)$$

The granular temperature balance is

$$\frac{3}{2} \nu \rho_s \left[\frac{\partial T}{\partial t} + V_s \cdot \nabla T \right] = \nabla \cdot (\lambda \nabla T) + \sigma_s \cdot \nabla V_s - \gamma + I_T \quad (3-19)$$

where λ is the granular conductivity, γ is the dissipation due to collision, and I_T is the granular temperature modulation. Additional equations are required to close the granular temperature equation. The equations for the solid stress follow the stress model theoretically derived by Lun et al. (1984). The solid stress equations are as follow:

$$\sigma_{normal} = \rho_s (\omega G_{1k} + G_{1c}) T \quad (3-20)$$

$$\sigma_{shear} = -\mu_s \nabla \cdot V_s \quad (3-21)$$

$$\mu_s = \frac{5\sqrt{\pi}}{96} \rho_s d_p (\omega G_{2k} + G_{2c}) T^{0.5} \quad (3-22)$$

$$\lambda = \frac{25\sqrt{\pi}}{128} \rho_s d_p (\omega G_{3k} + G_{3c}) T^{0.5} \quad (3-23)$$

$$\gamma = \frac{48}{\sqrt{\pi}} \eta (1-\eta) g_0 v^2 \frac{\rho_s}{d_p} T^{1.5} \quad (3-24)$$

The definition of G_{1k} , G_{1c} , G_{2k} , G_{2c} , G_{3k} , G_{3c} , η , and g_0 are listed in Table 3-1.

Turbulence Interaction

Two interaction terms are seen in the model: I_k in the k - ε model equations (Equation 3-12 and 3-13), and I_T in the granular temperature equation (Equation 3-19).

The interaction terms represent the energy transfer in the fluctuating component between the two phases. Louge et al. (1991) simplified the interaction terms into

$$I_k = -\beta(1-\nu) \left(2k - \overline{v_g v_s} \right) = -\beta(1-\nu) (2k - k_{sg}) \quad (3-25)$$

$$I_T = -\beta(1-\nu) \left(\overline{v_g v_s} - 3T \right) = -\beta(1-\nu) (k_{sg} - 3T) \quad (3-26)$$

k_{sg} is known as the cross correlation model. Many authors proposed different expression for k_{sg} . The model used will follow the cross correlation model derived by Sinclair and Mallo (1998) and validated by Rao et al. (2011).

$$k_{sg} = \sqrt{6kT} \quad (3-27)$$

Computer Simulation

Computational simulations of two-phase pipe flow were performed using Equation 3-1 to 3-27. The equations are discretized using the finite volume based method describe in Patankar and Spadling (1967). No-slip boundary conditions are used for the gas phase. The solid phase boundary conditions follow Johnson and Jackson (1987). Boundary condition for k and ϵ follow Bolio et al. (1995). The inputs and outputs for the code are listed in Table 2-2. The mass loading (m) is the mass ratio of particle flow rate to gas flow rate. The specularity coefficient (ϕ) is semi empirical constant arising from momentum loss during wall collision; this term represents the surface roughness of the wall.

Determining Collision Number

The collision frequency can be calculated using the particle fluctuating velocity (v'_s) and the inter-grain spacing (s). The particle fluctuating velocity is determined from the granular temperature (T) using Equation 3- 18. In this case of axisymmetric fully developed flow, the particle fluctuating velocity is the random movement of the particle in the r -direction, (i.e. particle velocity toward or away from the pipe wall). The inter-grain spacing is calculate using

$$s = d \left[\left(\frac{v'_0}{v} \right)^{1/3} - 1 \right] \quad (3-28)$$

The inter-grain spacing is the average distance from particle surface to other surfaces. Beyond this length particle will come into contact with another particle or the wall. The local collision frequency of the solid phase at any radial point in the pipe is

$$n' = \left(\frac{V'_s}{s} \right) \quad (3-29)$$

The unit of n' is collision per time. The charge transfers will occur during particle-wall contacts. The particle wall collision is Equation 3-29 calculated at the wall. The total particle-wall collision number for all the particles flowing through the pipe adjusted for particle mass (n_T^*) is found by multiplying the particle-wall collision by the particle residence time (τ) determined from the superficial velocity ($V_{s,s}$)

$$n_T^* = \tau \cdot n' |_{wall} = \left(\frac{L}{V_{s,s}} \right) \cdot \left(\frac{V'_s}{s} \right) |_{wall} = \left(\frac{L}{V V_s} \right) \cdot \left(\frac{V'_s}{s} \right) |_{wall} \quad (3-30)$$

where V_s is the velocity of the particles. Using n_T^* from Equation 3-30 it is possible to determine particle charging in a system using

$$q_m = q_{m,0} \exp\left(-\frac{n_T^*}{n_{T,0}^*}\right) + q_{m,\infty} \left\{ 1 - \exp\left(-\frac{n_T^*}{n_{T,0}^*}\right) \right\} \quad (3-31)$$

Equation 3-31 is another form of Equation 2-11, this equation determine the specific charge for multiple particle system based on the number of collision. Instead of looking at the particle-wall collision number for a single particle (n), Equation 3-31 uses the total particle-wall collision number for all particles (n_T^*). The term $n_{T,0}^*$ in Equation 3-31 is determined by relating the L_0 term, determined from the experiment in Chapter 2, to the n_T^* determined for that specific experimental condition.

Another collision parameter that is useful to know is the particle-wall collision number for a single particle (n) along the pipe length (L). This is estimate using the

particle collision in a 1-m pipe increment. At any given time the total number of collision in a 1m pipe ($n_{T,1m}$) and the number of particle in a 1-m pipe $N_{p,1m}$ are

$$n_{T,1m} = \left(\frac{1m}{V_s}\right) \cdot \left(\frac{V'_s}{s}\right) \Big|_{wall} \quad (3-32)$$

$$N_{p,1m} = \left(\frac{1m}{V_s}\right) \cdot N_m w \quad (3-33)$$

Where N_m is the number of particle in per unit mass and w is the average particle mass flow rate. The number of collision in a 1m pipe (i.e collision per length) is

$$n/L = \frac{n_{T,1m}}{N_{p,1m}} = \left(\frac{1}{N_m w}\right) \cdot \left(\frac{V'_s}{s}\right) \Big|_{wall} \quad (3-34)$$

The term n/L is useful for comparison of the particle collision in the pipe in each system; this term is independent of particle flow rate as well as pipe length. In an experimental setting, Matsusaka et al. (2002) found n/L to be around one collision per meter for 7 μ m particles in 4.6 mm pipe diameter with air velocity of 36-77 m/s.

Experiments

The values for the charging parameters are taken from Table 2-3. Experiments collecting the specific charge of particle at different pipe lengths and flow rates were performed using the experimental setup describe in Chapter 2 (Figure 2-2C and 2-2D). In these experiment four different pressure setting were used (refer to as setting 1 to 4). The flow rate and velocity for each pressure setting are listed in Table 3-3. The particle flow rates for these experiments are between 0.2 to 1.0 mg/s.

Simulation

CFD simulations were performed to match the experimental conditions that were used in the experiment (both the short pipe experiment, and the validation experiment). The inputs were measure for each experiment. The properties of the particles and the

pipe are listed in Table 3-4 and 3-5; unlike in Chapter 2, the particle diameters used are the count mean surface area diameter. The specular coefficient for each pipe was determined semi-empirically to be 0.02 for glass pipe and 0.08 for metal pipes (Bolio et al. 1995). The gas properties were taken at standard condition. Finally the coefficients of restitution used were taken from reported values in the work by various authors (Brauer 1980; Gondret et al. 2002; Sommerfield and Huber 1999). The coefficients of restitution are between 0.9 and 1. Grid size of 200 points in the radial passes the grid sensitivity test. The model was validated using the single-phase simulations for $Re = 7,000$ (Eggel et al. 1994), $Re = 21,800$ (Schildknecht et al. 1979), and $Re = 50,000$ (Laufer 1953). The velocity profile and the turbulent kinetic energy profile match that of the validation data. An example is shown for $Re = 21,800$ in Figure 3-1. The two-phase simulations were validated by Rao et al. (2011).

Results and Discussion

Particle-Wall Collision

CFD simulations were used to determine the particle-wall collision in the pipe. The outputs for CFD simulation were used along with Equation 3-28 through 3-34 to determine the two collision number, n_T^* and n/L . n/L for all the experiment performed were calculated to be between 0.1 to 1 collisions per meter, depending on the condition. The collision numbers are on the same order of magnitude as those observed in experiment by Matsusaka et al. (2002).

The validating experiments varied the operating condition (i.e. air velocity and particle flow rate). CFD simulations were performed to check the effect of each operating parameters on the collision number. The simulations were performed under a

typical condition for the soda lime particles in copper pipes; performing simulations for other particles and pipes also yields similar trends.

Figure 3-2 shows the collision number of the particle, n , traveling along a straight pipe. Each line in Figure 3-2 represents the gas velocity used in the validation experiment. In Figure 3-2, the particle mass flow rates were kept constant at 0.58 m/s. The simulations show that as flow velocity increases the number of collisions should increase as well. This result is expected. In general increasing the flow velocity increases the number of particle-wall collision in the pipe. Higher flow velocity increases the turbulent in the pipe. The higher the turbulent level in the flow will increase the likelihood of particle coming in contact with the wall. This result was found true when simulation were performed for other velocity as well. From this relationship, more charge transfer will be seen for experiments operating at higher velocity.

Another parameter that was varied in the experiments is the mass flow rate, w . In the simulation the changing the mass flow rate changes the mass loading term (see Table 3-2). The collision numbers along the pipe length were determined from the simulation at different mass loading this is shown in Figure 3-3. The relationship in Figure 3-3 indicates that as the particles flow rates entering the pipe increases, the fewer the collisions will occur for an individual particle. This would be possible when the addition of particles hindered the particle near the centerline from reaching the wall. These centerline particles will not collide with wall thus lower the average collision number. From this relationship, it is expected that less charge transfer will be observe when the mass flow rate increases. However the particle feeder used in the experiment

does not have the capability to precisely control the particle feed rate to test this effect. A parametric study of each parameter is presented in Appendix C.

Determining $n_{T,0}^*$

CFD simulation was done for each individual experiment ran in the short pipe experiments (Figure 2-2A and 2-2B) to determined the collision number, n . Under the assumption that the number of collision in the pipe is constant it is possible to convert L_0 (use in Equation 2-13) into $n_{T,0}^*$ (use in Equation 3-31). $n_{T,0}^*$ was determined using

$$n_{T,0}^* = L_0 \frac{n_T^*}{L} \quad (3-35)$$

n_T^* in Equation 3-35 is calculated using Equation 3-30 for the experimental condition specific to the experiment that was used to determined L_0 ; and L is 1 meter. Equation 3-35 directly converts the characteristic length L_0 into the characteristic collision number, $n_{T,0}^*$. $n_{T,0}^*$ for each particle-pipe system is also listed in Table 3-6. With L_0 and Equation 3-31, prediction of particle charge is possible but the operating condition must remain the same as the short pipe experiment as the number of collision changes with the operating condition. But with $n_{T,0}^*$ and Equation 3-31, we expect to be able to predict particle charging for the same particle pipe system but with different operating condition.

Comparisons to Experimental Results

Validation experiments were performed for each particle-pipe system at each pressure setting for pipe lengths of up to 4 m (see Figure 2-2C and 2-2D). A simulation was performed to match each experimental condition. The collision number determined under each condition was used with $n_{T,0}^*$ and $q_{m,\infty}$ to predict the particle charge. The predictive results are compared to the experimental results. Example results are shown

for soda lime particles in copper pipe (Figure 3-4) and JSC-1A in natural glass pipe (Figure 3-5). In both Figures 3-4 and 3-5, the points are the experimental measurement and the solid lines are the prediction made using CFD simulations. Each experiment was performed at different velocity (V_g) and particle mass flow rate (w); these are displayed for each figure. The collision number along the pipe length is also label in each figure. In both Figures 3-4 and 3-5, the general trend from the experiment is that as the flow velocity increases the amount of charge transfer to/from particle also increases, this is in agreement with the trend predicted in Figure 3-2.

In both figures, the predictions were able to capture the effect of impact charging. In Figure 3-4, the predicted results were very similar for each simulation; the soda lime-copper pipe system reaches equilibrium. The equilibrium charge was reach in the prediction but the experiment result did not reach equilibrium. This deviation is likely to due to experimental error and the environmental condition (i.e. humidity and temperature) and inhomogeneity of the pipe material causing some differences in $q_{m,\infty}$. This deviation did not cause significant changes in the prediction before reaching the equilibrium charge. The JSC-1A-natural glass pipe predictions in Figure 3-5 also show very good match with the experimental results when the particles had not reach the equilibrium charge. Similar results were seen for other particle-pipe system. The results for other particle-pipe system are in Appendix D.

Expanding the Prediction Model

Scale Up the Pipe-Line

The experiments were performed at a constant pipe size. In process design it is given that the pipe size will be scaled up in the actual processes; thus it is important to

validate that this predictive method will also be valid when the pipe size changes. In the current method, charge is transferred as a function of particle-wall collision. When changing the pipe size, not much is expected to change in the way particles impact the wall. The experiment and the method described in this work are expected to be valid when increasing or decreasing the pipe diameter. However it is necessary to test this hypothesis. In the future, experiments and simulations should be performed with different pipe diameters to determine whether it is possible to predicted particle charging for different pipe diameters. Doing so will validate the predictive technique for scaling up the pipeline.

Monitoring the Environmental Condition

While performing the experiments it was found that the environmental condition, namely the humidity and temperature, strongly affected the charge measured on the particle. We had speculated that both temperature and humidity mainly affect the equilibrium charge of the particle and the wall, but more testing is needed. In the future, this experiment should be performed in a control chamber. The humidity and the temperature should be accurately and easily controlled. The experiments measuring the equilibrium charge and the characteristic length should be performed under a range of relative humidities and temperatures. From this data it should be possible to create an empirical model that modifies the equilibrium charge and characteristic length between the two materials as a function of the relative humidity and temperature.

$$L_0=f(RH, T, L_0') \quad (3-36)$$

$$q_{m,\infty}=g(RH, T, q'_{m,\infty}) \quad (3-37)$$

RH is the relative humidity, T is the temperature, and the superscript indicates the measurement made at a reference condition possible at room temperature and dry air. We expected that these general functions f and g will be independent of the material properties, but that remains to be determined. Experiments should also be performed to check the validity of this model after including the environmental effect. This validation will take into account the day-to-day variation as well as the location.

Scaling the Particle Size

The current predictive method is only valid for the same particle size as the experiment. In some cases, it is important to change the particle size in the system. To take into account the changes in the particle diameter, it is important to know two different parameters: the surface of contact and the duration of contact. Next it is important to determine whether the charge transfer between the surfaces is limited by the surface area in contact, the duration of contact, or both. If the charge transfer occurs very slowly, a greater surface contact will not make a significant difference on the final charge on the particle. Thus the longer the contact, the longer the charge transfer. And in the other case, if the charge transfer occurs very quickly (as soon as the contact occurs) the contact surface will reach a charge equilibrium with the wall. The contact area between the two materials will control how much charge is transferred. The most likely scenario will be that the charge transfer is dependent on both the contact area and contact time. A model is needed to describe the charge transfer for a collision. Once the charge transfer model is made, it will be possible to convert the number of collisions used in the predictive equation to a new term including contact area and contact time.

Accounting for the Complex Flow Geometry

Ema et al. (2003) found that the charge transfer between the particles and the surfaces depends on the angle of impact. Charge transfers at certain angles were found to be as much as five times greater than direct collisions at 90°. Ema et al. indicated that this effect is due to the rolling and slipping motion of the particles. The highest charging efficiency occurs at a critical angle when particles switch from rolling to slipping.

In the current technique charge prediction is only valid for a straight pipe. In a straight pipe the angle of impact was found to be consistently around 80°; this effect can be neglected. However in a more complex pipeline (i.e. curved, bent, and split) the impact angle will change. In order to take into account the different angles of impact, first the critical angle in which slipping and rolling occurs should be determined. Theoretical models can be made to determine this based on the roughness of the two materials. Then it would be possible to incorporate this relation as

$$q_m = q_{m,0} \exp\left(-k_\theta \frac{n_T^*}{n_{T,0}^*}\right) + q_{m,\infty} \left\{1 - \exp\left(-k_\theta \frac{n_T^*}{n_{T,0}^*}\right)\right\} \quad (3-38)$$

where k_θ is the charging efficiency of the impact angle. Using this, we can perform simulations with different flow geometries to determine particle-wall collision as well as the average impact angle. With Equation 3-38 each section of the geometry needs to be modeled separately depending on the average impact angle.

It may be possible that the effect of the impact angle will tie into determining the particle-wall contact area and contact time. If what Ema et al. hypothesized is true, then the contact area will change depending on the rolling and slipping motion of the particle. But it is also important to take into account that when the particle is slipping and rolling, the charge transfer will also be different due to the friction created by the particle slip.

Summary

Particle charge in straight pipe was predicted using the particle-pipe parameters determined from an experiment along with the total number of particle-wall collisions determined with CFD simulation. For the experiments, particles were sent into a straight pipe, and the particle charge leaving the pipe was measured. By varying the initial charge it was possible to determine the particle-wall equilibrium charge and a charge transfer parameter. With this information a CFD simulation can be performed to determine particle-wall collision number for a single particle under any operating condition (gas velocity and particle flow rate). This prediction method worked well for both spherical particles and non-spherical particles. Determining of collision frequency is not limited to use of CFD simulation. CFD-DEM is also encouraged but will result in much higher simulation time. Excellent predictions were observed for different types of particle flowing through straight pipes for a range of gas velocities and particle mass flow rates.

Table 3-1. Term used in the turbulence and solid stress model

$$c_{T1}=1.4, c_{T1}=1.8, c_{T3}=1.2, c_{\mu}=0.09$$

$$f_{T1}=1$$

$$f_{T2} = \left[1 - \frac{2}{9} \exp \left\{ - \left(\frac{R_T}{6} \right)^2 \right\} \right] \left[1 - \exp \left\{ - \frac{y^+}{5} \right\} \right]^2$$

$$f_{\mu} = \left[1 - \exp \left(- \frac{y^+}{70} \right) \right] \left[1 + \frac{3.45}{\sqrt{R_T}} \right]$$

$$\sigma_k=1.4, \quad \sigma_{\varepsilon}=1.3$$

$$y^+ = \frac{U_T \rho_g}{\mu_g} (R-r)$$

$$R_T = \frac{\rho_g k^2}{\mu_{eg} \varepsilon}$$

$$G_{1k}=v$$

$$G_{1c}=4\eta v^2 g_0$$

$$G_{2k} = \frac{1}{\eta(2-\eta)g_0} \left[1 + \frac{8}{5} \eta v g_0 (3\eta-2) \right]$$

$$G_{2c} = \frac{1}{5(2-\eta)} \left[1 + \frac{8}{5} \eta v g_0 (3\eta-2) \right] + \frac{768\eta v^2 g_0}{25\pi}$$

$$G_{3k} = \frac{8}{\eta(41-33\eta)g_0} \left[1 + \frac{12}{5} \eta^2 v g_0 (4\eta-3) \right]$$

$$G_{3c} = \frac{96v}{5(41-33\eta)} \left[1 + \frac{16}{5\pi} \eta v g_0 (41\eta-3) + \frac{12}{5} \eta^2 v g_0 (4\eta-3) \right]$$

$$\eta = \frac{(1+e)}{2}$$

$$g_0 = \frac{v_0^{1/3}}{v_0^{1/3} - v^{1/3}}$$

Table 3-2. Inputs and outputs for the simulation

Parameter	Description
<u>Input</u>	
m	mass loading (-)
R	pipe radius (L)
μ_g	gas viscosity ($ML^{-1}T^{-1}$)
ρ_g	gas density (ML^{-3})
V_g	mean gas velocity (LT^{-1})
v_0	maximum solid volume fraction (-)
d_p	particle diameter (L)
ρ_s	particle density (ML^{-3})
ψ	sphericity (-)
e_p	particle-particle coefficient of restitution (-)
e_w	particle-wall coefficient of restitution (-)
ϕ	specularity coefficient (-)
<u>Output</u>	
v	solid volume fraction (-)
V_{gz}	gas velocity in the z-direction (LT^{-1})
V_{sz}	particle velocity z-direction (LT^{-1})
T	granular temperature (L^2T^{-2})
k	turbulent kinetic energy (L^2T^{-2})
ϵ	turbulent dissipation (L^2T^{-3})

Table 3-3. Air flow in each type of pipe at each pressure setting

Pipe	Pressure setting	Air flow rate (m^3/s)	Velocity (m/s)	Reynolds Number
Metal pipe (copper & Stainless steel)	1	0.000257	6.7	3120
	2	0.000482	12.5	5860
	3	0.000805	20.9	9760
	4	0.001290	33.5	15600
Glass pipe (natural glass and Pyrex)	1	0.000285	7.9	3560
	2	0.000534	14.7	6670
	3	0.000891	24.5	11100
	4	0.001420	39.3	17800

Table 3-4. Characteristics of particles used in the experiment

Material of particle	Density (kg/m ³)	Diameter (μm)	Sphericity	Maximum solid volume fraction
Borosilicate	2220	48	1.00	0.65
Soda lime	2580	75	1.00	0.65
PMMA	1380	50	1.00	0.65
Crush soda lime	2670	43	0.76	0.47
JSC-1A	3230	27	0.86	0.53

Table 3-5. Characteristic of pipes used in the experiment

Material of pipe	Inner diameter (m)	Specularity coefficient
Copper	0.0070	0.008
Stainless steel	0.0070	0.008
Natural glass	0.0068	0.002
Pyrex	0.0068	0.002

Table 3-6. Characteristic values for each particle in 1-m pipe

Material of particle	Material of pipe	$q_{m,\infty}$ (μC/kg)	L_0 (m)	$n_{T,0}^* \times 10^7$ (#)
Borosilicate	Copper	-59±4	3.9±0.3	67.4±5.8
	Stainless steel	-113±11	0.7±0.7	12.8±12.9
	Natural glass	711±19	11.3±0.5	115.1±4.8
	Pyrex	473±14	19.1±0.4	98.4±2.2
Soda lime	Copper	-17±3	3.1±0.4	23.0±2.8
	Stainless steel	-56±7	0.7±0.6	5.1±4.6
	Natural glass	212±7	10.3±0.3	44.8±1.3
	Pyrex	175±8	11.4±0.4	49.3±1.6
PMMA	Copper	766±27	1.7±0.7	14.9±5.8
	Stainless steel	1451±43	1.4±0.7	12.3±6.6
	Natural glass	504±21	1.9±0.6	11.3±3.7
	Pyrex	368±13	2.8±0.4	16.4±2.7
Crush soda lime	Copper	15±3	4.4±0.4	7.7±7.4
	Stainless steel	-6±2	1.9±0.4	32.8±7.9
	Natural glass	179±8	10.7±0.4	176.5±6.8
	Pyrex	285±9	22.2±0.4	365.6±6.0
JSC-1A (30-90 μm) sieve fraction	Copper	-105±6	3.6±0.4	130.3±14.1
	Stainless steel	-45±6	1.1±0.6	38.3±21.1
	Natural glass	265±7	8.1±0.3	179.0±6.5
	Pyrex	211±8	19.9±0.4	439.4±8.4

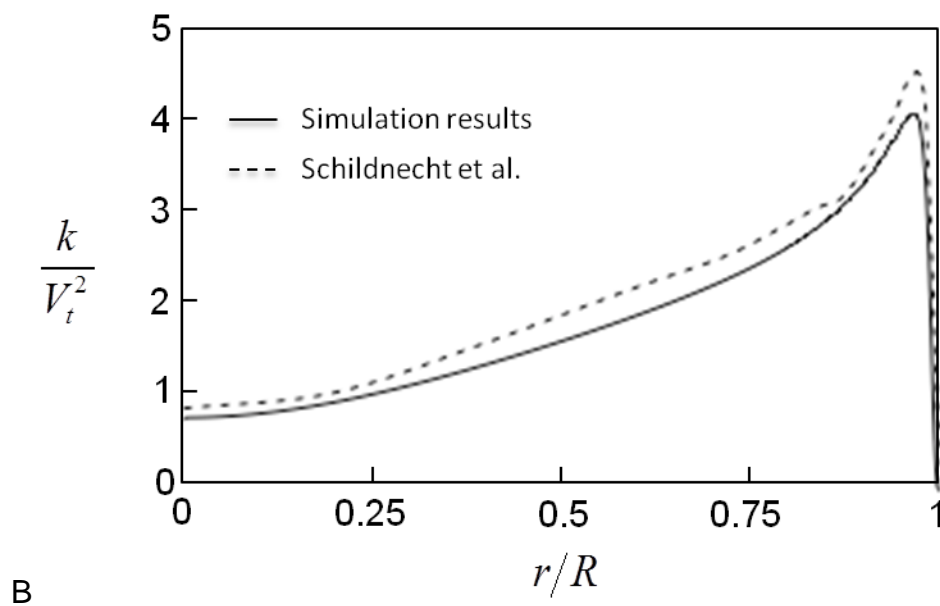
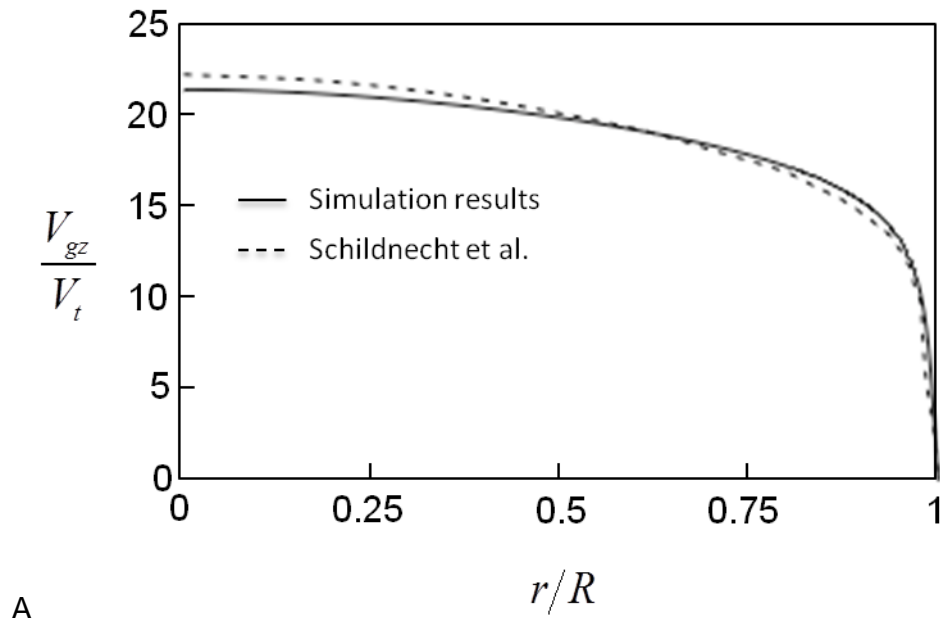


Figure 3-1. Comparison of single phase prediction to benchmark data by Schildnecht et al. (1979). A) Velocity profile. B) Turbulent production profile.

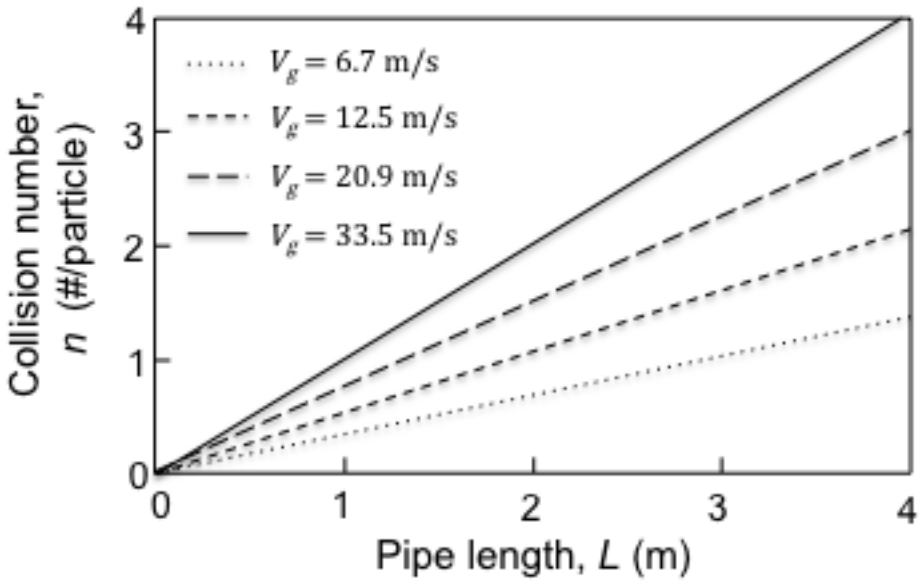


Figure 3-2. Collision number for soda lime particle in copper pipe at different velocities, the mass flow rate is constant at 0.58 mg/s

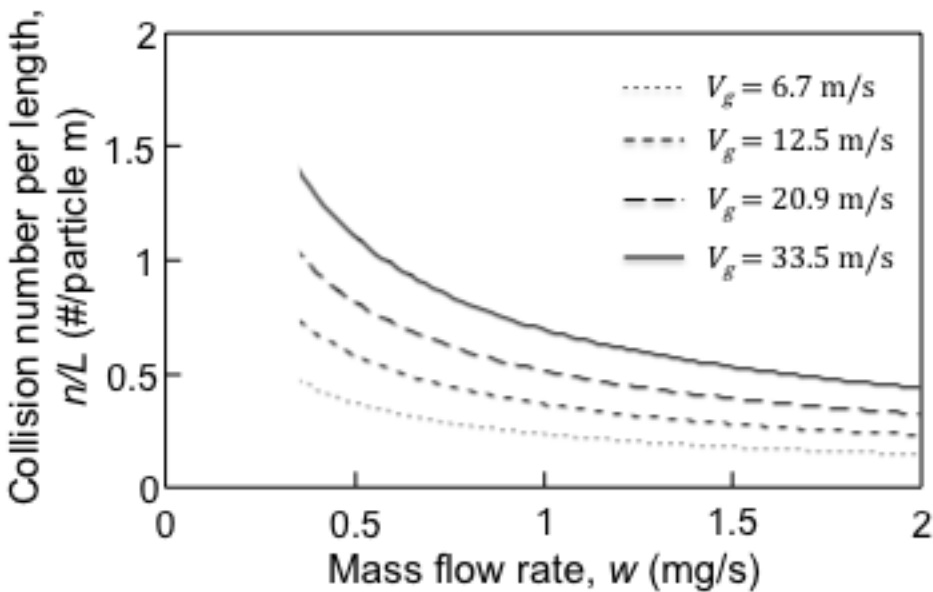


Figure 3-3. Collision number along the pipe for soda lime particle in copper pipe as a function of mass flow rate and velocity

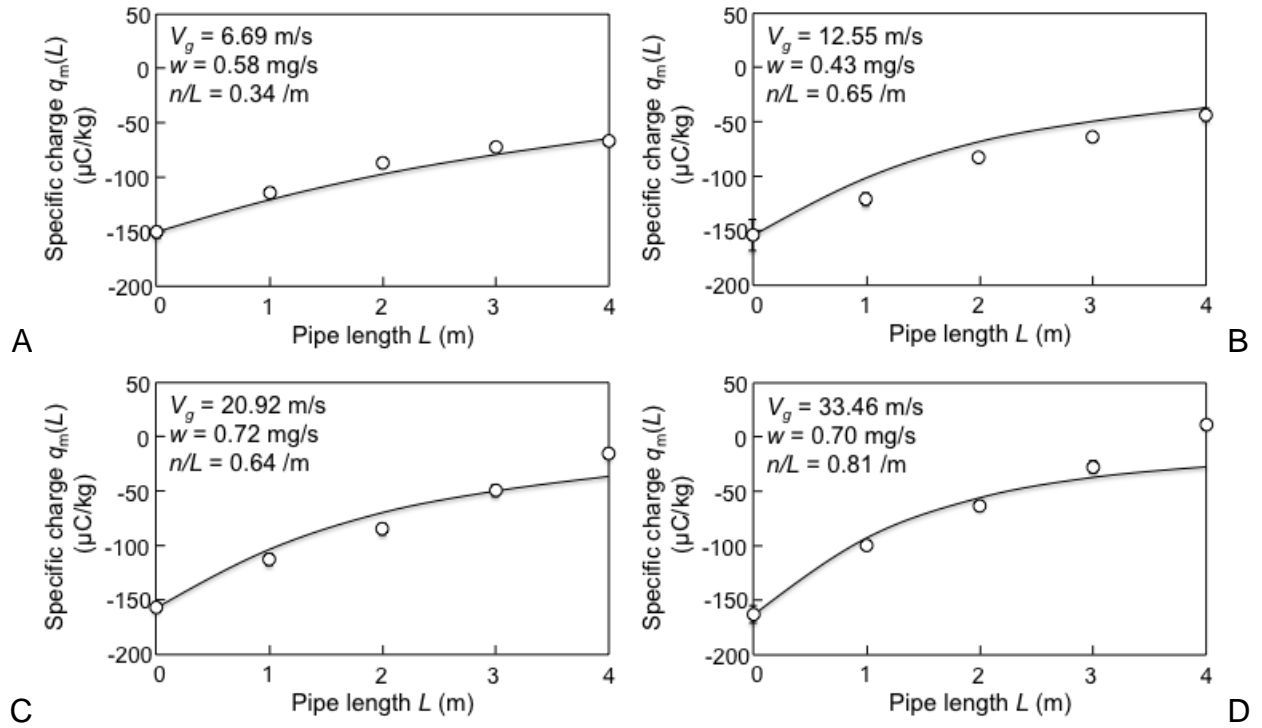


Figure 3-4. Predicted charging profile for soda lime particles in copper pipe for different air velocity and mass flow rates

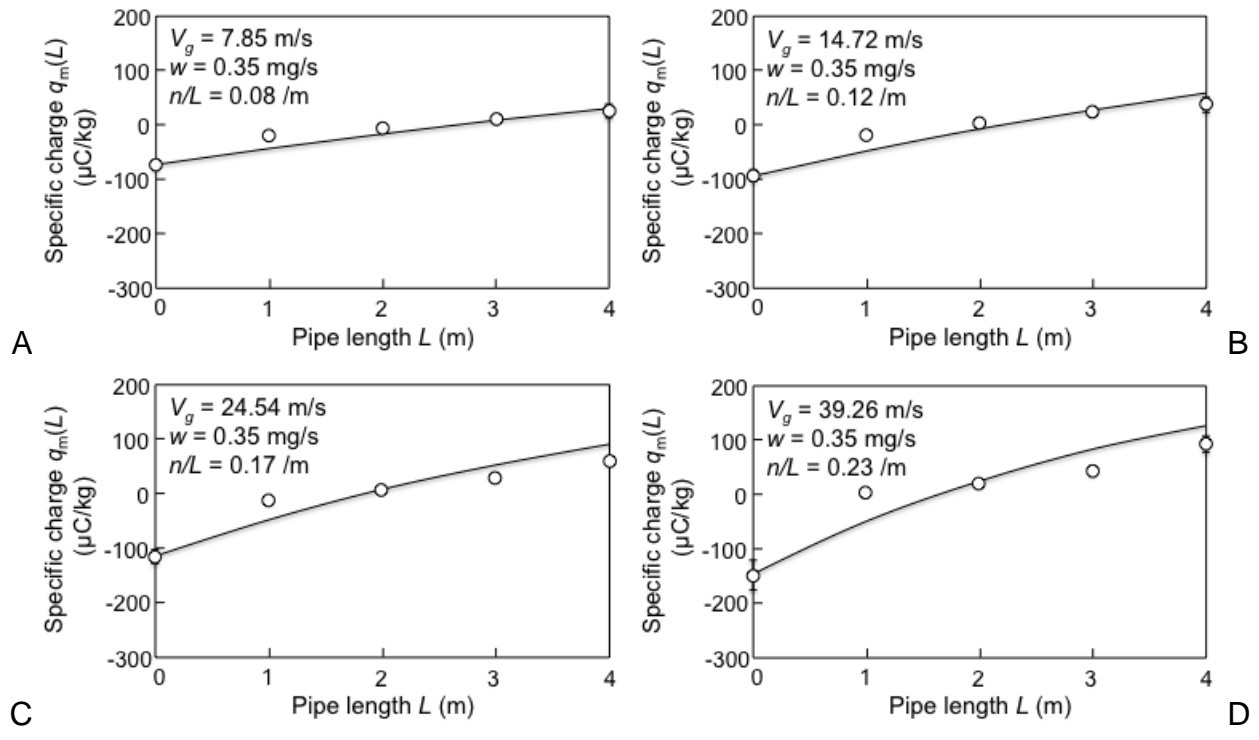


Figure 3-5. Predicted charging profile for JSC-1A particles in natural glass pipe for different air velocity and mass flow rates

CHAPTER 4 DEPOSITION OF CHARGED PARTICLES IN BIFURCATING AIRWAY

Background

The charge on a particle is affected by its properties, e.g. size and composition, as well as by the method of charging. The presence of charge in a particulate mixture can dramatically influence its flow behavior, and understanding this effect has the potential to improve many particulate processes, including those found in medicine (Bailey et al., 1998; Peart et al., 2003). For example, knowledge of the behavior of charged particles can lead to more efficient particle drug delivery systems using inhalers. Researchers have found that aerosols generated from inhalers contained some amount of charge on the particles (Kwok et al., 2005; Byron et al., 1997). Ali et al. (2009) measured the amount of charged particles generated from a commercial metered dose inhaler (MDI) and a dry powder inhaler (DPI) and found that up to 40% of the generated particles contained charges.

To date, researchers have performed experimental deposition studies with uncharged particles in airways; the common experimental technique that is employed is the single breath regional deposition (SBRD) technique (Brand et al. 2005; Ferin et al., 1983; Yu and Finlay, 2005). SBRD compares inhaled and exhaled particles to determine the amount of deposited particles but cannot provide local deposition pattern information. For local deposition patterns, visualization techniques such gamma camera, single-photon computed tomography (SPECT), and fluorescence are commonly used. Although gamma camera and SPECT can be used in-vivo, a clear deposition image requires a long acquisition time and a high dose of radiation (Biddiscombe et al., 1993; Brown et al., 2002; Eberl et al., 2001; Dunbar et al., 2002;

Dolovich and Labiris, 2004). Fluorescence techniques do not have these drawbacks, but they are limited to airway models and measurements are rather tedious. For example, Oldham et al. (2000) deposited fluorescence-tagged polystyrene particles into a silicone airway model of the lung and then the airway was cut in half and deposited particles were counted using a fluorescence microscope. Similarly, Kim and Fischer (1999) deposited urine-tagged oleic-acid particles in glass airway models and then local deposition was determined by dissolving, in water, the particles in each section. Both groups found that the majority of uncharged particles deposited near the regions where airway bifurcations occurred, with very little deposition occurring in the straight conduit sections of the airway, and even less in the inlet airway.

In comparison to uncharged particles, there is a paucity of research on charged particle deposition in airways. Melandri et al. (1983) and Prodi and Mularoni (1985) used the SBRD technique with human volunteers and found that charged particles deposit two times more than their uncharged counterpart. Chan et al. (1978) tagged Fe_2O_3 particles with a technetium-99m radiotracer, then aerosolized and charged the particles using a spinning-disc aerosol generator, to determine particle deposition in a rubber airway model of the human lung. The charging of the particles occurred by triboelectrification between the particles and the spinning disc, and the deposition patterns were determined using a gamma-counting system. Chan et al. also observed an increase in particle deposition for charged particles, with the enhancement in deposition greatest for particles less than 5 μm and occurring in the middle section of the trachea. Chan et al. concluded that the increase in deposition was due to the image

force - the attraction of a charged particle toward the wall due to the difference in electrical charge.

Complementary computational fluid dynamics (CFD) simulations and experiments of charged particle deposition in a single bifurcating glass airway model were recently performed by Leong et al. (2009). The particles were charged using corona charging, and an excessive amount of particles were deposited so that they could be viewed with the naked eye. They observed that uncharged particles deposit mainly in the bifurcating regions, which was attributed to inertial impaction and gravity, while the charged particles deposited on both the straight airway section and the bifurcating region. Their CFD simulations showed that the electrostatic force significantly increases deposition when particles are in the near wall region, and that the overall deposition efficiency for charged particles was four times greater than uncharged particles.

In this work, a relatively new, simple and non-intrusive technique – near infrared (NIR) fluorescence – was used to determine local particle deposition in a model airway. The electrospray technique was employed to vary the charge on the particle, as well as to consistently generate particles with varying morphologies. With this novel combination of techniques, the effects of particle charge and morphology are explored, and local deposition patterns can be easily detected and measured.

Electrospray Technique

Production of Charged, Spherical Particles

Electro-hydro dynamic atomization (electrospray) is capable of producing a constant stream of monodispersed particles from a liquid solution. A general schematic of an electrospray system is given in Figure 4-1. The spraying solution is pumped

through a small (mm) nozzle, and a high voltage is applied to the nozzle with a ground counter electrode positioned below the nozzle. At the tip of the spraying nozzle, the electrostatic force binds the spraying solution into a cone shape, known as the Taylor cone. The spraying solution then atomizes into droplets at the tip of the Taylor cone. Electro spray generates particles with a very narrow size distribution; these particles also contain an electrostatic charge, which can be controlled using corona discharge.

The particles that are generated by electro spray depend on the liquid solution properties; namely, the polymer concentration, density, surface tension, viscosity, and conductivity of the spraying solution. Hartman (1998) formulated a scaling law for electro spray, which defines the droplets generated from electro spray based on the physical properties of the solution. The scaling law is based upon two different spraying modes – the varicose break-up mode and the whipping mode. In the varicose break-up mode, the Taylor cone is stable; monodispersed particles are generated in this mode. In the whipping mode, the Taylor cone is no longer stable but is in constant movement; the liquid stream leaving the cone is in the form of a whip. The particles generated in the whipping mode are polydispersed.

The scaling law requires knowledge of the jet current (I) at the spraying cone. For a Newtonian fluid with a flat radial velocity profile in the spraying cone, the jet current is calculated by

$$I = 2.17(\gamma K Q)^{0.5} \quad (4-1)$$

where γ is the solution surface tension, K is the solution conductivity, and Q is the solution volumetric feed rate (Hartman, 1998). The scaling law approximates the droplet size generated in each spray mode as:

$$d_{d, varicose} = \left(\frac{16\rho_s \varepsilon_0 Q^3}{\gamma K} \right)^{\frac{1}{6}} \quad (4-2)$$

$$d_{d, whipping} = \left(0.8 \frac{288\varepsilon_0 \gamma Q^2}{l^2} \right)^{\frac{1}{3}} \quad (4-3)$$

where ε_0 is the permeability in a vacuum ($8.854 \times 10^{-12} \text{ C}^2/\text{Nm}^2$) and ρ_s is the density of the spraying solution. For a given solution and feed rate, the smaller of the two droplet sizes calculated for $d_{d, varicose}$ and $d_{d, whipping}$ from equations 2 and 3 indicates the stable break up of the droplet and gives the spraying mode. This smaller droplet size is $d_{droplet}$. The final solid particle formed after the solvent evaporates can then be calculated from

$$d_{particle} = \sqrt[3]{f \frac{\rho_s}{\rho_p} d_{droplet}^3} \quad (4-4)$$

where f is the mass fraction of the polymer solute, $d_{particle}$ is the diameter of the solid particle after the solvent evaporates, and ρ_p is the density of the polymer solute.

Additional details associated with the derivation of this scaling law can be found in Yurteri et al. (2010).

Production of Charged, Non-Spherical Particles

The production of non-spherical particles using electrospray is relatively new and the techniques not so well developed. Liu et al. (2008) have produced cup-shaped and polygonal-shaped particles and Bhaskar et al. (2010) have produced rod-shaped and disc-shaped particles. Both studies link the formation of non-spherical particles to the solvent properties, polymer concentration, and solution feed rate. Almeria et al. (2010) explained the formation of non-spherical particles due the solute entanglement network and breakup of the droplets.

Near Infrared (NIR) Spectroscopy

NIR spectroscopy uses NIR fluorophores to emit light with wavelength close to infrared light. NIR fluorophores are excited by light with a wavelength that is slightly longer than red light. NIR spectroscopy is a safer imaging alternative to radiotracers and overcomes auto-fluorescence issues associated with common green fluorophore. Previously, the FDA had approved only indocyanine green (ICG) fluorophore for use in humans. Recently, more NIR fluorophores have become commercially available for use in-vivo. The nature and availability of NIR fluorophores makes NIR spectroscopy a safe and relatively inexpensive alternative for analyzing particle deposition (Frangioni, 2003; Hilderbrand and Weissleder, 2010). In-vivo NIR usage has been well developed in areas such as the brain, heart, eye, and other vital organs (Frangioni, 2003). NIR techniques have also been used to detect cancer cells in the lungs. Troyan et al. (2009) found that NIR fluorescence was just as effective for in-vivo imaging as the conventional radiotracer.

Experiments

Bifurcating Model

The bifurcating airway model in this study is based on the first four airways of Weibel's Model A (Weibel, 1963). Weibel's Model A is a representative model for a healthy adult human lung. Weibel's model begins with the trachea, which is labeled as *generation 0* (G0). The G0 airway branches into two identical daughter airways, both called *generation 1* (G1). This branching sequence continues until G23. The angle between the two daughter airways is always 70 degrees. The dimensions of each generation are listed in Figure 4-1. The final airways, G3, were modified with barbed

fittings for additional use with a pump and filter; these airways are label as the *connector sections*.

The original Weibel model did not specify the azimuthal angle. However, Howatson Tawhai et al. (2000) indicated that the branching plane of the lung is, on average, at a 90 angle with respect to the preceding airway. Although further investigations by CT scans found that the angle less than 90 degrees (Nowak et al., 2003; Zhang and Kleinstreuer, 2002), the model system in this work was generated using 90 degrees to reduce the geometric complexity. The bifurcating airway model was glass blown using Corning 7740 Pyrex glass. Figure 4-2 presents a schematic of the bifurcating airway model.

Generation of Spherical Particles

Particles were poly(lactic-co-glycolic acid) (PLGA) polymer dyed with NIR fluorophore 3,3' Diethylthiatricarbocyanine iodide (Sigma-Aldrich). The spraying solution was 0.75% by wt. PLGA polymer in a 4:1 acetone-dichloromethane solution. Addition of the NIR dye to the solution increased its electrical conductivity. To keep the particle size and the fluorescence properties constant for all solutions, the NIR dye was added so that the spraying solutions had a constant electrical conductivity of $80 \mu S/m$. Figure 4-2 lists the properties of the solution used in the spherical particle experiments. The scaling law predicts that electro spraying with 1.1 mL/hour ($3.05 \times 10^{-10} \text{ m}^3/\text{s}$) solution feed rate will result in a varicose break-up mode with a final solid particle of $1.98 \mu\text{m}$.

Figure 4-3A shows a sample of the spherical particles generated; Figure 4-3B presents the particle size distribution, which is quite narrow. The average surface area diameter is $2.18 \mu\text{m}$ with a geometric standard deviation of 1.26. The small peak

between 1 and 2 microns may be due to the production of secondary particles. Particle size variations between experiments were minimal, varying less than 8%, and modifications in the particle charge did not affect the particle size.

Generation of Non-Spherical Particles

Rod-shaped particles were generated using PLGA in an acetone-ethyl-acetate solution. Figure 4-4 documents the effect of composition of the solvent mixture on the particle morphology. Guided by these results, the rod-shaped particles used in the experiments (Figure 4-5) were generated with a PLGA solution at a 0.75% by weight concentration in 6:4 acetone-ethyl acetate solution fed at 0.90 mL/hr ($2.50 \times 10^{-10} \text{ m}^3/\text{s}$). On average, the rod-shaped particles were 1.3 μm in diameter with an aspect ratio of 3.3. Although the rod-shaped particles were not as monodispersed as the spherical particles, there were minimal day-to-day variations in the generated particle mix.

Hollow-shell particles were produced by spraying a polyethylene glycol (PEG) solution with baking soda added following Marijnissen et al. 2010. Applying heat to the sprayed particles decomposes the baking soda embedded in the particle. The gas in the particle then expands and creates a hollow-shell particle similar to a balloon.

Unfortunately, this method only produced particles greater than 50 μm . Hence, the baking soda was eliminated and an alternate procedure was developed. A new solution of 4% by wt. of PEG (MW = 2000) in a 40:1 ethanol-carbonated water solution was fed at 0.5 mL/hour ($1.39 \times 10^{-10} \text{ m}^3/\text{s}$) and generated the hollow particles shown in Figure 4-6. In this case, the predicted particle size (Equation 4-4), before particle expansion, is 0.52 μm . Since the hollow particles require more time to evaporate, a 30cm long metal pipe was added to the experimental setup (shown in Figure 4-7) to accommodate the

slower evaporation rate of carbonated water used for particle generation. Figure 4-6 details PEG particles collected at different locations downstream from the spraying nozzle. These images show a marked increase in particle size as the solvent is evaporated and carbonated water emerges, causing particle to swell.

Experimental Setup

The electrospray chamber is oriented vertically and consists of five separate elements: the spraying nozzle, the spraying ring, the discharge needles, the metallic cone, and a particle charge measuring system (Figure 4-7). Solution is fed through the spraying nozzle using an automatic syringe dispenser (NE-500, New ERA Pump System Inc.). High voltages are applied to both the nozzle and the ring. Electrospraying occurs at the tip of the spraying nozzle with the spraying ring acting as a counter electrode. The potential difference between the nozzle and the ring atomizes the solution into droplets. An applied positive voltage generates a positively-charged particle. The charge of the generated particles can be modified using the discharge needles. For example, an applied negative voltage is used to neutralize a positively-charged particle. Depending on the level of applied voltage, the particle can be fully or partially neutralized. The spraying nozzle, ring, and the discharge needle were encased in a cylindrical tube made of borosilicate II glass ($L = 0.305$ m, $ID = 0.102$ m). The particles then flow into a metal cone, 0.254 m in length, tapered to gradually reduce the flow diameter from the glass tube to the opening of the bifurcating airway model. The gradual reduction in diameter of the cone minimizes turbulence effects, and the cone can also be used to filter out particles. For example, if positive voltage is applied to the cone, the cone will attract and collect negatively charged particles at the wall before they exit the cone.

The average particle charge is monitored in real time using a charge-measurement system composed of a ring probe and an electrometer (6514 system electrometer, Keithley Instrument Inc.) following the charge-measurement systems of Vercoulen (1995) and Gajewski (1985; 1997). When a charged particle moves toward the ring probe, the particle induces a current in the ring, which is sent to the electrometer. The current measurement is directly related to the charge on the particle. For a stream of particles with a constant flux, the current reading remains constant over time. The ring probe is placed outside of the airway and does not come into contact with particles. The ring probe is encased in a grounded shield to prevent interference from any external electrical fields. The charge reading from the ring probe is not the true charge of the particles as the signals are affected by the material properties of the ring probe and shielding. Hence, calibration with a Faraday cup is used to determine the true charge of the particles. After passing through the charge-measurement system, the particles then flow through Tygon tubing and enter the airway model.

During the experiment, the generated particles are carried downward towards the airway model using compressed air entering from the top of the chamber. A sheath of air flows near the wall to keep particles from depositing there. Total airflow in the chamber (compressed air and sheath flow) was 28 LPM ($0.000467 \text{ m}^3/\text{s}$), controlled using rotometers. Since the electrospray chamber is 0.610 m in length, it takes about 5 seconds for the particles to flow from the spraying nozzle to the airway model, ensuring sufficient time for the solvent to evaporate to form the solid particle. The constant particle flux ($\sim 0.1 \text{ mg}/\text{min}$) is measured separately by collecting particles in a filter

placed after the ring. The relative humidity for these experiments was approximately 74%.

Four high voltage DC power supplies (HCN 35-20000 and HCL 35-20000, Fug; Series 230, Berton Associates Inc.) are connected to the spraying nozzle, spraying ring, discharge needle, and metallic cone. To generate positively-charged particles, positive voltage is applied to the spraying nozzle, spraying ring, and metallic cone while low negative voltage is applied to the discharge needles. To generate negatively-charged particles, the polarity used to generate the positively-charged particles is reversed. Neutral particles can be made by applying the same voltage as either the positively- or negatively-charged particles but with higher voltage at the discharge needle and grounded metallic cone.

Characterizing Neutrally-Charged Particles

In the case of zero charge reading from the charge-measurement system, it was unclear whether the particle mix contained both positive and negative charges, which cancel out for the overall neutral charge or whether individual particles were without any charge. An additional experiment was used to determine the particle charging. A parallel plate capacitor and a faraday cup were positioned after the electrospray chamber, as shown in Figure 4-8. A voltage was applied to one plate while the other plate was grounded. Changing the voltage on the parallel plate capacitor filters out the particles of different charges, resulting in changes in the measured charge for particles collected in the faraday cup over a one minute time interval.

Figure 4-9 presents the magnitude of the charge collected from such a test for positive, neutral and negative readings from the charge-measurement systems. Positively-charged particles (Figure 4-9A) show a positive gain in voltage when positive

voltage is applied to the plate, and the opposite is true for negatively-charged particles (Figure 4-9C). This confirms that a positive reading from the charge-measurement system yielded a mix of all positive particles and vice versa for the negative particles. Figure 4-9B, for the neutral particles, exhibits a charge collected that is minimally positive but not detectable in the charge-measurement system. However, with the neutral particles, the reading from the faraday cup also exhibited instances when the voltage reading decreased. The decrease in voltage indicates the presence of negatively-charged particles. Hence, the particles are not completely neutral, but rather consist of a mix of positively and negatively-charged particles with (almost) “zero” net charge.

Particle Deposition

Particles were sprayed until steady state conditions were achieved in the chamber. At steady state, the particle flux, particle size, and particle charge exiting the spraying chamber were constant. The priming period necessary to achieve steady state took up to four hours. Once the spraying chamber is at steady state, the airway model is attached and particles are collected for a four hour period. This collection period could be reduced by using an improved emission filter, better matching the emission wavelength (as discussed in the next section) or by using another dye.

NIR Imaging

The IVIS Lumina medical imaging system (Caliper Life Science) was used to visualize the particle deposition. The IVIS Lumina is capable of generating excitation light at a specific range of wavelengths and collecting the resulting emission light at a different range of wavelengths. The optimum excitation and emission wavelengths for the specific NIR dye in the PLGA polymer were determined using the Nanolog

Spectrofluorometer (Horiba Scientific). Samples of thin polymer film, made by evaporating the spraying solution on a glass slide, were used to obtain these wavelengths giving the highest fluorescence signals. The optimum excitation and emission wavelength are 690 nm and 780 nm, respectively, as shown in Figure 4-10. Based on the optimal excitation and emission wavelengths, the best available ICG background excitation and emission filters (665-695nm and 810-875nm, respectively) were selected to correspond to these wavelengths.

Operating conditions for the IVIS Lumina were also optimized for the highest signal-to-noise ratio. The best signal-to-noise ratio was found to occur at 20 seconds integration time and the largest aperture. Black tape was used to reduce reflection and to block-out the signal to prevent counting photons from different airway sections. In order to calibrate the IVIS signal, known masses of polymers, with a constant concentration of NIR dye (as used in the experiments), were placed into the IVIS Lumina along with the airway model. The standards relate the photon count to the polymer mass. The relation between photon count and polymer mass in a single ROI was consistently found to be:

$$\text{Photon Counts} = 1.340 \times 10^{10} m + 1.318 \times 10^4 \quad (4-5)$$

where m is the mass of the polymer in grams. The photon count in the case of zero polymer mass was that given off by the background in the IVIS Lumina chamber. Since lighting influences the photon counts, the airway model and the standards were placed in the same location and orientation for all deposition experiments. The photon count variation between two images of a single experiment was less than 5%. The connector sections at the end of airway model were not included in the deposition analysis as the

amount of particles deposited in that section varied greatly day-to-day due to the sharp reduction in airway diameter (see Figure 4-2).

Results

For each deposition experiment, two IVIS Lumina images were taken. The first was an ordinary photograph; the second was an image showing the fluorescence signal. By overlaying the two images, the resulting picture presents the particle deposition in specific locations of the airways. Figures 4-11 through 4-17 are generated in this manner, and all are displayed with the same color scale for the photon count. Since the airway model could not be imaged in a single picture, multiple images were taken for each experiment. Figure 4-11 gives the images associated with the various sections in the airway model for the case in which no particles were deposited and no fluorescence signal is detected. Each section was divided up into region of interests (ROIs) (Figure 4-12) of constant area to determine the photon counts in that section (Figure 4-12).

Deposition of “Neutral” Spheres

Figure 4-13 shows a representative deposition pattern with the IVIS Lumina after four hours of deposition testing. In the image, yellow/orange/red color indicates where particles have deposited, with the yellow regions indicating the highest particle deposition. Figure 4-3 shows the percentage of the total mass deposition from airway 0 to bifurcation 2. The average and standard deviations values are based on three experiments performed on different days. Information regarding deposition dynamics was also obtained at three different times during the deposition process; these images are shown in Figure 4-14. The total photon counts are displayed in the upper right corner of each image.

These “neutral” spheres exhibited a steady build up of particles in all sections of the airway as more particles were deposited. This deposition pattern is different than what is expected for uncharged spheres. For uncharged spheres, the bulk of the deposition occurs at the airway bifurcations due to particle inertia and impaction (Oldham et al. (2000); Kim and Fisher (1999)). However, in Figures 4-13 and 4-14, there is deposition in the bifurcating region, as well as the conduit airway. This difference in deposition is likely due to the small positive charge the particles hold. This hypothesis is based on the fact that the airway models of Oldham and Kim and Fischer are smaller than the one used here, Hence, it would be expected that the deposition in the conduit airway would be less in the present case, rather than greater, unless there were some other factor or mechanism, such as particle charge, present.

Deposition of Positively-Charged Spheres

Positively-charged spheres (4.64×10^{-19} C/particle) were used in this part of the study. The deposition of positively-charged spheres proved to be more troublesome than “neutral” spheres. The positively-charged spheres deposited on the wall near the region of particle generation; this drastically reduced the particle flux entering the airway. A ground wire was wrapped around the glass section of the spraying chamber to reduce any patch charges on the glass surface. Humidity is another issue that directly affects deposition for positively-charged spheres. At high humidity (>80% RH), no detectable particle flux entered the model. To obtain a strong measurable signal, the deposition experiments were carried out under a relative humidity below 50% and the resulting flux was consistently 0.13 mg/minute. Although the use of grounding wire and reduced humidity testing were not performed for the “neutral” spheres, the particle flux

should also increase under these conditions and the deposition patterns should remain the same.

Figure 4-15 presents the deposition of positively-charged spheres after four hours of testing; Figure 4-3 gives the deposition mass percentages of the positively-charged spheres. Positively-charged spheres deposit much more strongly than the “neutral” particles in the earlier section of the model, and very little charged particle deposition occurs in airway 2 in comparison to the “neutral” spheres deposition. This observation is likely due to space charge effects in which like-charged particles in the particle cloud repel each other, pushing particles towards the wall much more quickly than in the “neutral” particle case.

Figure 4-16 documents the dynamics of the deposition of positively-charged spheres at three different times during the particle deposition process. Positively-charged spheres do not exhibit the same steady build up of particles in each section as seen with “neutral particles”. Rather, positively-charged spheres initially deposit near the entrance (airway 0) of the model. The deposition in airway 0 continues until a saturation in particle deposition is reached, and then deposition begins in the next region downstream. Positively-charged particles only deposit at clean surfaces of the airway due to particle-particle repulsion from previously deposited particles, and this gives rise to the particle deposition downstream.

Deposition of Non-Spherical Particles

For non-spherical particles, experiments were performed with “neutral” charge on the particles. The deposition images for the rod-shaped particles are displayed in Figure 4-17A; the mass percent depositions in each section are given in Figure 4-3. In comparison to the “neutral” spheres deposition, a small increase in rod-shaped particles

deposition was found in the upper section of the airway model. In addition, it was visually observed that the depositions of particles in each straight conduit section of the airway were in patches as depicted in the sketch shown in Figure 4-17B. When a rod-shaped particle deposits on the wall, a portion of the rod-shaped particle will likely protrude, acting as a seed such that electrostatic effects pull other rod-shaped particles to the seed particle to deposit. As particles continue to pile onto the seed particles, this gives rise to the formation of the deposition patches.

Hollow, balloon-shaped particles were also delivered into the airway at a mass flow rate of approximately 0.02 g/min, which is lower than the spherical particles. Nevertheless, the flow rate in terms of particle number was twice as high as the spherical particles. Knowing the mass flow rate, the size of the solid particle (0.52 μm) before expansion, and the solid particle density, the flow rate in terms of particle number is calculated. Even with this significant increase in flow rate in terms of particle number, negligible amounts of the hollow, balloon-shaped particles were collected in the airway after 8 hours of deposition. It is expected that the low density, hollow particles behave in a similar fashion to submicron particles in which very little deposition occurs in the airways. However, when hollow, balloon-shaped particles penetrate deep into the airways, a greater amount of deposition is expected due to interception.

Concentration of the Deposited Particles

The mass percent deposition of “neutral” spheres, positively-charged spheres, and rod-shaped particles (data given in Figure 4-3) are normalized with the surface area in each of the deposition sections to obtain particle concentration information in the airway model. The surface area of each section is estimated using a 3D auto-CAD model of the airway. Figure 4-4 presents these particle concentration values, as well as

the total surface area, in each section. For all cases, by far, the highest particle concentration is located in the bifurcating sections. For “neutral” spheres and rod-shaped particles, deposition concentration increases as the airway size reduces. For positively-charged spheres, the deposition concentration in the bifurcating section is also much higher than the branching section, but the particle concentrations comparing airways 0 and 1, as well as comparing bifurcations 0 and 1, are similar, indicating a saturation for particle deposition in those regions.

Summary

Charged particles embedded with NIR dye were generated by electrospray and deposited in a glass airway model. The deposition of charged particles was visualized with an IVIS Lumina system. The NIR visualization technique proved to be an easy-to-use, non-intrusive method to quickly quantify particle deposition. The NIR technique also has great potential to provide a safe and inexpensive way to visualize in-vivo particle deposition. Further investigation using this technique is warranted - for example, matching excitation and emission wavelengths to minimize the deposition time.

Charged particles were found to deposit differently from uncharged particles. Charged particles deposit in both the conduit airways as well as the bifurcation region, as opposed to just the region near the bifurcation. How charged spheres deposit is also a function of the distribution of charges within the particle cloud. Spheres with zero net charge show a gradual build up of particles on all airway surfaces over time. Spheres with only positively-charged particles initial deposit preferentially in the upper section of the airway, then more deposition occurs downstream over time. For “neutral”, rod-shaped particles, deposition occurs in patches along the airways. Hollow, balloon-

shaped particles are conveyed through all four branches of the airway without depositing.

Table 4-1. Dimension of the bifurcating airway model

Airway	Number of Airway	D (m)	L (m)
G_0	1	0.0180	0.1200
G_1	2	0.0122	0.0476
G_2	4	0.0083	0.0190
G_3	8	0.0056	0.0076

Table 4-2. Electro spray solution properties

	Solution for spheres	Solution for hollow balloon-shaped particles
Polymer	PLGA	PEG
Weight concentration (%)	0.75% by wt.	4.00% by wt.
ρ_s (kg/m ³)	874	894
ρ_p (kg/m ³)	1200	2900
γ (N/m)	0.0245	0.0241
μ (Pa·s)	4.70×10^{-3}	4.85×10^{-3}
K (S/m)	80×10^{-6}	2570×10^{-6}
Q (m ³ /s)	3.05×10^{-10}	2.78×10^{-10}

Table 4-3. Mass percent deposition of “neutral,” positively-charged, and rod-shaped particles

	“Neutral” particles	Positively-charged particles	Rod-shaped particles
Airway 0	29.60% ± 4.60%	47.29% ± 5.58%	36.79% ± 5.38%
Bifurcation 0	7.40% ± 0.65%	14.78% ± 4.48%	12.72% ± 2.05%
Airway 1	18.54% ± 1.59%	20.94% ± 1.49%	13.52% ± 2.61%
Bifurcation 1	16.03% ± 2.42%	9.34% ± 1.81%	12.67% ± 3.65%
Airway 2	10.14% ± 0.78%	3.64% ± 0.62%	5.61% ± 1.70%
Bifurcation 2	18.29% ± 2.59%	4.01% ± 0.52%	18.69% ± 1.76%

Table 4-4. Total surface area in each airway section and the average deposition concentration of “neutral,” positively-charged particles, and rod-shaped particles

	Total surface area (mm ²)	“Neutral” particles (g/m ²)	Positively-charged particles (g/m ²)	Rod-shaped particles (g/m ²)
Airway 0	6130	48	77	60
Bifurcation 0	503	147	294	253
Airway 1	3011	61	69	45
Bifurcation 1	436	367	214	290
Airway 2	1129	76	27	42
Bifurcation 2	396	465	102	476

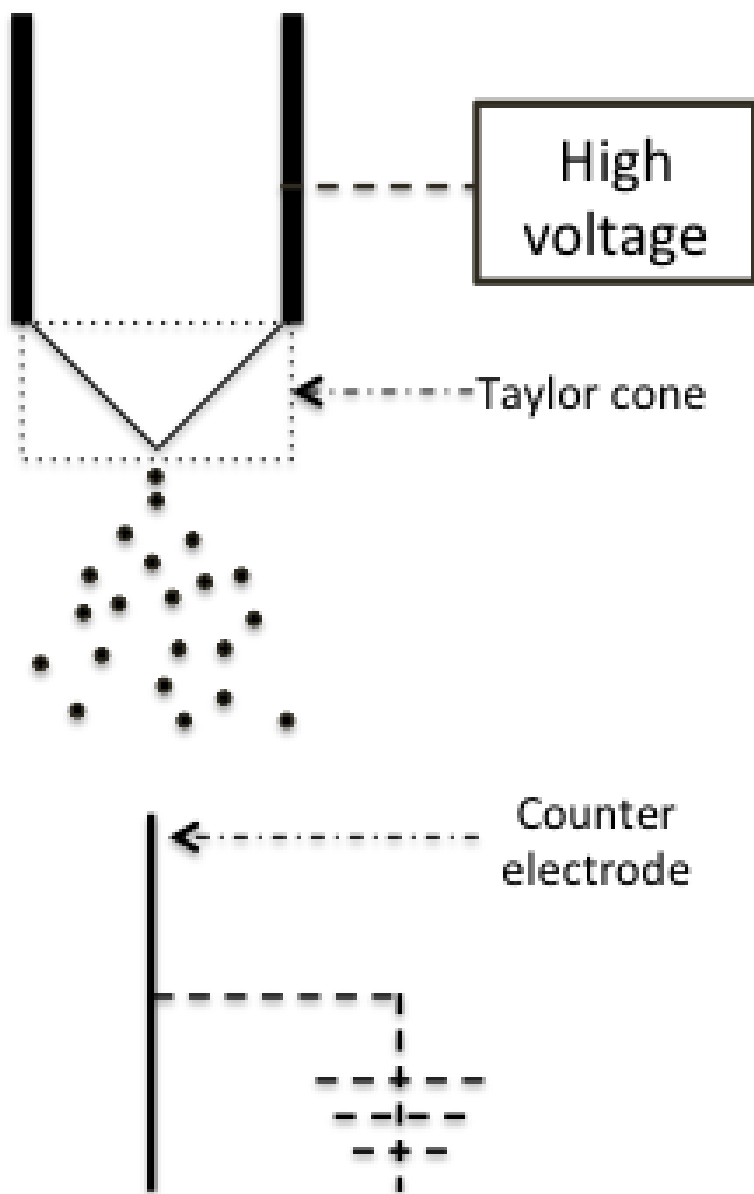


Figure 4-1. Schematic of electro spray

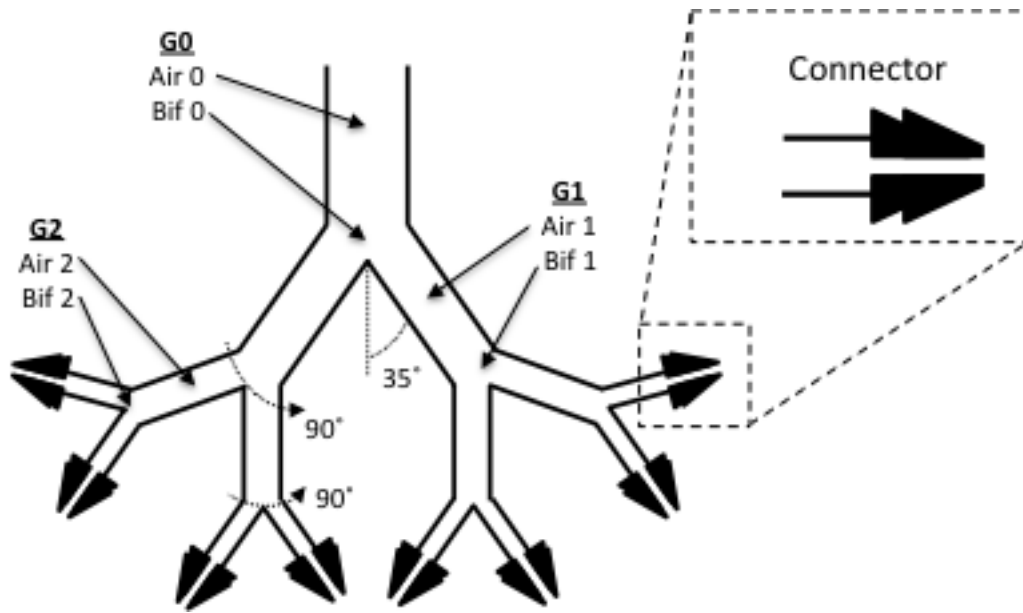


Figure 4-2. Schematic of the bifurcating airway model

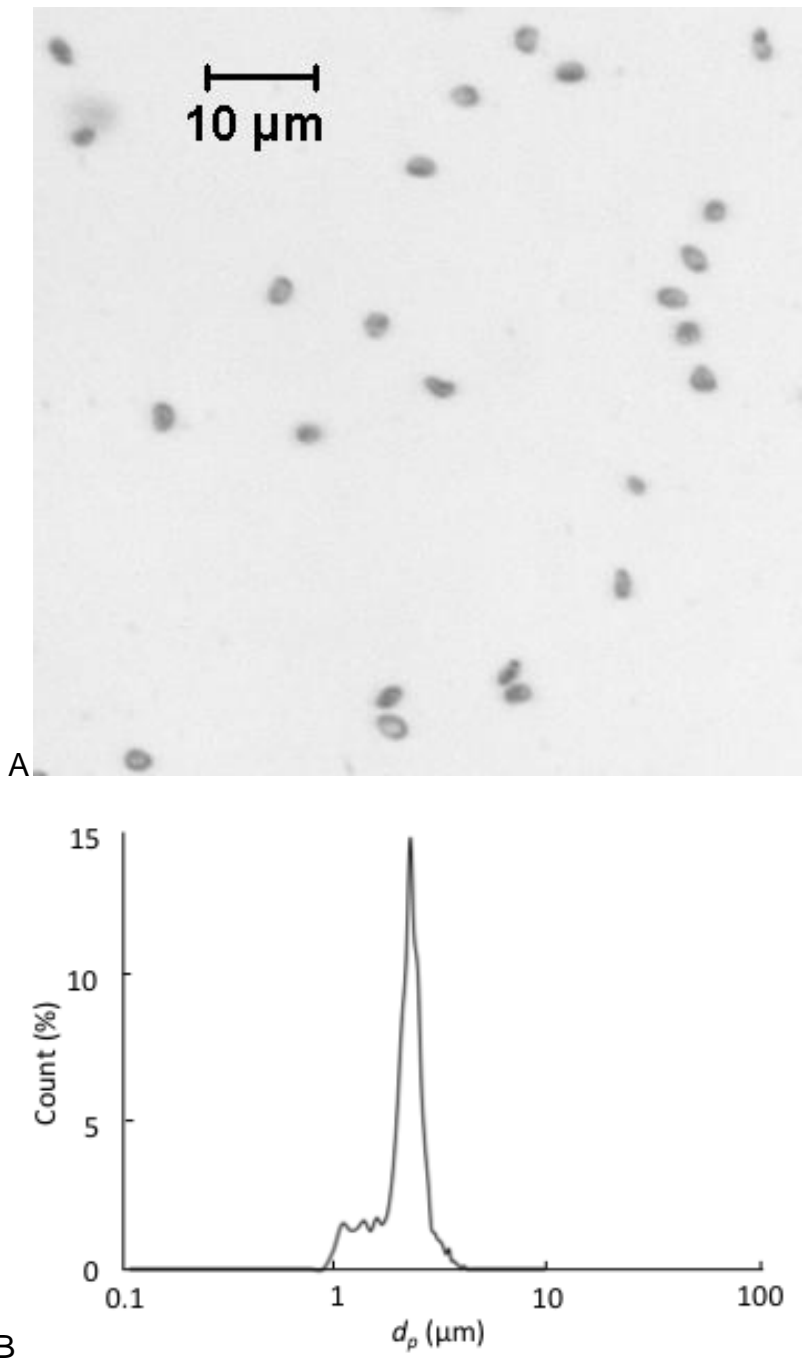


Figure 4-3. Properties of spherical particles. A) Microscopic image. B) Particle size distribution.

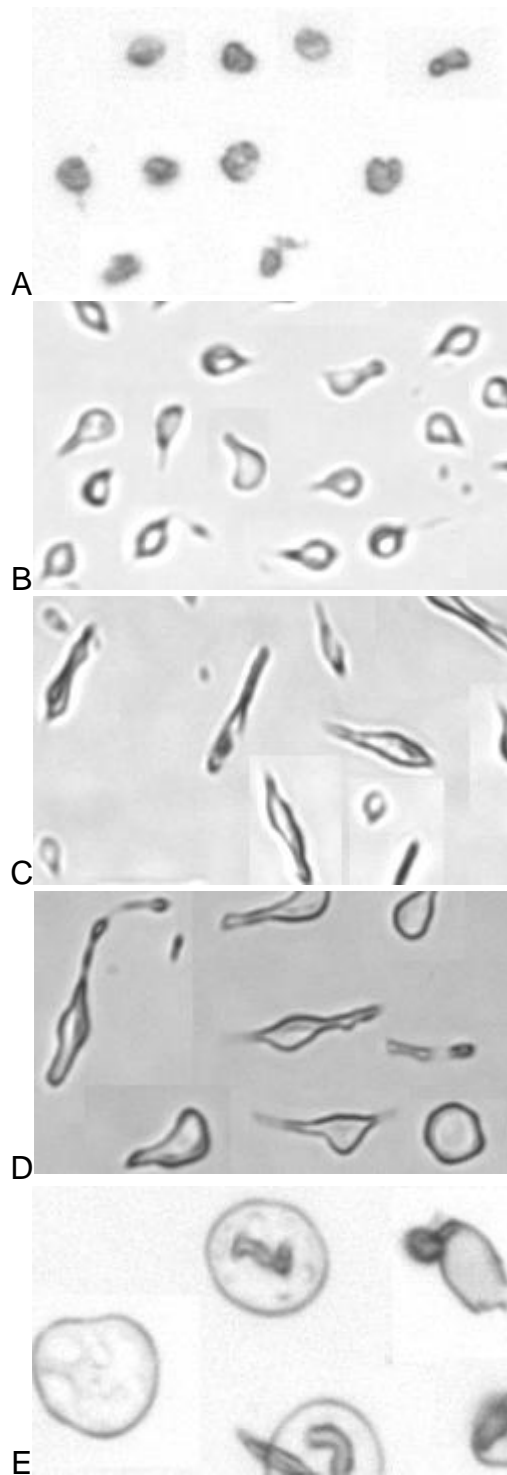


Figure 4-4. PLGA particles generated in various solvents. A) Acetone, B) 67:33 acetone-ethyl acetate, C) 50:50 acetone-ethyl acetate, D) 33:67 acetone-ethyl acetate, and E) Ethyl acetate. Sprayed with 2.78×10^{-10} m³/s spray of 1% by wt. PLGA.



Figure 4-5. Microscopic images of rod-shaped particles

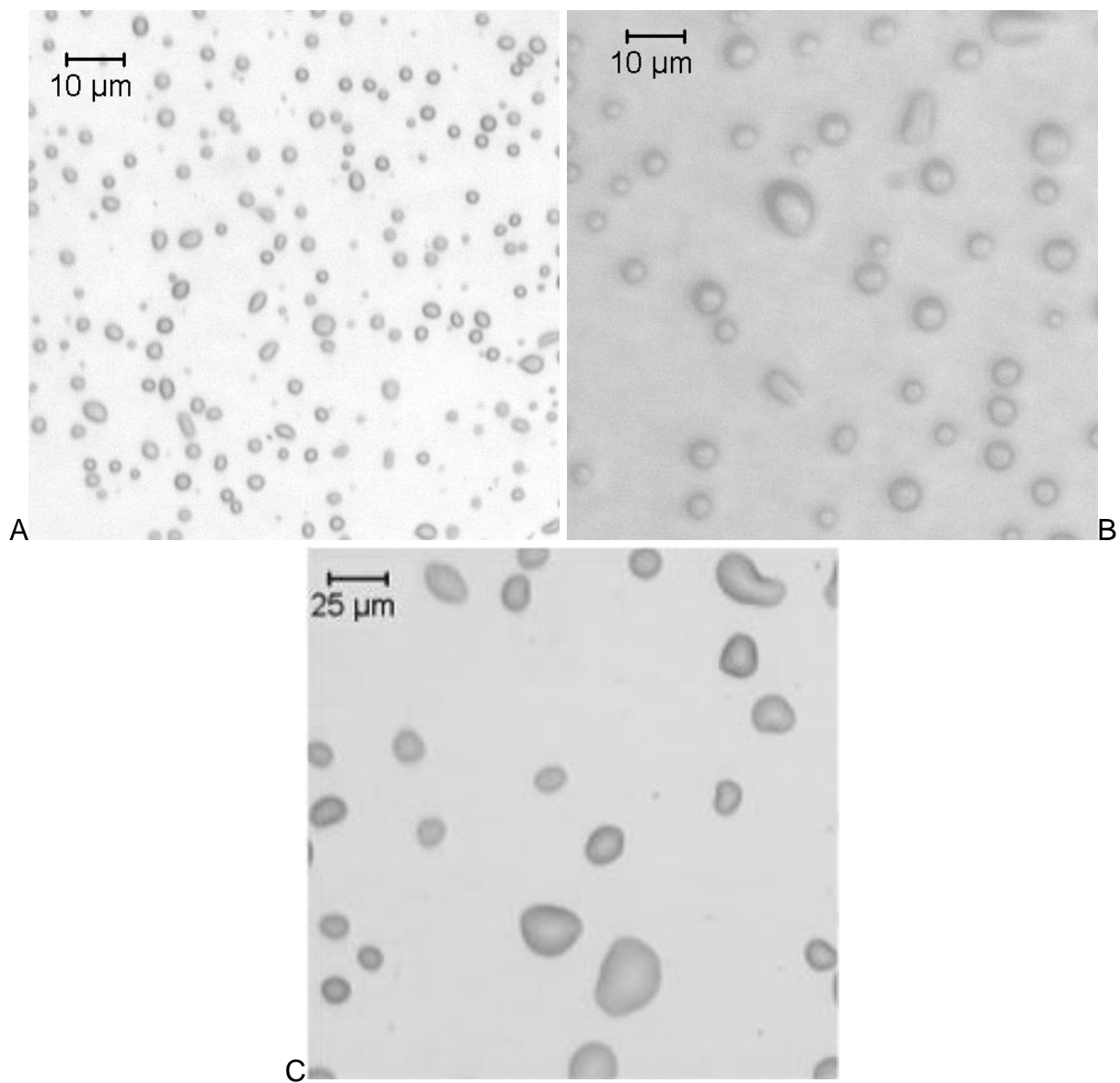


Figure 4-6. Microscopic images of hollow, balloon-shaped particles collected at different location. A) The spraying nozzle. B) The discharge needles (6 cm downstream from the spraying nozzle). C) The charge-measurement system (690 cm downstream from the spraying nozzle).

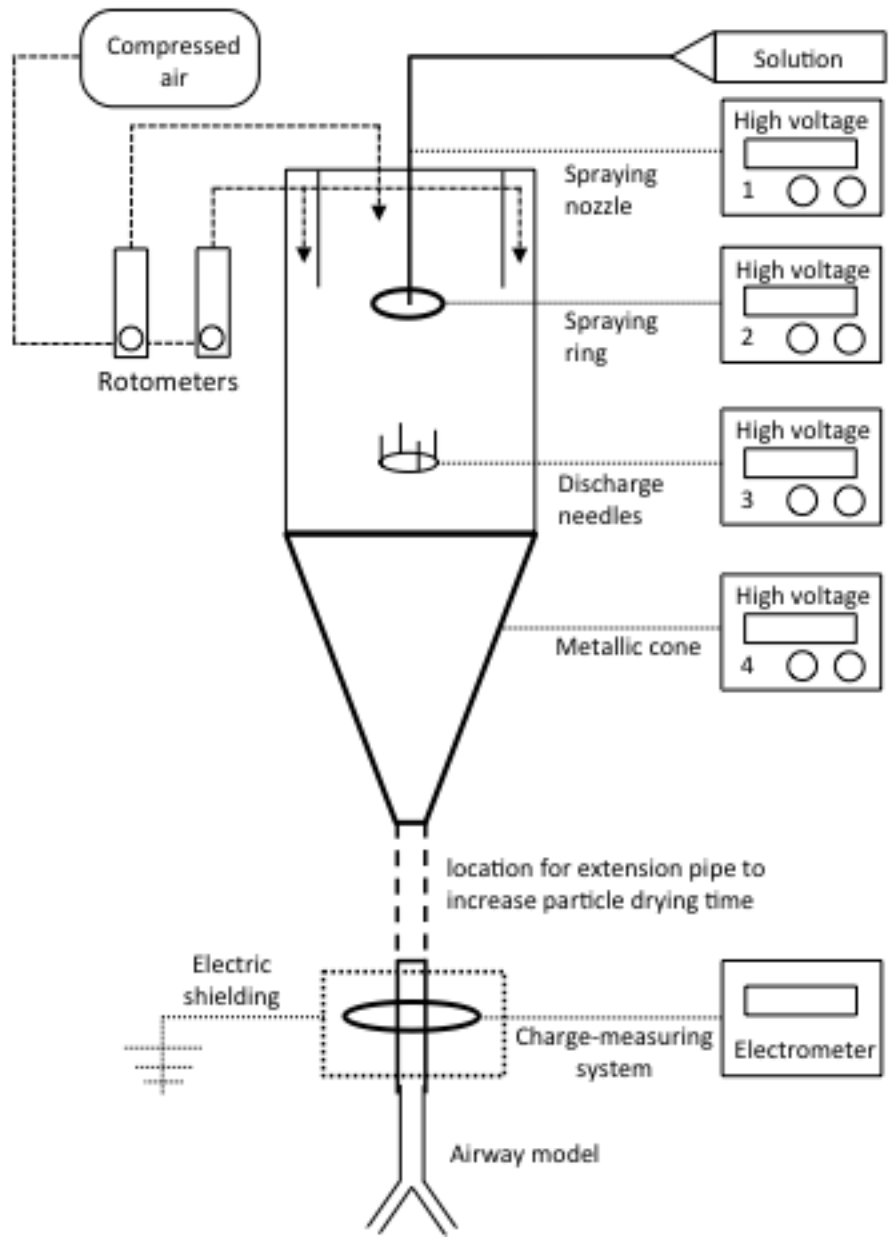


Figure 4-7. Experimental setup

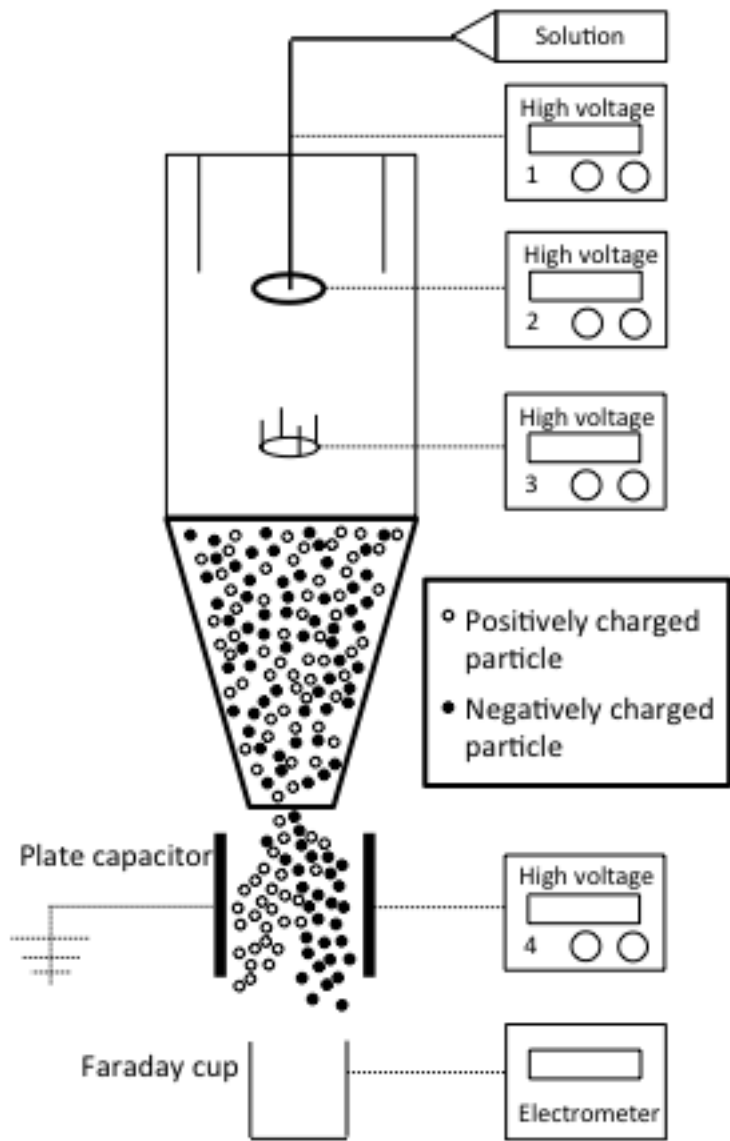
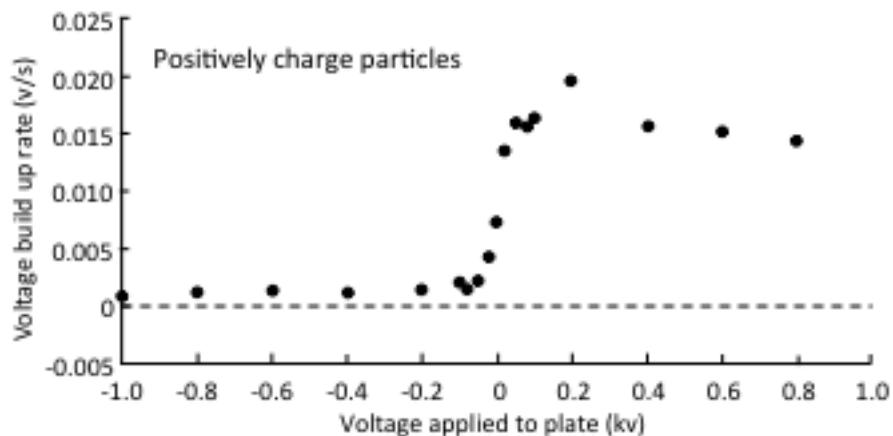
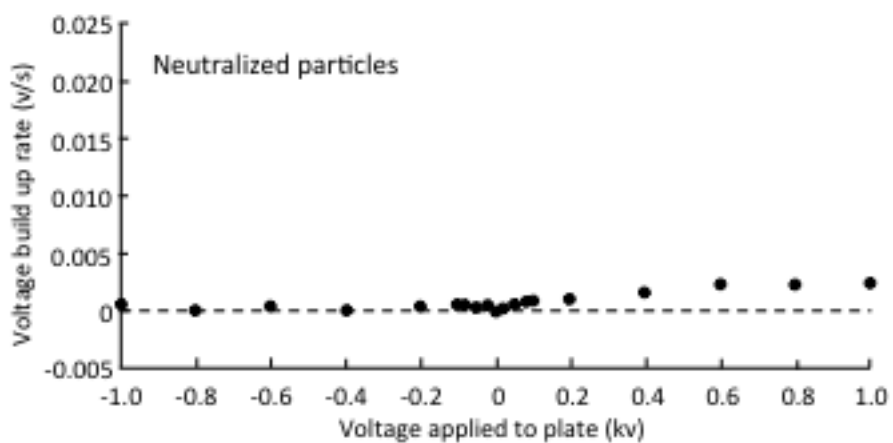


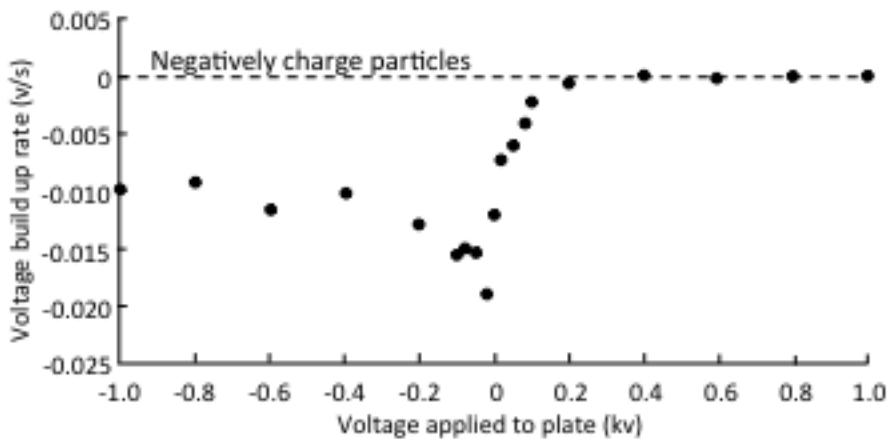
Figure 4-8. Experimental setup using a parallel plate capacitor to characterize the charge of the particle mixtures



A



B



C

Figure 4-9. Voltage build-up rates in the Faraday cup at different plate voltages. A) Positively-charged particles. B) "Neutral" particles. C) Negatively-charged particles.

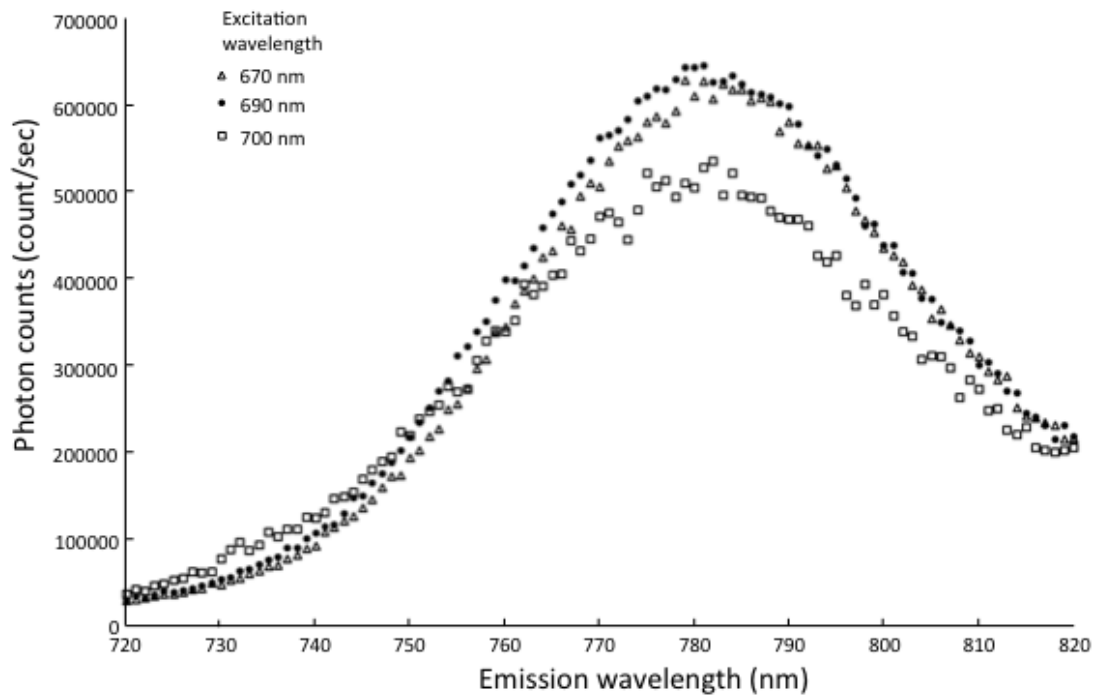


Figure 4-10. Emission spectra from solid PLGA film embedded with NIR dye for different excitation wavelengths

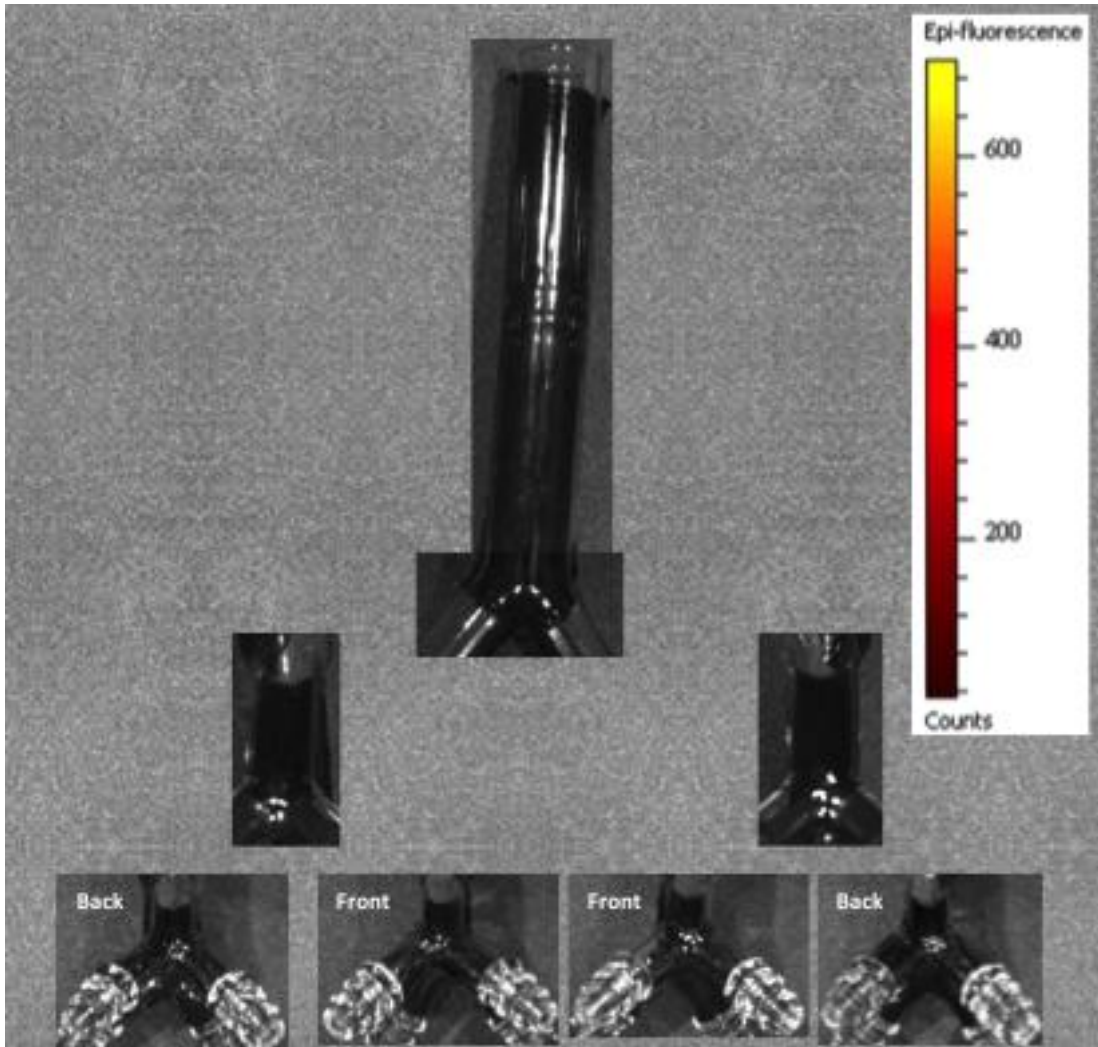


Figure 4-11. Compilation of IVIS Lumina images showing no photons in the airway model

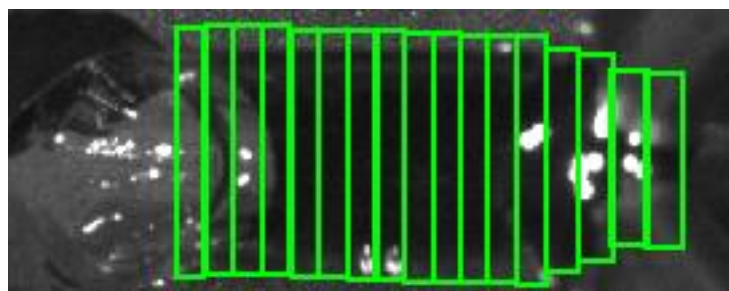


Figure 4-12. Example of individual regions of interest for generation 1 airway

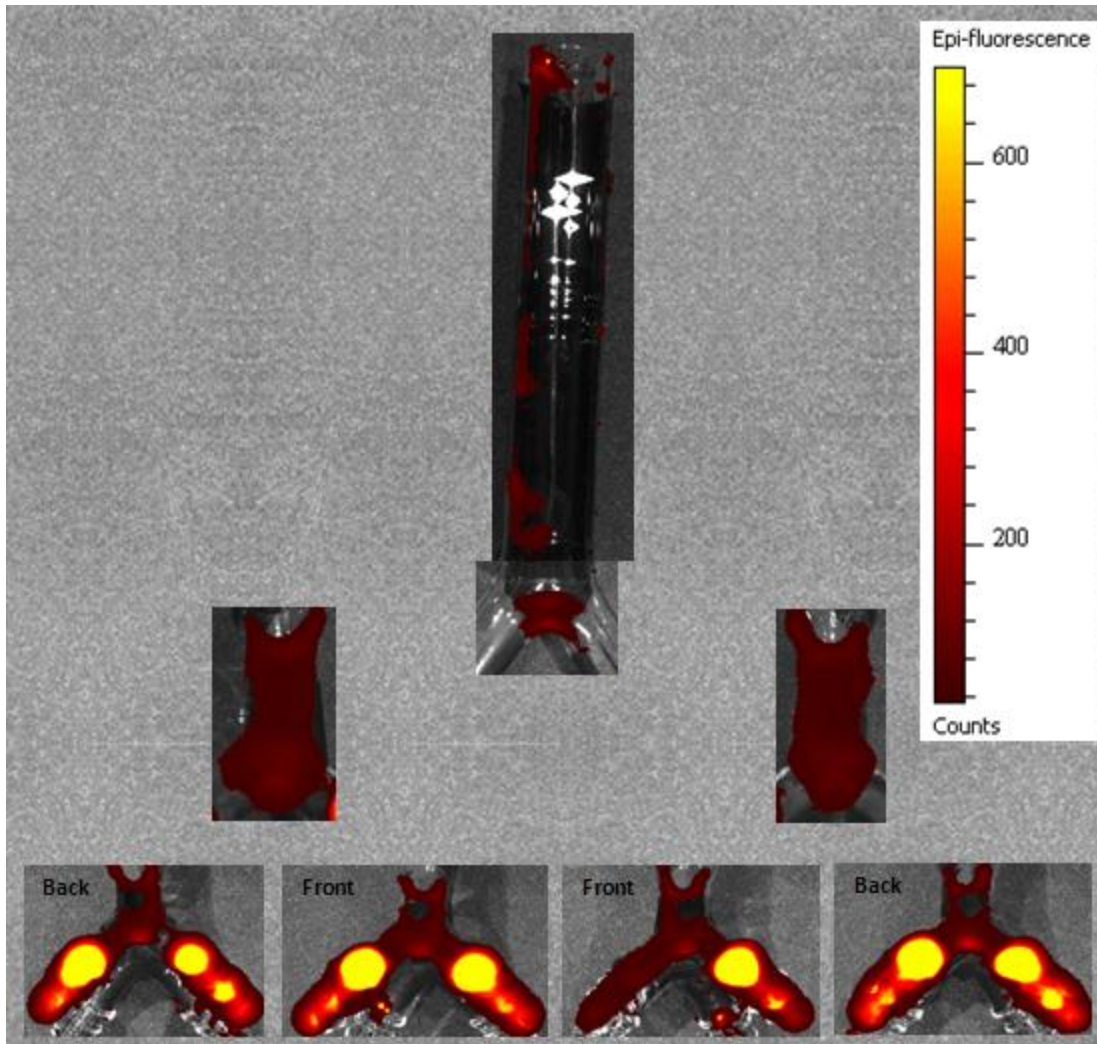


Figure 4-13. IVIS Lumina images of “neutral” sphere

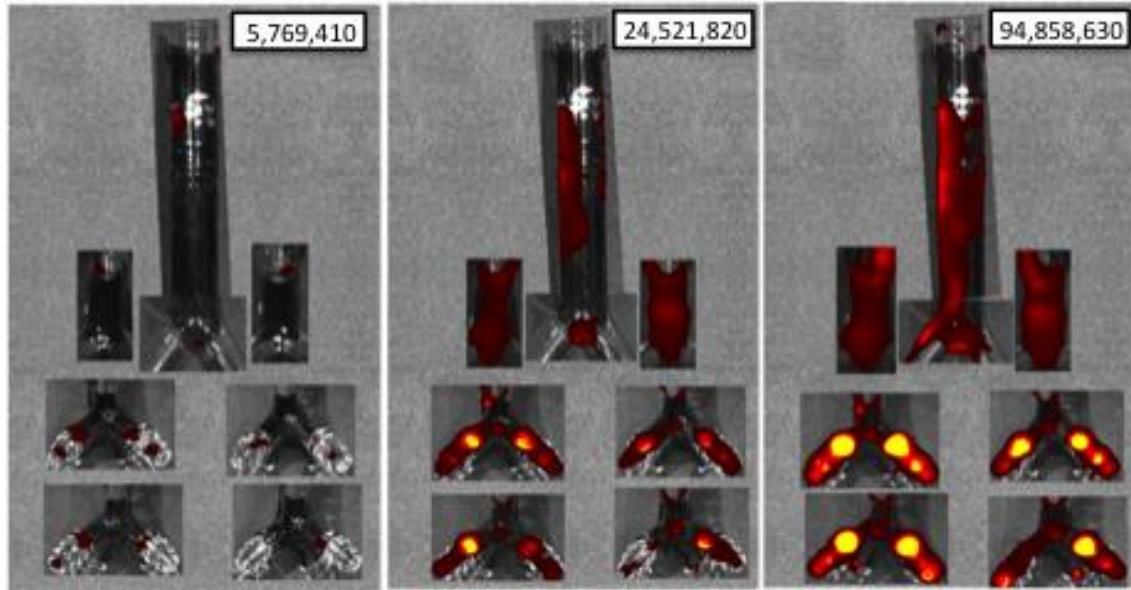


Figure 4-14. Evolution of deposition patterns for "neutral" sphere

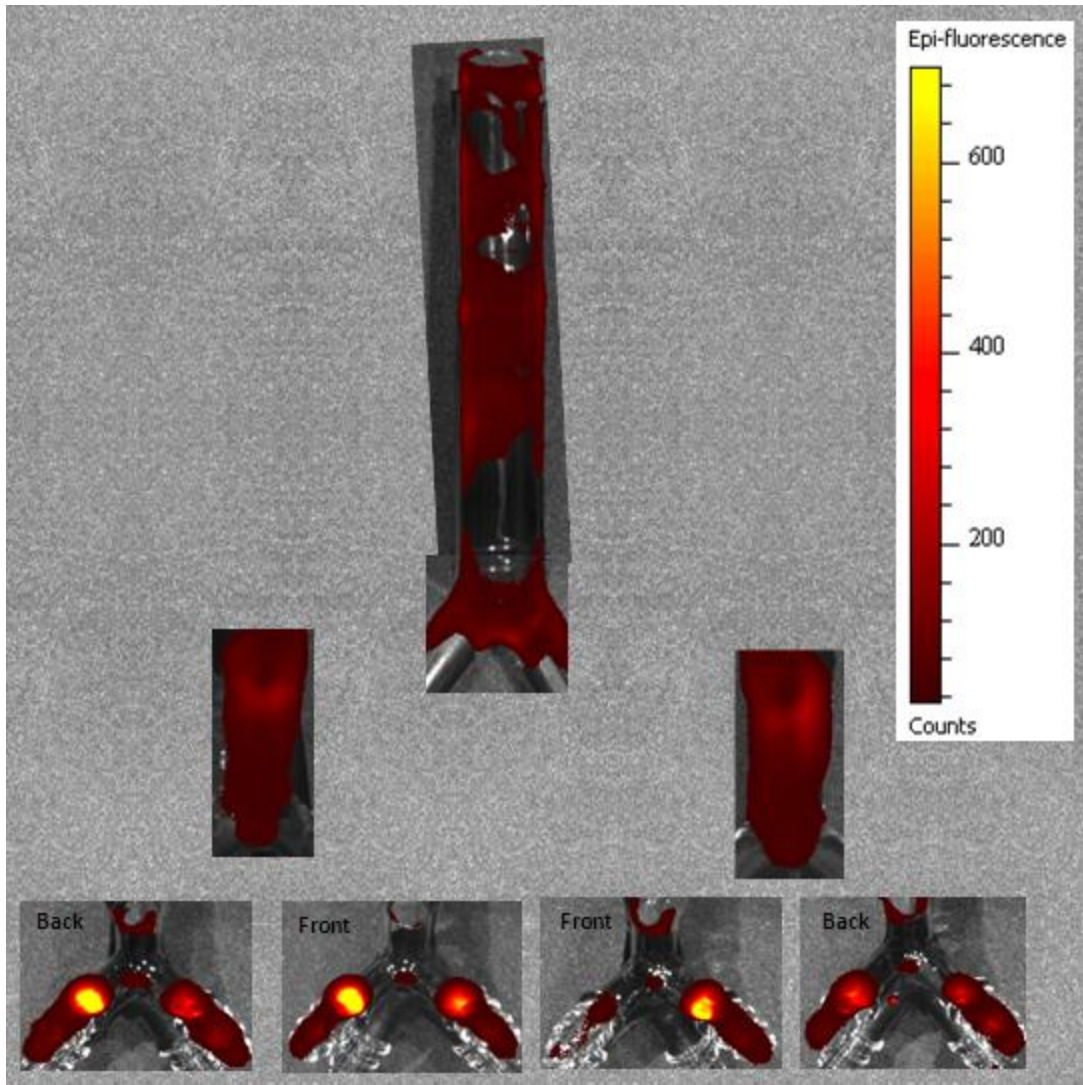


Figure 4-15. IVIS Lumina images of positively-charged sphere

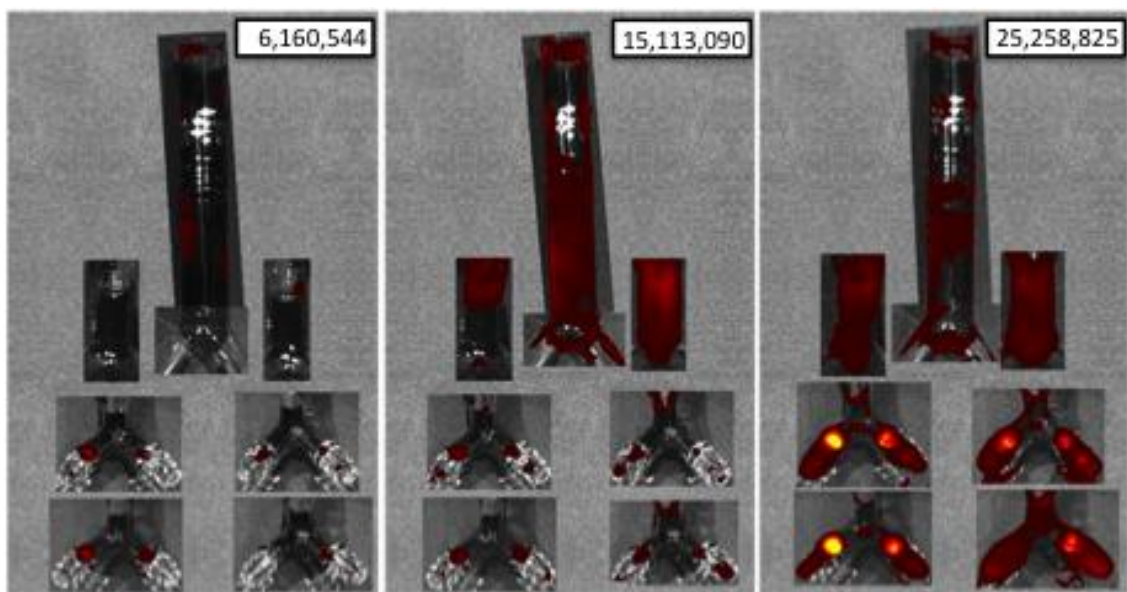


Figure 4-16. Evolution of deposition patterns for positively-charged sphere

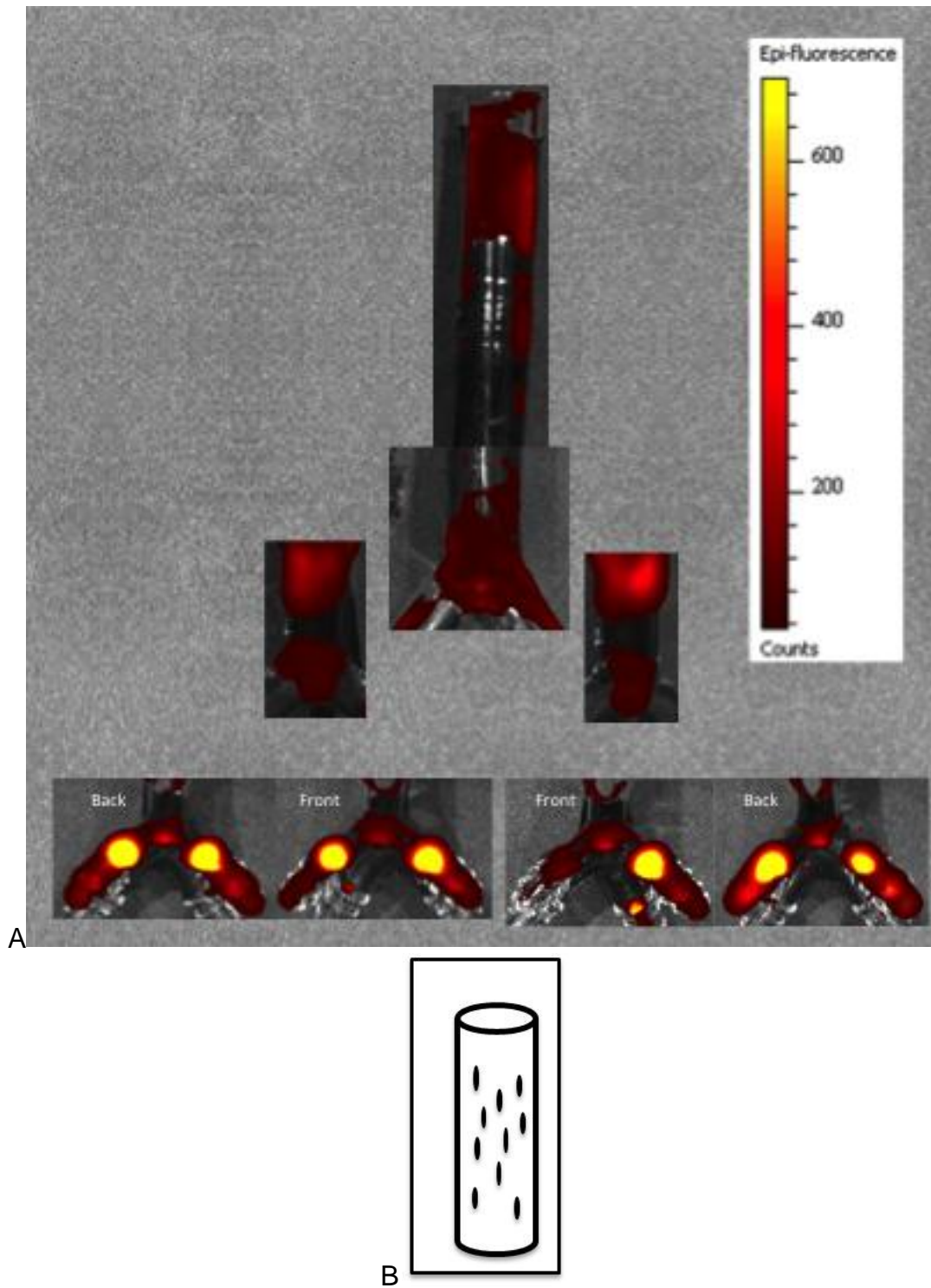


Figure 4-17. Deposition of rod-shaped particles. A) Compilation of IVIS Lumina images showing rod-shaped particle deposition patterns. B) Schematic of the observed deposition patches for the rod-shaped particles.

CHAPTER 5 DEPOSITION OF NON-SPHERICAL PARTICLES IN BIFURCATING AIRWAY

Background

The human respiratory system provides a vast area for quick and non-invasive drug delivery with minimal side effects (Marianecci et al. 2011). The large surface area of the lungs makes pulmonary medication an effective path for drug delivery. The first usage of pulmonary medication was in 1554 BC, for treatment of asthma (Sanders 2011). Since then drug delivery tools have been refined into the contemporary medical inhaler. Drugs and particulate matter are loaded into an inhaler, and then aerosolized into the lung. The devices and the drug formulations for pulmonary drug delivery are well developed; while relatively little effort went into engineering the particles. It is well accepted that particles between 1-10 μm in size have the highest deposition efficiency in the human lung. Many researchers studied the overall particle deposition using ideal monodisperse spherical particles (Pavia et al. 1977; Schlesinger et al. 1977; Emmett et al. 1982)

A small number of researchers studied the benefits of using controlled non-spherical particles for inhalation. They found that those fibers with certain aspect ratios and particles of certain shapes aerosolized from the dry powder inhaler much better than others (Kaialy et al. 2011). Once they enter the lung, particles with higher smoothness and aspect ratios can travel deeper into the airway (Zeng et al. 2000). Finally after deposition, alveolar macrophages interact with the particle differently depending on the particle morphology (Champion et al. 2007). The importance of particle morphology extends beyond the benefits of particle flow and deposition; drug release from particles is affected as well. Drug releases from microfilament polymers

were ten times longer than those from spherical particles (Geng et al. 2007). Zero-order drug release is possible using hemispherical particles (Hsieh et al. 1983)

The majority of the investigations of non-spherical particles were focused on the fibers. The investigations were a direct response to the danger posed by asbestos. Fibers are characterized using its aspect ratio, the ratio of the fiber's length to its diameter. The fiber orientation during flow depends on its aspect ratio. There are two possible flow extremes. Particles can align with the flow along the streamline. This orientation reduces the drag force on the particle. Particles can also align perpendicular to the streamline. This orientation increases the drag force on the particle and decreases the particle velocity. Fibers with an aspect ratio between 1 and 5 have no preferential flow orientation; while fibers, with aspect ratio greater than 5, align themselves along the streamline (Timbrell 1965).

With the exception of fiber, few particle shapes were investigated. Hu et al. (2008) generated micron size budesonide particles. The shapes under investigation were ellipsoidal, elliptic flake, and rectangular flake. Particles were sent into a throat airway, then into a multi-stage stage impinger. They found that flake particles outperform ellipsoidal particles with more flake particles depositing in the latter stages of the impinger. Hassan et al. (2009) studied sphere, pollen shaped, plate, cubic, and rod shaped particles. Pollen particles are spherical particles with non-uniform surface morphology, e.g. spiked surface. Particles were aerosolized using an inhaler and deposited into a cascade impactor at a flow rate of 30 LPM. They found that pollen shaped particles improved aerosolization from inhaler and deposition in the lung.

In addition to shape, particle density also plays an important role in particle deposition. Large porous particles had become a powerful medical delivery tool. Large porous particles allow for higher drug loading but they have the flow characteristic of smaller particles. Edwards et al. (1997) found that porous polymer particles, 8.5 μm in diameter, have a respirable fraction of 50% whereas solid particles with a diameter of 3.5 μm have a respirable fraction of 20%. Respirable fraction is related to how much particles remain in the lung after inhaled. They also found that the amount of porous particles deposited in rats' lungs is an order of magnitude higher than non-porous particles. In human clinical trial, the commercialized PulmoSphere particles (porous sphere) can double the deposition in the lung (Hirst et al. 2002). For non-spherical particles, Su et al. (2009) found that low momentum fibers penetrated deeper into the lung, whereas high momentum fibers deposited more in the upper airways.

The investigation in this chapter attempts to look at the effects of particle shape on the local particle deposition. Ten different types of particles with aerodynamic diameters between 3-10 μm were used in the experiment. The shapes used were sphere, rod, flake, and random shape. The local depositions were visualized and quantified using near-infrared (NIR) fluorescence. An empirical model was made relating the deposition efficiency in each airway.

Deposition Efficiency

Deposition efficiency (η) characterizes the particle deposition in the lung. Deposition efficiency is defined as the ratio of the mass of particles deposited in the airway (M_{dep}) to the mass of particles entered into the airway (M_{in}). Deposition

efficiency can be calculated for an individual airway (local deposition efficiency) or as a whole (total deposition efficiency). Deposition efficiency can be calculate using:

$$\eta_n = \frac{M_{dep,n}}{M_{in,n}} \quad (5-1)$$

where the subscript n denotes the airway of interest. Equation 5-1 is valid for individual airways or for series of airways.

Deposition Mechanisms

In any airway there are three main deposition mechanisms: inertial impaction, sedimentation, and diffusion (Hinds 1982). Inertial impaction occurs when a particle is unable to follow the fluid flow path. When the airflow changes direction, particles come into contact with the surrounding wall and deposit. Inertial impaction is classified using the Stokes number (*STK*). Stokes number is the ratio of the particle's stopping distance to the characteristic dimension of the obstacle. The Stokes number for particle flowing in a bifurcating airway is

$$STK = \frac{\rho_p d_p^2 v}{18\mu D} \quad (5-2)$$

where ρ_p is the particle density, d_p is the particle diameter, v is the average fluid velocity in the airway, μ is the fluid viscosity, and D is the airway diameter. Many researchers related particle deposition to the Stokes number. Gawronski and Szewczyk (1986) and Chan and Schreck (1980) both found a logarithmic relationship between Stokes number and the overall deposition efficiency in the tracheobronchial tree.

Sedimentation is the deposition due to the influence of gravity. The important forces in sedimentation are gravity, drag, and buoyancy. Using the force balance the terminal settling velocity (v_T) is calculated to be

$$v_T = \frac{d_p^2 (\rho_p - \rho_f) g}{18\mu} \quad (5-3)$$

where ρ_f is the fluid density, and g is the acceleration due to gravity. For flow in a pipe, the deposition due to sedimentation in the absence of other deposition mechanisms can be related to the sedimentation parameter (ϕ):

$$\phi = \left(\frac{3}{4Re} \right) \left(\frac{\rho_f v_T L}{\mu} \right) = \frac{3v_T L}{4VD} \quad (5-4)$$

where L is the length of airway.

The third mechanism, diffusion, occurs by random bombardment of air molecules on the particle. This mechanism is known to be important for smaller particles. The particle's diffusion coefficient (α) can be calculated using the Stokes-Einstein equation:

$$\alpha = \frac{kT}{3\pi\mu d_p} \quad (5-5)$$

where k is the Boltzmann constant, and T is the temperature. Similar to the sedimentation parameter, particle deposition caused by diffusion in a pipe flow can be related to the diffusion parameter (Δ):

$$\Delta = \frac{\alpha L}{vD^2} = \frac{\pi\alpha L}{4Q} \quad (5-6)$$

where Q is the air flow rate. In pipe flow, both diffusion and sedimentation parameters determine the particle wall loss (Davies 1973).

There are two other deposition mechanisms: interception and electrostatic. Interception is relevant for particles with large aspect ratios such as fiber. Interception occurs when the particle shape or particle size prevents the particle from passing through the airway. Electrostatic deposition is caused by the influence of electrostatic charges on the particle. The effects of both mechanisms are expected to be minimal in this study.

Particle Characterization

In this study, particles are characterized into three general shapes: sphere, rod, and flake. Important parameters are the particle surface area (S_p) and particle volume (V_p). A schematic of each particle shape is shown in Figure 5-1. Spherical particles (Figure 4-1A) are assumed to be perfectly spherical; thus the equations for surface area and volume of a sphere can be used

$$S_p = \pi d_p^2 \quad (5-7)$$

$$V_p = \frac{\pi}{3} d_p^3 \quad (5-8)$$

Rod particles (Figure 5-1B) are particles with a high aspect ratio (l/d_p), the equations for surface area and volume of the cylinder can be used

$$S_p = \frac{\pi}{2} d_p^2 + \pi d_p l \quad (5-9)$$

$$V_p = \frac{\pi}{4} d_p^2 l \quad (5-10)$$

Flake particles (Figure 5-1C) are characterized with the projected surface area (A), perimeter (P), and particle thickness (t). Flake particles do not have a fixed projected area; the projected area differs from one particle to another. The equations for surface area and volume are:

$$S_p = 2A + Pt \quad (5-11)$$

$$V_p = At \quad (5-12)$$

Lastly, there are particles that do not have a definable shape. Each particle in the sample is different from another. These particles possess morphologies that are a combination of rod, tetrahedron, block, and cube. These random shapes are

generalized to a flake particle in order to approximate the particle surface area and volume.

To account for the non-spherical factor of the particle sphericity is used. Sphericity (ψ) is a shape factor that measures how close the particle's shape is to a sphere. Sphericity is defined as the ratio of the surface area of a sphere with the same volume as the particle to the actual surface area of the particle:

$$\psi = \frac{(\delta\pi^2 V_p)^{1/3}}{S_p} \quad (5-13)$$

Sphericity values range between zero and one, with one being completely spherical.

Boundary Layer

A boundary layer is a layer of flow near the wall where the flow is dominated by the viscosity. Within the boundary layer, the drag force becomes important and the fluid velocity profile approaches its minimum, as the fluid gets closer to the wall. Particle diffusion becomes more significant within the boundary layer than outside the layer. The boundary layer in the pipe will be approximated as the Blasius boundary layer for a flat plate; the boundary layer thickness (δ) is given as given as

$$\delta = 5 \sqrt{\frac{\mu L}{\rho_f v}} \quad (5-14)$$

The boundary layer thickness is normalized by the length of the airway (δ/L).

Experiments

Particle Characterization

Ten different types of particles were used for this experiment: solid glass spheres (Mosci), hollow glass spheres (Dantec Dynamic), glass rods (Nippon Electronic Glass co.), two types of glass flakes (Glassflake Ltd.), talc flakes (Barretts Minerals inc.), silver

flakes (Inframat Advance Material LLC.), Aluminum oxide powders (AIRBRASIVE), crushed glass powders, and fine fractions of JSC-1A lunar simulants. Images of each particle type were taken under an optical microscope to determine particle shape and sizes.

The images taken from the optical microscope were processed using ImageJ software. Samples up to 2500 particles were used to obtain representative characteristics for each type of particle. The particle aerodynamic diameter (d_a) was determined using the TSI PSD 3603 Aerosizer (TSI). Particle densities were obtained using the Ultrapyc 1000 gas pycnometer (Quantachrome corp.).

Airway Model

The airway model used in the experiment is described in Chapter 4. For this set of experiment, rather than considering the airway branch section and bifurcating section, this experiment looked at the deposition in each airway generation (see Figure 5-2). The dimension of each generation and the surface airway in each generation are listed in Table 5-1.

Particle Deposition

Particles were dyed with 3,3'-Diethylthiatricarbocyanine iodide (Sigma Aldrich), from this point on the dye will be referred to as NIR dye. Each type of particle was mixed into a solution of ethanol and NIR dye. The ethanol solvent dried off, leaving the particles coated with the NIR dye. Particles were placed in an inverse cyclone seeder. A small amount of Larostat antistatic powder (BASF) was mixed in with the particles to minimize the electrostatic charge on the particles. Figure 5-3 shows the diagram of the inverse cyclone seeder and the experimental setup. In the cyclone seeder, air entered from the side and entrained particles from the particle bed at the bottom of the cyclone

seeder. Entrained particles exited the cyclone seeder from the top and flowed into the airway model. In all experiments, the air flow rates were kept constant at the rate of 30 LPM (0.0005 m³/s). The flow parameters (air flow rate, average fluid velocity, residence time (τ), Reynolds number, and boundary layer thickness) for each generation are listed in Table 5-2.

The average particle mass flow rate was determined at the point where the particle entered the airway model. A filter was placed where the airway model is in Figure 5-3. The mass of the particles collected is determined for a set period of time. The mass flow rate was different for each type of particle. During experiment, particles were sent into the airway model until enough particles were deposited such that strong signals were seen in the fluorescence image. Some particle types (e.g. JSC-1A) required longer time because weaker signals were emitted from the NIR dye. The deposited airway model was taken to the imaging device directly after deposition. A total of three experiments were performed for each type of particle.

Quantifying the Deposition

The same method as described in Chapter 4 was used to obtain images from the IVIS Lumina. After deposition, the airway model was placed into the IVIS Lumina and the photon counts were determined for each airway. Multiple images were taken at different angles to capture the entire geometry of the airway model. Sample powders of known mass were placed into the IVIS Lumina with each picture to standardize the images together. The particle photon counts (total photon count minus the background) from the each airway were used to determine the percentage of particle deposited in each section.

Particles deposited in the airway model were washed off using ethanol alcohol. The washed particles were dried and weighted to determine the mass of the deposited particles. The total mass of deposited particles was multiplied by the percentage of the particle photon counts in each airway to determine the mass of particles deposited in individual airways. The total mass of particles entered into the airway was determined using the average particle mass flow rate and the duration time of the deposition. The deposition efficiency in each airway was calculated using Equation 5-1.

Results

Particle Characteristics

A representative image for each type of particle taken from the optical microscope is in Figure 5-4. Particle shape was classified into sphere, rod, flake, and random shape. The projected area diameters (d_{pa}) were calculated from the images. The surface area and volume for each type of particle were calculated using Equation 5-7 through 5-12, the thickness for flake particles were given by the manufactures. The surface area and volume are used to calculate the sphericity. The projected area diameter, aerodynamic diameter, particle density, and sphericity for each type of particle are listed in Table 5-3. Particle aerodynamic diameter links particle flow characteristic to a sphere of a given density with the aerodynamic diameter; whereas the projected area diameter indicates the actual size of the particle seen through the microscope. Comparing the two diameters can give information on how the particle size and how particle flow; e.g. a glass sphere particle is about 3 μm in diameter but flow like an 8 μm sphere.

Particle Deposition

An image of the clean airway model taken with the IVIS Lumina is shown in Figure 4-11. In Figure 4-11 no photon signals were detected from the airway model. As a comparison, representative images for glass spheres and glass flakes 1 are shown in Figure 5-5 and 5-6 respectively. In each image, the higher color temperature indicates higher photon counts; red being the lowest and yellow being the highest. All three images are on the same color temperature scale. Figure 5-5 is the deposition of the glass sphere in the airway model. As expected, the majority of the depositions occur at the bifurcating section, with very little deposition in the straight tube section of the airway. This result is similar to the finding by Kim and Fischer (1999). Figure 5-6 shows the deposition of glass flake 1. The glass flake 1 deposited differently than the glass sphere. Instead of just depositing in the bifurcating section, glass flake 1 also deposited in the straight tube airway. Talc flakes also show deposition at the bifurcating section of the airway.

Particle photon counts were calculated from each image. The percent deposited in each generation of the airway was calculated and listed in Table 5-4. Table 5-4 also shows the average weight of the particles that entered and deposited in the airway model. Based on the values in Table 5-4, the deposition efficiencies were calculated using Equation 5-1. The aerodynamic diameters (Table 5-3) were used along with the flow information (Table 5-2) to calculate the parameters important to each deposition mechanism (Equation 5-2, 5-4, and 5-6). The deposition efficiency, Stokes number, sedimentation parameter, and diffusion parameter in each airway for each type of particle are listed in Table 5-5.

Deposition Model

Six different types of particles were chosen to create an empirical model for particle deposition. Glass spheres, hollow glass spheres, glass rods, glass flakes 1, silver flakes and aluminum oxide particles were used. The empirical model proposed in this chapter uses an adjusted deposition efficiency (η^*):

$$\eta_n^* = \frac{\eta_n}{\psi(S_n/S_0)} \quad (5-15)$$

where S_n is the surface area of the airway, and S_0 is the surface area for airway G0. η_n^* is the deposition efficiency in airway n . η_n^* is calculate by normalizing η_n with the particle sphericity and the ratio of the surface area of the airway to the surface area of the largest airway. Normalizing the deposition efficiencies with the surface area will allow comparison of the deposition efficiency from one airway generation to the next.

From all the IVIS Lumina results, every type of particle exhibits higher deposition at the bifurcating section of the airway. It can be concluded that inertial impaction is the main deposition mechanism for particles with aerodynamic diameter between 1-10 μm depositing in a bifurcating airway. Figure 5-7 is a plot of the adjusted deposition efficiency as a function of Stokes number. In Figure 5-7, there appear to be two distinct relationships: one for flakes and low-density particles, and the other for high-density particles. Fitting the adjusted deposition efficiency with the Stokes number gives:

$$\eta_{STK}^* = 208STK^{3.678} \quad (5-16)$$

η_{STK}^* is the adjusted deposition efficiency arising from the inertial impaction, this term is plotted with a dotted line in Figure 5-7. Inertial impaction alone was not enough to explain all the particle deposition. Two other mechanisms, sedimentation and diffusion, were included to resolve the additional deposition. Inertial impaction is the primary

deposition mechanism. Sedimentation and diffusion are the secondary deposition mechanisms. Modifications are made to the sedimentation and diffusion parameter, the adjusted parameters are:

$$\frac{1}{\phi^*} = \frac{C}{\phi} \quad (5-17)$$

$$\Delta^* = C\Delta \left(\frac{\delta}{L}\right) \quad (5-18)$$

where

$$C = \exp\left(\frac{3}{\psi \cdot SG}\right) \quad (5-19)$$

the term C is the adjustment for the influence of the shape and density. The calculations of each parameter were done using the aerodynamic diameter as the particle diameter, this assumes that the particles are spherical. Adjustment is needed to correct for the non-spherical aspect of the shape. Sphericity is used to adjust for the non-spherical nature of the particle. The lower the sphericity, the higher the surface area the particle has. Higher surface area led to higher drag that hindered the particle flow. Higher surface area also increases the contact area for diffusivity. A particle with low sphericity (e.g. flakes) will have a lower terminal velocity than a sphere and will also have a higher diffusivity. The specific gravity term is used to limit the effect of the sphericity. Some particles, such as silver flakes or aluminum oxide, have low sphericity but high density. These particles depositions appear similar to the deposition of the solid sphere, where very little deposited on the straight section of the airway. Based on this observation, the effect of sphericity is negated by the density of the particle. A specific gravity term is used, at higher density, the term C approaches 1; and at lower density the specific gravity enhances the effect of the diffusion. The adjusted diffusion term also includes

the dimensionless boundary layer term (δ/L). The diffusion mechanism is important in the boundary layer, thus this term is included in the calculation of the diffusion parameter.

Figures 5-8A and 5-8B show the plot of $(\eta^* - \eta_{n,STK}^*)$ versus ϕ^* and $(\eta^* - \eta_{n,STK}^*)$ versus Δ^* respectively. The trends in Figure 5-8A and 5-8B are similar to that in Figure 5-7, power law fitting was also used in for these two mechanisms; these result in:

$$\eta_{\phi}^* = 3.67 \times 10^{-12} \phi^{*3.6778} \quad (5-20)$$

$$\eta_{\Delta}^* = 9.43 \times 10^{33} \Delta^{*3.6778} \quad (5-21)$$

η_{ϕ}^* and η_{Δ}^* are plotted as dotted lines in figure 5-8A and 5-8B. This model will assume that the sedimentation and diffusion are competing mechanisms. The two secondary mechanisms are assumed to be mutually exclusive and only one will occur depending on the particle property. The specific momentum of the particle (P') is used to determine which secondary mechanism will take place.

$$P' = \rho v_t \chi^2 \quad (5-22)$$

where χ is a shape factor defined by

$$\chi = \sqrt{\frac{\pi d_a^2}{S}} = \frac{d_a}{d_s} \quad (5-23)$$

The shape factor χ , represents the ratio of aerodynamic diameter to the ratio of the surface area diameter. In general if the surface area diameter is less than the aerodynamic diameter then χ is greater than one, this means the actual particle has less surface area than the aerodynamic diameter. Lower surface area means less drag and a higher particle velocity. The opposite is true as well. The specific momentum is used to relate the effectiveness of Brownian diffusion. Particles with low P' felt greater

influence from the air molecules during collision; whereas high P' particles are unperturbed by the air molecules. The particles' specific momentum is used to classify whether sedimentation or diffusion will occur, the total deposition efficiency can be calculated using:

$$\eta_{Pre}^* = \begin{cases} \eta_{STK}^* + \eta_{\phi}^* & \text{for } P' \geq 10 \text{ kg/m}^2\text{s} \\ \eta_{STK}^* + \eta_{\Delta}^* & \text{for } P' < 10 \text{ kg/m}^2\text{s} \end{cases} \quad (5-24)$$

η_{Pre}^* is the predicted deposition efficiency predicted.

Model Validation

The model is checked with all ten types of particles used in the experiments. Table 5-6 lists the adjusted deposition efficiencies from each experiment (η_{Exp}^*) and the adjusted deposition efficiency calculated using Equation 5-24 (η_{Pre}^*). The plot in Figure 5-9 compares η_{Pre}^* with η_{Exp}^* . The dotted line in Figure 5-9 represents the $\eta_{Pre}^* = \eta_{Exp}^*$ relationship. The fitting match well for both the six particle types used to create the model, as well as the other four particle types. The RMS deviation between η_{Exp}^* and η_{Cal}^* is 0.24.

The airway used in these experiments is based on generation 0 to generation 3 of the Weibel's Model A. A more realistic airway or an airway with deeper generation would be useful for further experiments. Airways with deeper generation will lead to a more realistic result that is much closer to the deposition in the human pulmonary airway. However with a more complex airway, it will become harder to determine the local deposition efficiency. We would then need a more complex system to determine the deposition efficiency. The recommended system would be something akin to SPECT where the images are taken in slices and are put together to create a 3D model.

NIR fluorescence was proven to be successful, but unless a machine similar to the Xenogen IVIS is available to take 3D images, using commercially available imaging systems will be more efficient.

Summary

This chapter presented an empirical model relating the deposition efficiency particle characteristic. The deposition efficiency in a single airway was broken down in to the primary deposition mechanism, inertial impaction, and a secondary mechanism (either sedimentation or diffusion). The two secondary mechanisms are mutually exclusive and chosen by the specific momentum of the particle.

This model is expected to work for any non-spherical particles with 1-10 μm aerodynamic diameters, given that the representative morphology the particles can be categorized into a specific shape. This model may fail for the cases when particles travel deeper into the airway or when particle density is too low. The empirical model is expected to fail in these cases because sedimentation and diffusion will be the dominating deposition mechanisms instead of inertial impaction.

Table 5-1. Dimension of the bifurcating airway model

Airway	Number of Airway	D (m)	L (m)	S (m ²)
G0	1	0.0180	0.1200	0.006632
G1	2	0.0122	0.0476	0.001723
G2	4	0.0083	0.0190	0.000431
G3	8	0.0056	0.0076	0.000127

Table 5-2. Flow parameter in the bifurcating airway model for the average airflow rate of 30 LPM

Airway	Q (m ³ /s)	V (m/s)	τ (s)	Re	δ (m)
G0	0.0005	1.965	0.061	2358	0.00479
G1	0.00025	2.139	0.022	1739	0.00289
G2	0.000125	2.310	0.008	1278	0.00176

Table 5-3. Characterization for each type of particle

Particle	Particle shape	d_{pa} (μm)	d_a (μm)	ρ_p (kg/m ³)	ψ
Glass spheres	Sphere	2.892	8.470	2326.7	1
Hollow glass spheres	Sphere	5.715	8.360	1038.4	1
Glass rods	Rod	10.858	10.898	2610.1	0.762
Glass flakes 1	Flake	12.551	8.124	2491.6	0.393
Glass flakes 2	Random	8.694	10.810	2472.0	0.783
Crush glass	Random	5.368	7.989	2556.6	0.796
Talc flakes	Flake	5.624	3.419	2865.3	0.477
Silver flakes	Flake	8.070	6.096	9552.8	0.26
Aluminum oxide	Random	5.624	5.549	4580.2	0.411
JSC-1A, fine fraction	Random	3.257	6.522	3200	0.628

Table 5-4. The percentage of deposition in each generation of the airway model, and the particle weight deposited in the model

	Glass sphere	Hollow glass sphere	Glass rod	Glass flake 1	Glass flake 2
<i>G0</i> (%)	6.70 ± 2.11	10.13 ± 4.15	8.90 ± 1.15	29.90 ± 1.70	9.13 ± 1.71
<i>G1</i> (%)	21.99 ± 6.88	20.92 ± 2.64	28.38 ± 2.49	17.12 ± 1.15	30.09 ± 3.97
<i>G2</i> (%)	28.48 ± 4.00	29.64 ± 3.38	16.54 ± 1.34	16.78 ± 0.06	25.22 ± 2.91
Connector (%)	42.82 ± 6.55	39.31 ± 6.16	46.19 ± 4.30	36.20 ± 0.55	35.55 ± 2.56
Wt deposited (g)	0.01309 ± 0.00217	0.01351 ± 0.00500	0.00838 ± 0.00094	0.01137 ± 0.00229	0.01949 ± 0.01019
Wt entered (g)	0.18473 ± 0.04307	0.05833 ± 0.05465	0.02544 ± 0.00308	0.02637 ± 0.00776	0.09965 ± 0.03846

	Crush glass	Talc flake	silver flake	Aluminum Oxide	JSC-1A fine fraction
<i>G0</i> (%)	15.72 ± 1.86	12.88 ± 5.75	6.23 ± 1.49	1.16 ± 0.08	4.75 ± 0.85
<i>G1</i> (%)	24.47 ± 3.56	17.66 ± 5.23	21.70 ± 2.41	21.38 ± 1.90	16.31 ± 2.40
<i>G2</i> (%)	18.86 ± 2.72	26.97 ± 3.31	18.58 ± 2.20	19.19 ± 1.56	22.90 ± 1.07
Connector (%)	40.96 ± 3.92	42.28 ± 6.16	53.49 ± 5.72	58.27 ± 1.52	56.04 ± 2.65
Wt deposited (g)	0.01765 ± 0.00712	0.00277 ± 0.00141	0.0036 ± 0.00159	0.00328 ± 0.00131	0.03859 ± 0.00890
Wt entered (g)	0.05950 ± 0.00675	0.01620 ± 0.00329	0.01494 ± 0.00909	0.03473 ± 0.01818	0.15102 ± 0.05284

Table 5-5. Deposition parameter for each particle in each airway

	Airway	η (%)	STK	ϕ	$\Delta \times 10^{-10}$	
Glass spheres	G0		0.48	0.0562	0.0128	5.32
	G1		1.57	0.0903	0.0069	4.22
	G2		2.06	0.1434	0.0038	3.37
Hollow glass spheres	G0		2.35	0.0245	0.0056	5.39
	G1		4.96	0.0393	0.0030	4.28
	G2		7.40	0.0623	0.0016	3.42
Glass rods	G0		1.72	0.1044	0.0239	4.14
	G1		5.66	0.1677	0.0128	3.28
	G2		5.45	0.2663	0.0070	2.62
Glass flakes 1	G0		2.93	0.0554	0.0127	5.55
	G1		9.62	0.0890	0.0068	4.40
	G2		6.21	0.1413	0.0037	3.52
Glass flakes 2	G0		12.89	0.0973	0.0222	4.17
	G1		8.48	0.1563	0.0120	3.31
	G2		9.07	0.2482	0.0065	2.64
Crush glass	G0		0.11	0.0550	0.0126	5.65
	G1		2.02	0.0883	0.0068	4.48
	G2		1.85	0.1402	0.0037	3.58
Talc flakes	G0		4.66	0.0113	0.0026	1.32
	G1		7.61	0.0181	0.0014	1.05
	G2		6.35	0.0288	0.0008	8.35
Silver flakes	G0		1.50	0.1196	0.0273	7.40
	G1		5.30	0.1921	0.0147	5.87
	G2		4.79	0.3050	0.0080	4.69
Aluminum oxide	G0		2.20	0.0475	0.0109	8.13
	G1		3.08	0.0763	0.0058	6.45
	G2		4.86	0.1212	0.0032	5.15
JSC-1A, fine fraction	G0		1.21	0.0459	0.0105	6.92
	G1		4.22	0.0736	0.0056	5.49
	G2		6.19	0.1169	0.0031	4.38

Table 5-6. Contribution of deposition from each mechanism

	Airway	η_{STK}^* (%)	η_{ϕ}^* (%)	η_{Δ}^* (%)	η_{Pre}^* (%)	η_{Exp}^* (%)
Glass spheres	G0	0.53	0.38		0.91	0.48
	G1	3.00	3.72		6.72	6.02
	G2	16.44	35.12		51.56	31.73
Hollow glass spheres	G0	0.02		22.74	22.77	2.35
	G1	0.14		45.48	45.62	19.10
	G2	0.77		93.29	94.06	113.96
Glass rods	G0	5.12	0.09		5.21	2.26
	G1	29.26	0.86		30.11	28.62
	G2	160.24	8.09		168.33	110.22
Glass flakes 1	G0	0.50		48.17	49.21	7.46
	G1	2.84		97.41	100.25	94.35
	G2	15.57		199.81	215.38	243.67
Glass flakes 2	G0	3.95	0.13		4.08	16.46
	G1	22.57	1.29		23.86	41.66
	G2	123.61	12.18		135.79	178.49
Crush glass	G0	0.48	0.82		1.30	0.14
	G1	2.76	8.00		10.76	9.79
	G2	15.13	75.51		90.64	35.88
Talc flakes	G0	0.00		47.14	47.14	9.77
	G1	0.01		94.28	94.29	61.36
	G2	0.04		193.39	193.44	204.87
Silver flakes	G0	8.44	0.02		8.45	5.77
	G1	48.16	0.17		48.34	78.59
	G2	263.80	1.63		265.43	284.33
Aluminum oxide	G0	0.28	2.17		2.45	5.36
	G1	1.62	21.26		22.88	28.90
	G2	8.85	200.72		209.56	182.29
JSC-1A, fine fraction	G0	0.25	1.70		1.95	1.93
	G1	1.42	16.64		18.05	25.85
	G2	7.77	157.05		164.82	151.71

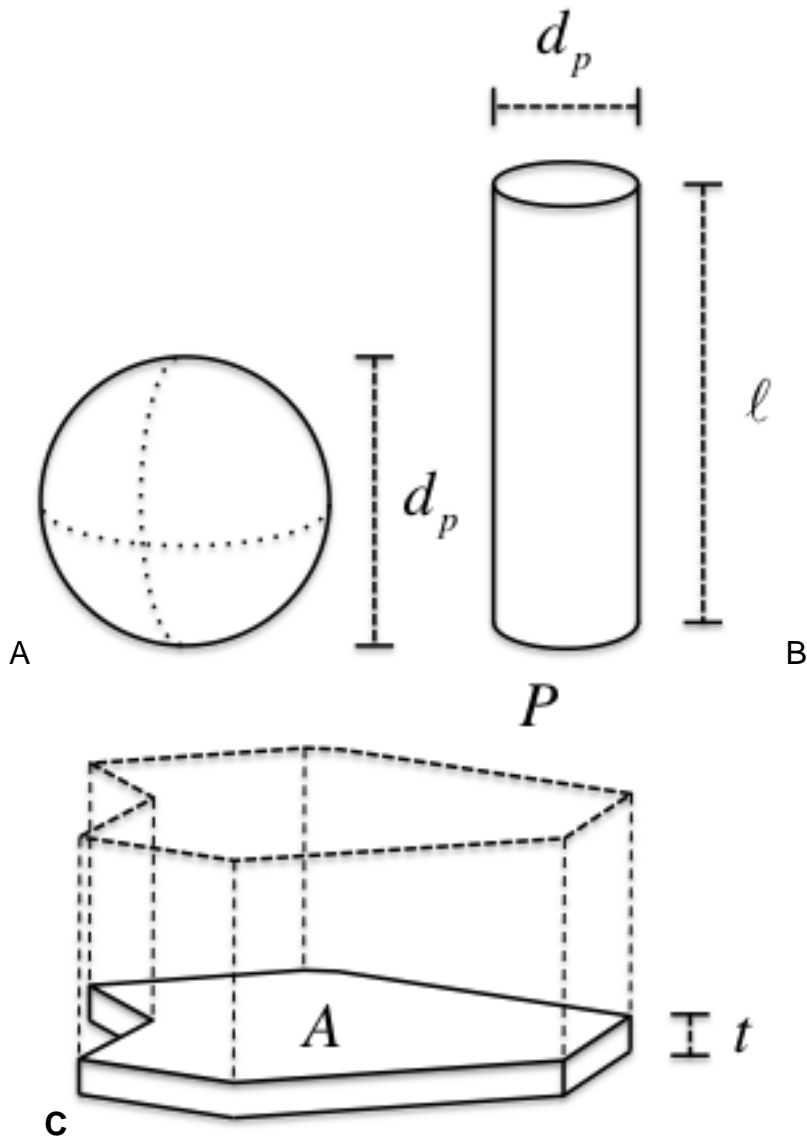


Figure 5-1. Shape and characteristic dimensions of different types of particles. A) Sphere. B) Rod. C) Flake particle.

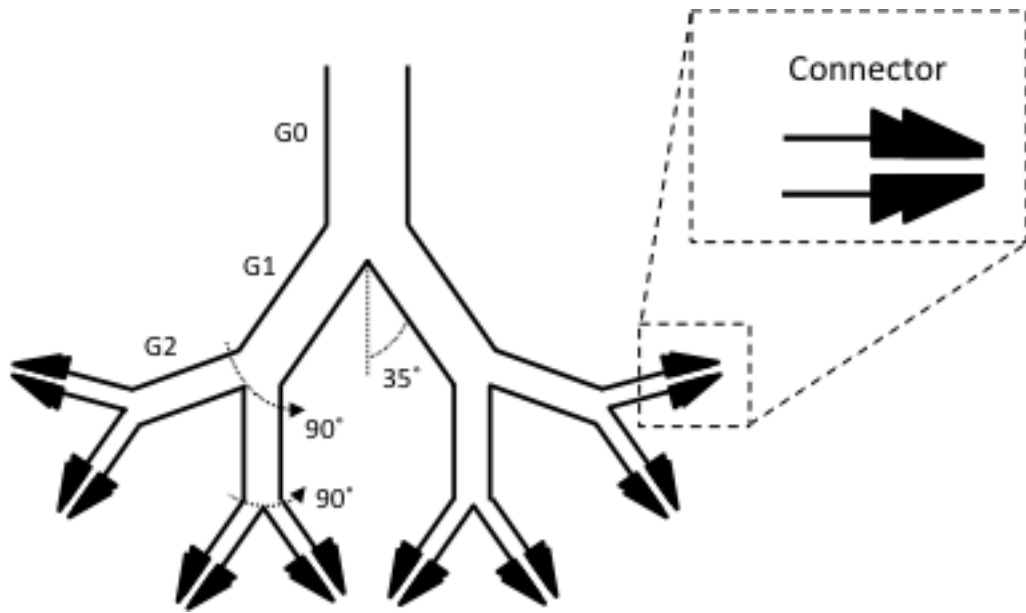


Figure 5-2. Schematic of the bifurcating airway model

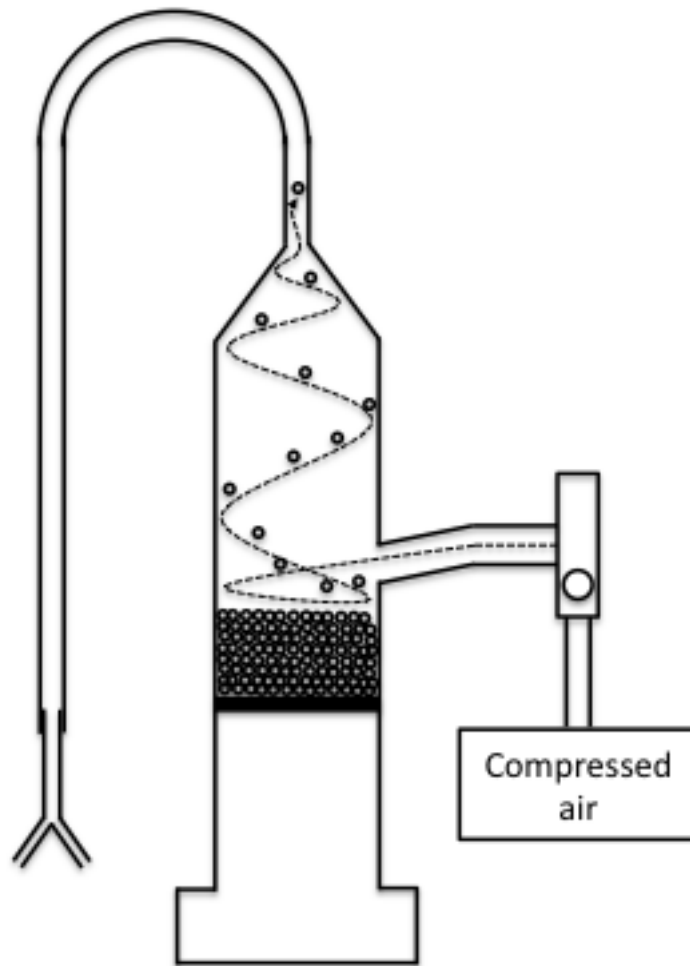


Figure 5-3. Schematic of the inverse cyclone seeder setup

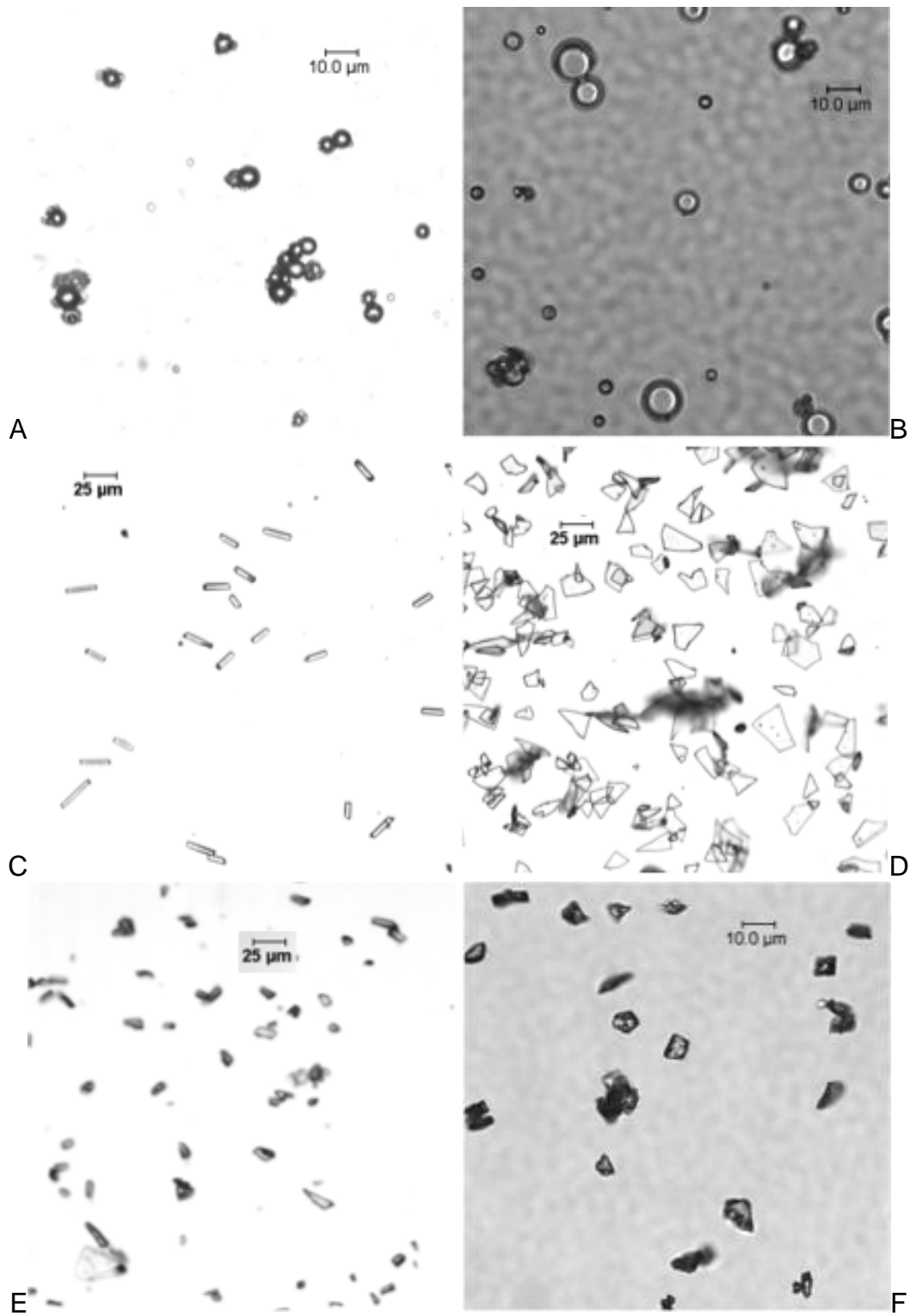


Figure 5-4. Particle viewed under optical microscope. A) Glass spheres. B) Hollow glass spheres. C) Glass rods. D) Glass flakes 1. E) Glass flakes 2. F) Crushed glass. G) Talc flakes. H) Silver flakes. I) Aluminum oxide. J) Fine JSC-1A

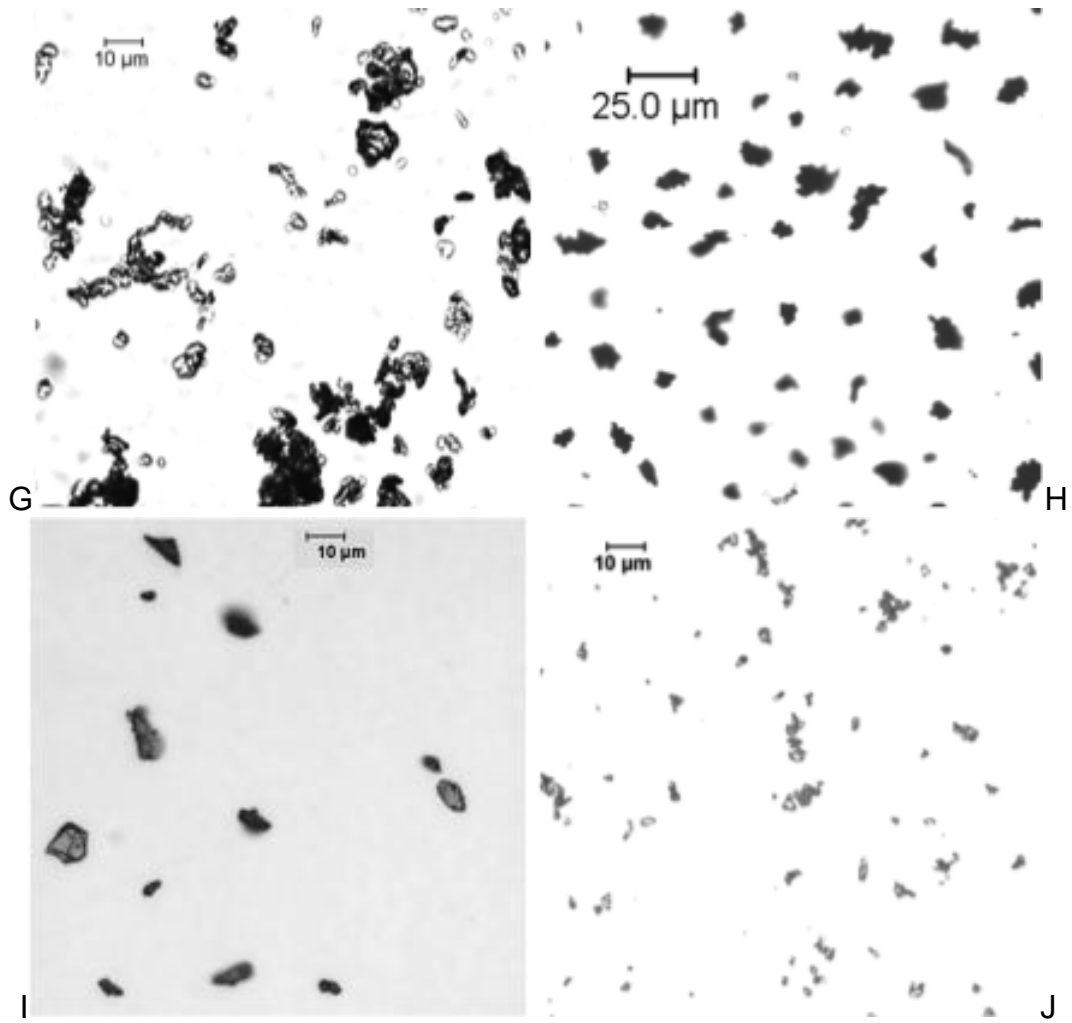


Figure 5-4. Continued

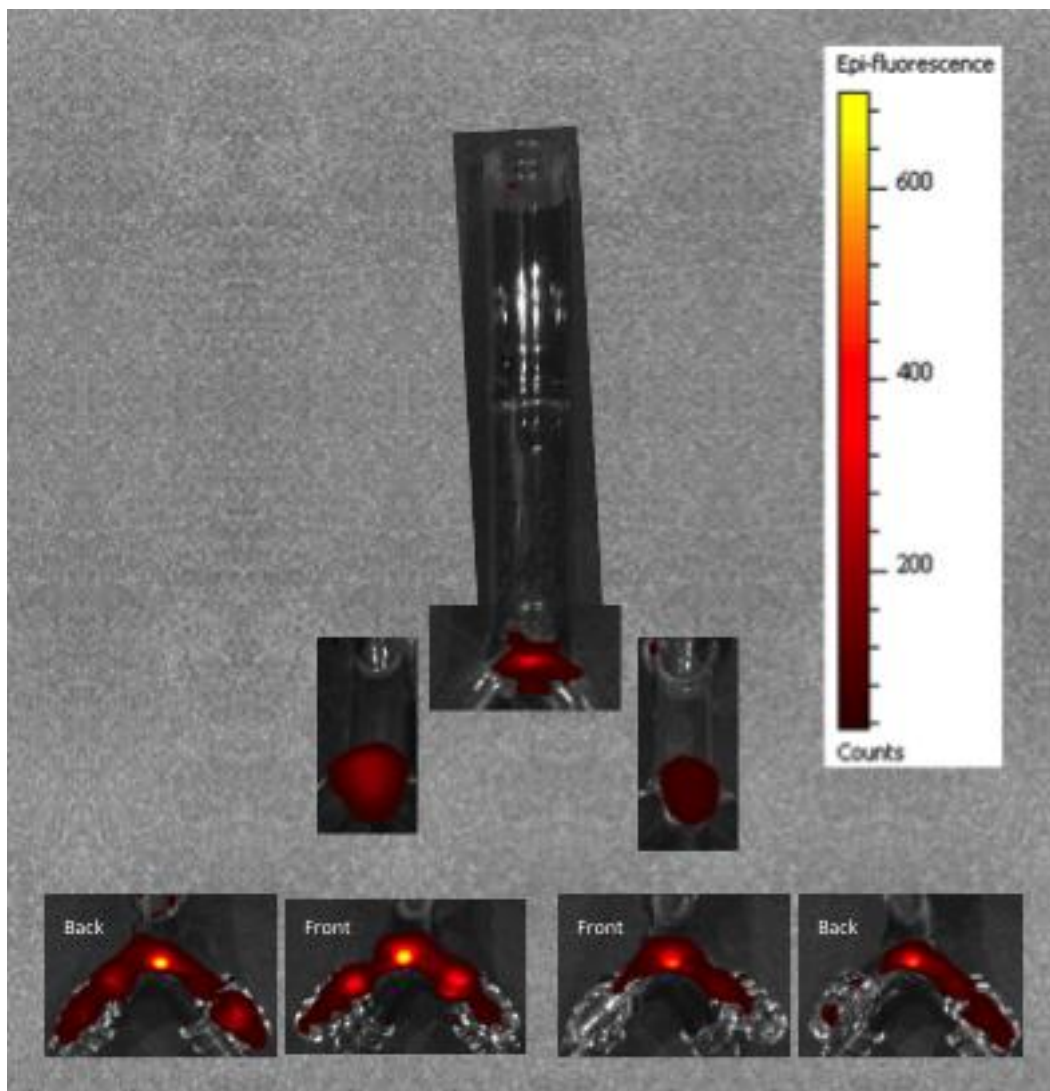


Figure 5-5. IVIS Lumina images of glass spheres

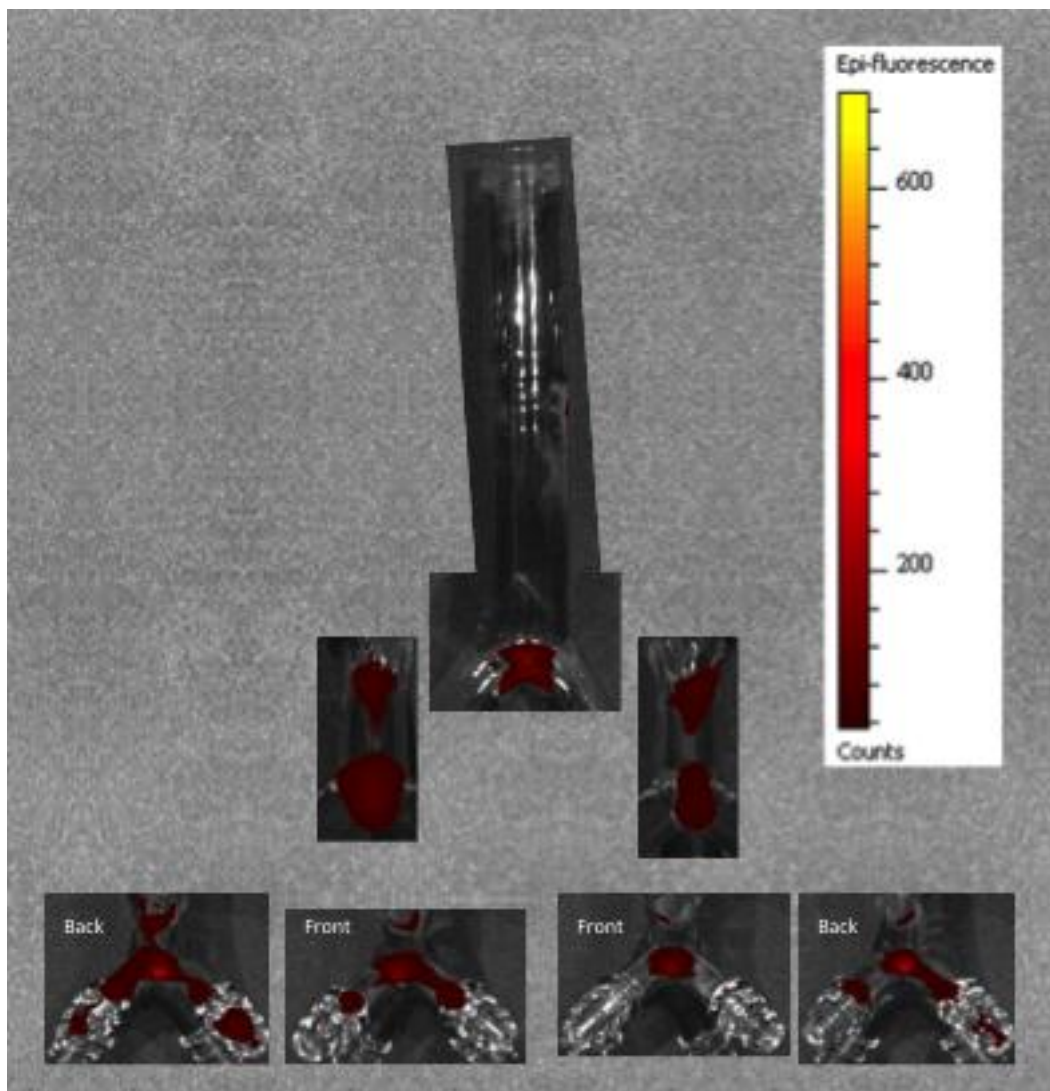


Figure 5-6. IVIS Lumina images of glass flakes 1

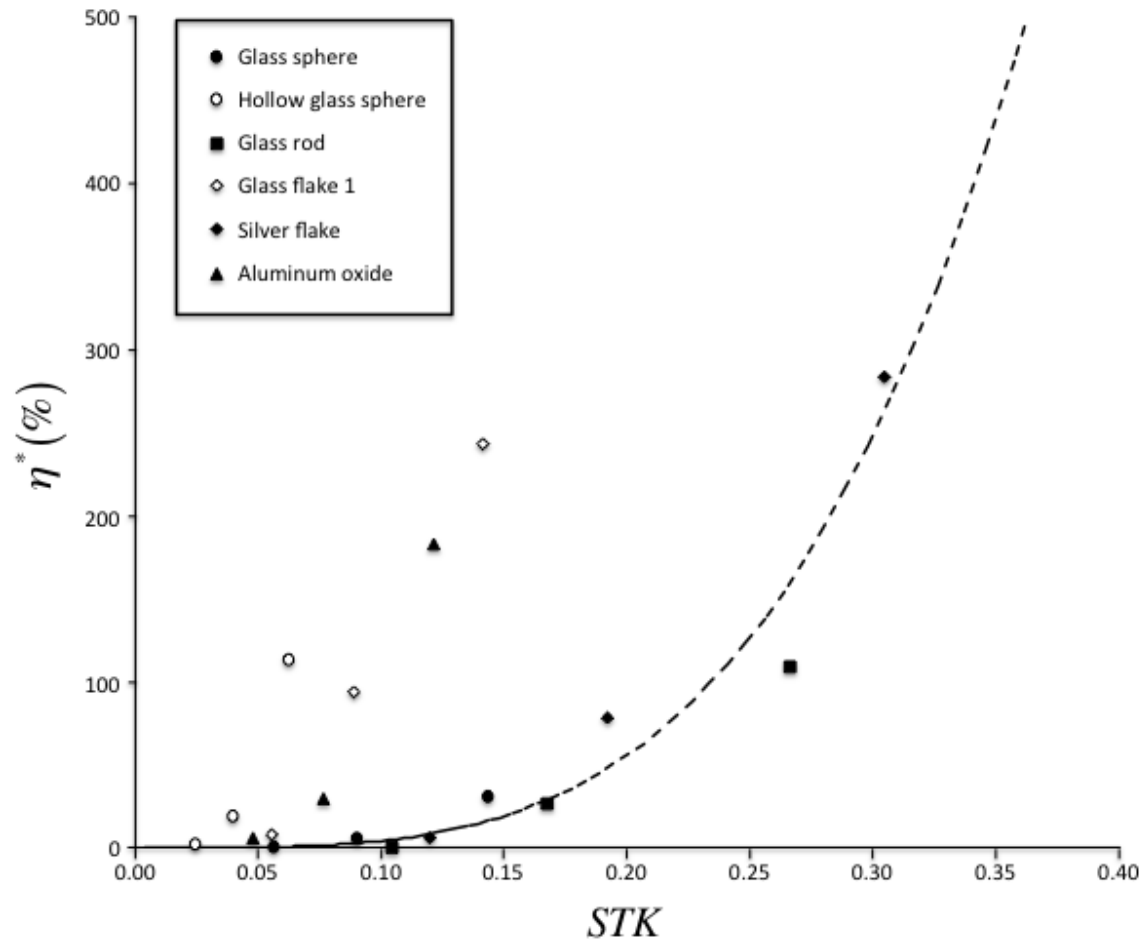
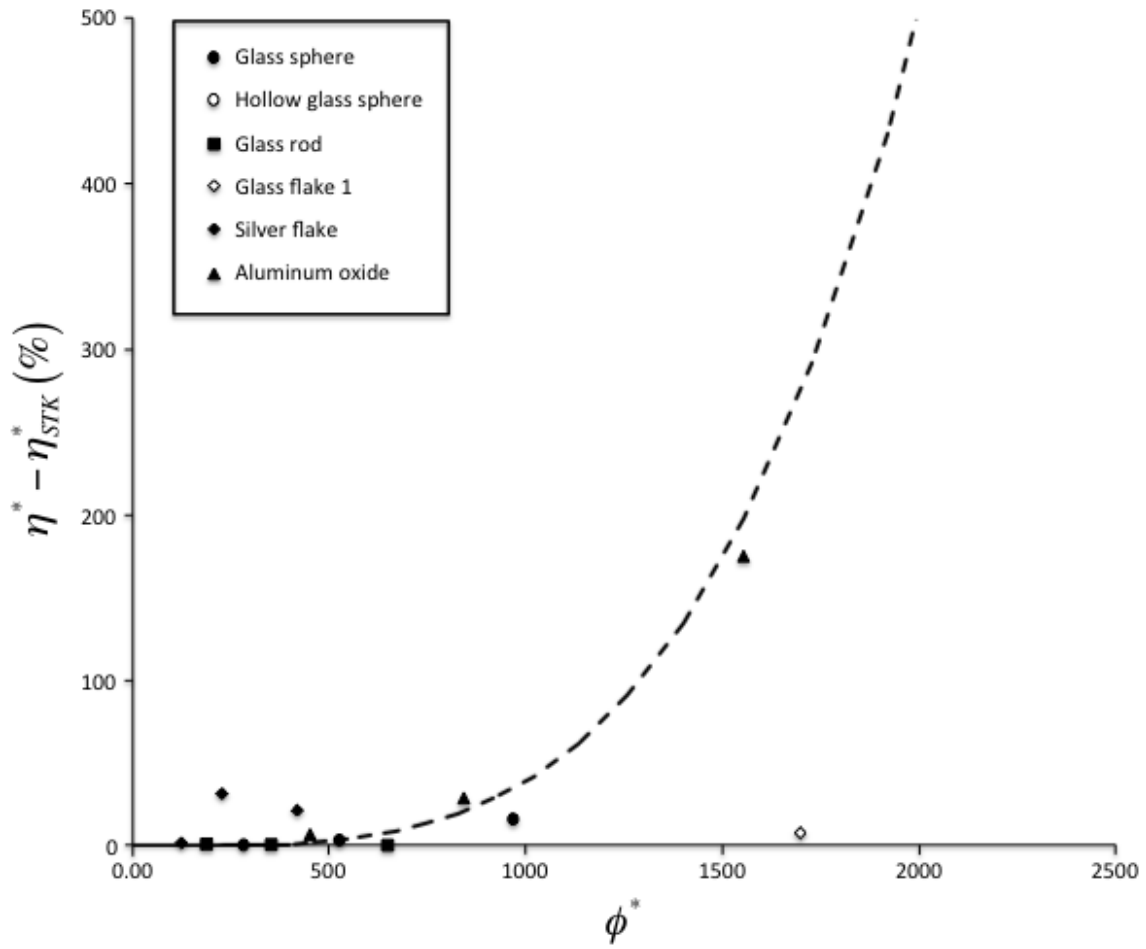


Figure 5-7. Plot of the η^* against Stokes number. The dotted line indicates the relation for the adjusted deposition efficiency of the inertial impaction mechanism



A

Figure 5-8. Deposition efficiency of the secondary mechanism. A) Sedimentation, B) Diffusion. The dotted line indicates the calculated relationship for the mechanism.

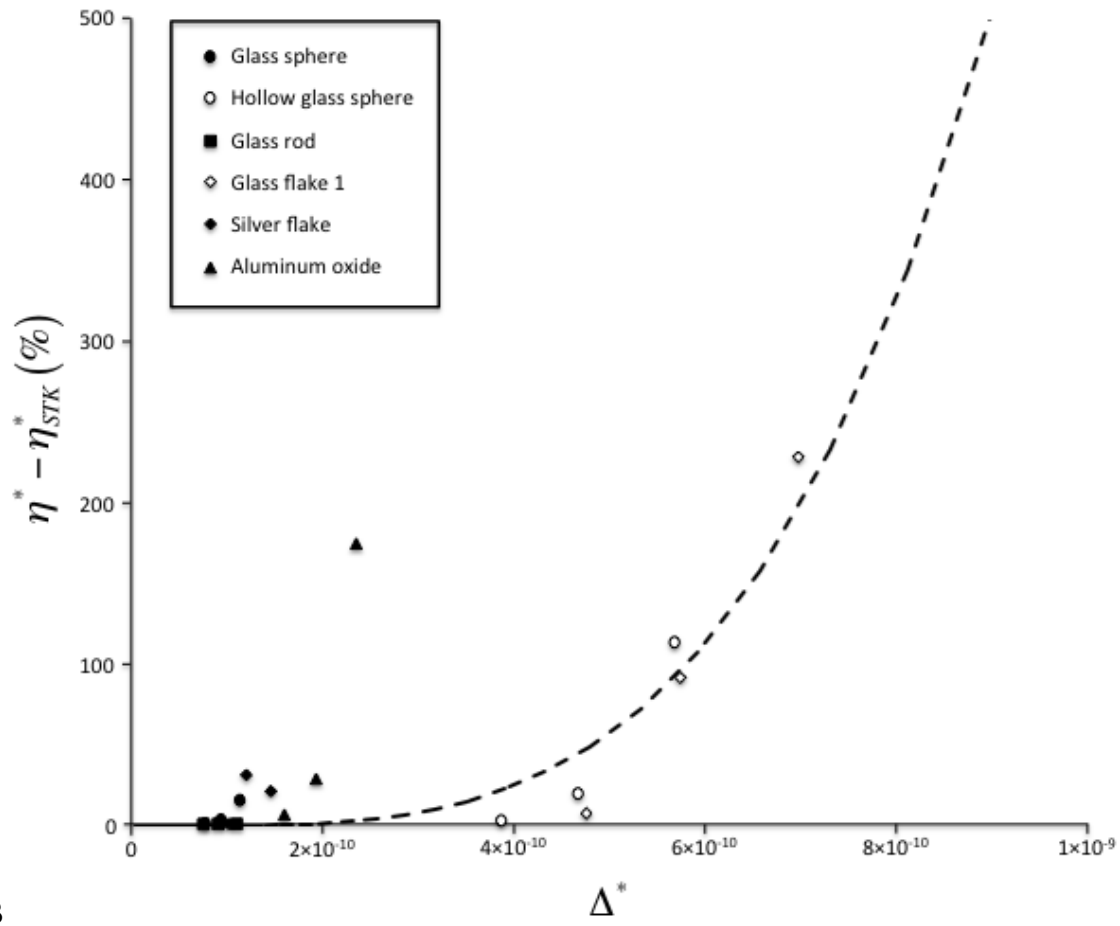


Figure 5-8. Continued

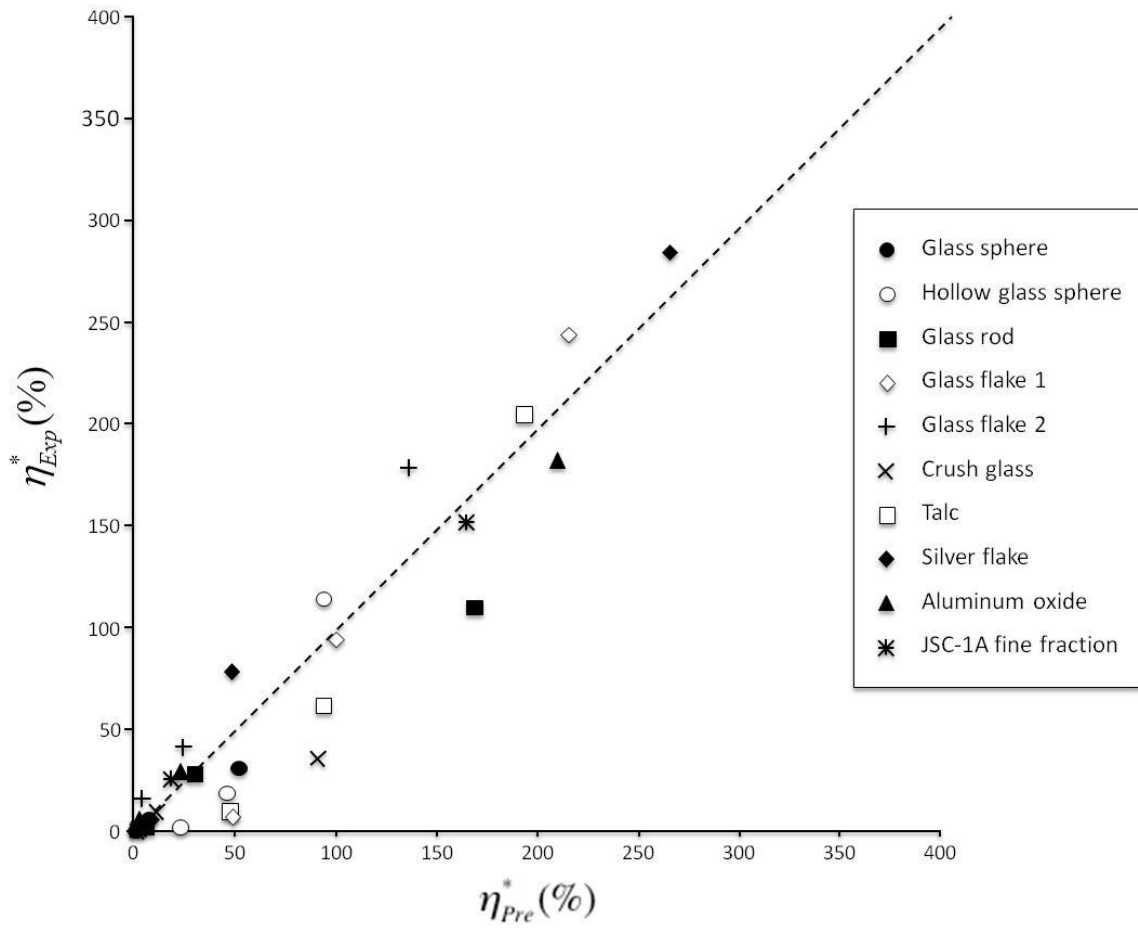


Figure 5-9. η_{pre}^* vs. η_{Exp}^* . The dotted line is the $\eta_{pre}^* = \eta_{Exp}^*$ relationship.

CHAPTER 6 CONCLUSION AND RECOMMENDATION

The works presented deal greatly with the transport of particles in the airways.

Particles become charged and deposit along the flow geometry. The important contributions are:

- Developed a standardized method for measuring particle-wall charging characteristics (L_0 , n_0 , and q_∞).
- Demonstrated the prediction of particle charge for a pipe flow system using experiment coupling with CFD simulations.
- Validated the use of NIR fluorescence in the visualization and quantification of particle deposition
- Showed that particle deposition is dependent not only on how much charge is on the particles but also on the distribution of charge
- Acquired data for the local deposition of non-spherical particles in a series of branching airways.

Particle Charging During Transport

The works detailed in Chapters 2 and 3 demonstrated that it was possible to predict the particle charge in various conditions based on information obtained from a small-scale experiment. An experiment was performed to determine what happened to the particle charge after traveling through a single 1 m pipe. Then a CFD simulation was performed, matching the experimental condition, to determine the particle-wall collision. With this set of information it is possible to predict particle charge in the same particle-pipe system at different operating conditions. This method is valid for both spherical and non-spherical particles. There are many ways to improve this model. The future continuation of this work should focus on expanding the model as mentioned in detail in Chapter 3. In the future, the model should take into account:

- Changes in particle size

- Changes in pipe
- Changes in environmental condition (humidity and temperature)
- Complex flow geometry

Lastly, the characteristic parameters as well as the equilibrium charge should be related to the particle and wall material parameters. This would be difficult because the charge transfer theory of insulators is not well developed. But if these parameters could be calculated from material properties, an experiment would no longer be needed. Particle charge could be determined directly using simulation and all these effects could be incorporated into a commercial CFD code to determine particle charge in any particulate system.

Particle Deposition in Pulmonary Airways

Use of NIR Fluorescence

The works described in Chapters 4 and 5 demonstrated that it is possible to both visualize and quantify particle deposition in a complex airway geometry using near-infrared fluorescence. The NIR images looked clear and the photon count in the images was used to determine the mass of the particle deposited in the airway model. The only issue we encountered was the long deposition time needed in order to get a strong signal coming from the particle. However the lack of signal was attributed to the poor matching of the dye and the camera filter set. In future studies, it is very important to better coordinate the dye and the filter set.

Ultimately, the use of NIR fluorescence is aimed toward in-vivo clinical trials. The next step in testing this is to perform experiments with animals. Similar experiments with charged particles and non-spherical particles should be performed in rats. By performing the experiment with animals, it will be possible to determine the feasibility of particle imaging using NIR fluorescence. During this test it would be good to do a

comparative study with other common imaging techniques such as the gamma camera. The comparison will tell how the NIR fluorescence stacks up against other techniques currently used.

Effect of Electrostatic charge on Particle Deposition

Deposition of Charged Spheres

The deposition of charged particles shows that electrostatic charge on the particles strongly influences particle deposition. Charged particles deposited much more than uncharged particles. Uncharged spheres, found in prior studies and Chapter 5, are found to deposit mainly in the area where the airway branching occurs; whereas charged particles deposited everywhere. The deposition of charged spheres also depends upon the charge on the spheres. For particle clouds of positively-charged particles, deposition occurs sequentially in each airway particles pass through. This is hypothesized to be caused by particle-particle repulsion. Particles with zero net charge are found to deposit in each airway evenly over time.

Deposition of Charged, Rod-Shaped Particles

Rod-shaped particles were generated using an electrospray. The depositions of rod-shaped particles were similar to those of spherical particles because the aspect ratios of the rod-shaped particles were fairly low. Rod-shaped particles deposited in patches; this is thought to be caused by the deposited rods extending from the wall surface and becoming seed particles for additional particles to deposit.

Deposition of Charged Hollow, Balloon-Shaped Particles

The hollow, balloon-shaped particles were generated using an electrospray. This newly introduced technique using carbonated solution was successful in producing hollow particles. Particles that were predicted to be 1 μm penetrated through the airway

model without depositing. In the future we recommend that we document the rate of particle growth over time. The same technique for collecting particles at different distances from the generation would best document the effect because cameras do not have the magnification to capture the particle size.

Future Experiments

In the future, more experiments should focus on:

- A comprehensive study using different levels of charge on the particles
- Varying the aspect ratio of rod-shaped particles with electrostatic charge
- Varying the charge distribution on the particle surface
- Sending hollow, balloon-shaped particles into smaller airways
- Deposition with other types of non-spherical particles

These experiments will help us gain a better understanding of the influence of electrostatic charge on particle deposition.

Deposition of Non-Spherical Particles

Particles between 1-10 μm in size were successfully deposited and quantified using NIR fluorescence. The result showed that particle depositions can be explained using a combination of two mechanisms. Particle deposition depends on the particle specific momentum. Particles with high momentum deposited through particle impacting on the branching section of the airway; particle movement was also caused by gravity. Particles with low momentum also deposit by impacting at the branching section of the airway but instead of additional deposition caused by gravity, the low momentum particles deposit through Brownian movement toward the wall surface. Particle shapes were also important; the shape factors used to describe particle shapes were important in determining the particle deposition.

The empirical model presented in Chapter 5 is developed from six different types of particles and tested with ten different particle types. Additional work is needed to further test and improve the model; these additional tests include:

- Experiments with monodispersed particles
- Experiments using rods with varying aspect ratio
- Experiments using flakes of varying surface area
- Experiments with additional particle types
- Experiments with smaller airways

Another possible experiment is to deepen our understanding of particle morphology. Parameters such as particle roughness will surely affect particle flow and deposition. Suggestions for this would be to start with spherical particles and rod shaped particles with surface roughness. Roughness has been found to affect particle flow leaving the inhaler; it should also affect deposition as well.

Future applications to simulation

The overall goal of investigating particle shape and charge is to relate particle deposition to computational simulation. Due to the various particle-particle interactions seen in this work, we recommend the use of CFD-DEM simulation. In the CFD-DEM we should be able to determine the steady state fluid flow information for the airway model so that we can then simulate the particle-particle interaction in the flow system. Electrostatically charged particles will involve implementing interactions caused by electrostatic charge. This should include both particle-particle interaction as well as particle-wall interaction. The resultant force on the particle will be a function of charge of the two materials as well as the distance between them. Non-spherical particles should also be examined to determine the effect of particle shape. And lastly for simulations of non-spherical, charged particles, we expect that the distribution of electrostatic charge

on these particles will depend on the particle shape (such as charge accumulating toward the edges); this information should be taken into account for large particles. CFD-DEM simulation will help to identify the flow effect of the electrostatic charge on the particle and the effect of non-sphericity of the particle.

APPENDIX A EFFECT OF V_{EX} ON THE CONTACT POTENTIAL

The external electric field has a significant influence on contact electrification. The term V_{ex} in Equation 2-3 arises from the electric fields in the surrounding environment, including electric fields in nature (e.g. the earth magnetic field) and man-made electric fields (e.g. electric field from power line). A schematic of the electric potential of a particle in contact with a surface (Figure A.1) can help understand the effect of V_{ex} . In Figure A.1, the energy levels of the particle and wall are presented on the left and right hand sides, respectively. The Fermi level is a hypothetical energy level for an electron inside the particle. The vacuum level is the energy level such that the potential energy of the electron is zero. The difference between the Fermi level and the vacuum level is equal to the work function of the particle. Consider Case 1 in Figure A.1 where no external electric field is applied and the particle's work function (ϕ_a) is higher than the wall's (ϕ_b), while the potential difference due to image charge (V_e) and space charge (V_b) remain constant. The final voltage potential of the particle is determined by the work function and the final potential of the wall consists of the wall work function and the contribution from the image charge and the space charge. The charge transfer is equal to the potential difference of the two surfaces, V . During contact, electrons will transfer from lower voltage potential to higher voltage potential, as the potential is zero at the vacuum level. In Case 1, electrons will flow from the wall to the particle, resulting in negatively charged particles. Cases 2, 3, and 4 show what occurs when the external potential is applied to the wall surface. In Case 2, a small amount of potential is applied to the wall; the final potential of the wall is now closer to the potential of the particle. The result of such a contact is that smaller charge transfer occurs during contact, so that the

resultant particle in Case 2 will not gain as many electrons as the resultant particle from Case 1. In Case 3, the potential of the wall is equal to the potential of the particle, and no charge transfer occurs between the particle and the wall. In Case 4, a strong electric field is applied to the wall such that the potential of the wall is higher than the work function of the particle. In this case, the vacuum level is shown for the wall as more energy is required to remove electrons from the surface of the wall than from the particle's surface. In Case 4, electrons transfer from the particle to the wall and particles becomes positively charged. The examples shown in Cases 2, 3, and 4 suggest that electric field can directly influence how particles are charged. The particle charger used in this study builds upon this concept. In the particle charger, the electric field is intentionally applied to the wall surface to artificially modify the potential difference between the particle and the wall. The charge of the impacted particle is directly related to the applied electric field.

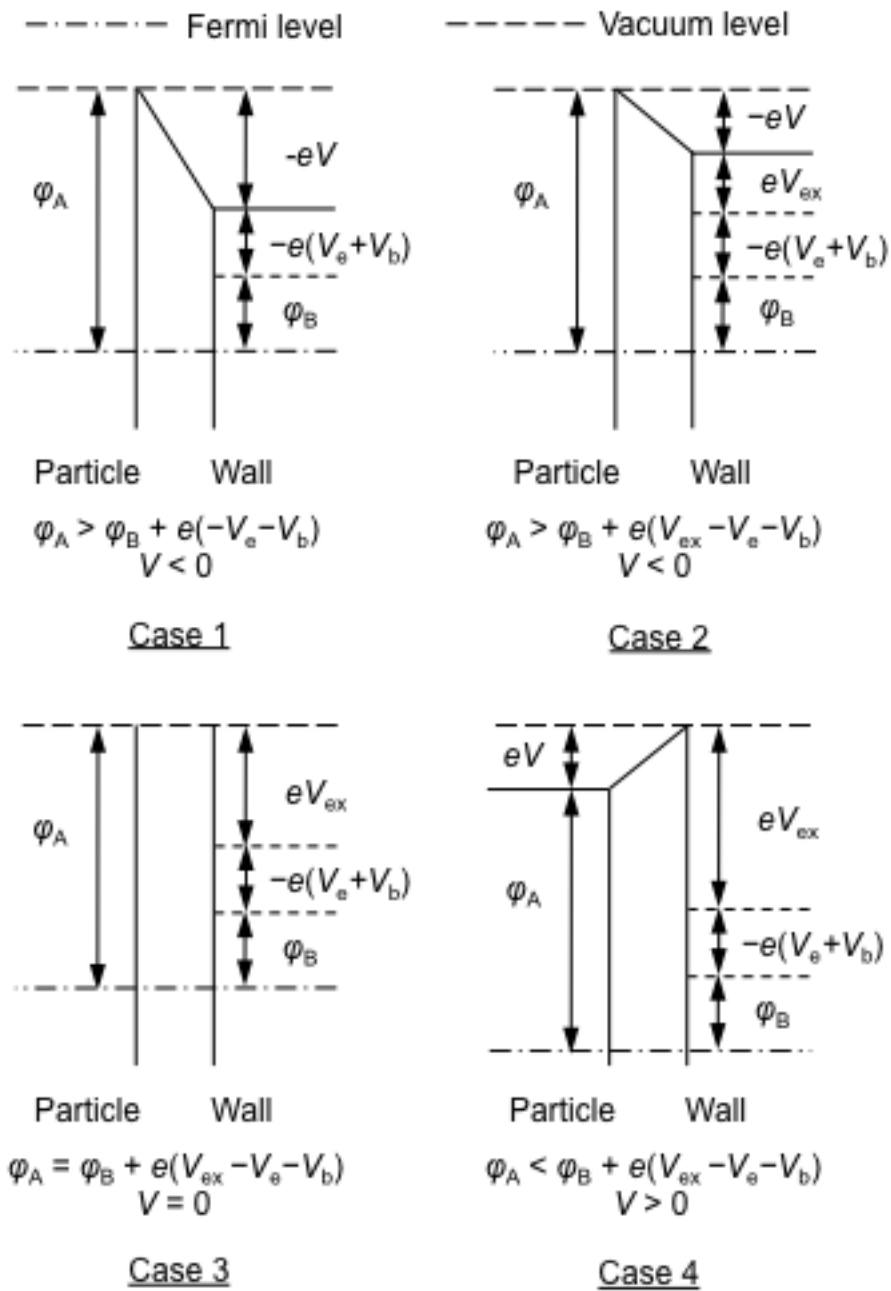


Figure A-1. Different cases of contact charge transfer in applied electric field

APPENDIX B
RAW DATA FOR PARTICLE CHARGING EXPERIMENT

Table B-1. Raw data for borosilicate particle-copper pipe system

Electric field (kV/m)	$q_{m,0}$ ($\mu\text{C}/\text{kg}$)	$q_m(L=1)$ ($\mu\text{C}/\text{kg}$)	
0		-274	-234
100		-198	-169
200		-152	-132
300		-117	-105
400		-91	-58
500		-34	-33
600		-10	-22
700		14	-4
800		41	11
900		50	16
1000		26	

Table B-2. Raw data for borosilicate particle-stainless steel pipe system

Electric field (kV/m)	$q_{m,0}$ ($\mu\text{C}/\text{kg}$)	$q_m(L=1)$ ($\mu\text{C}/\text{kg}$)	
0		-274	-153
100		-198	-139
200		-152	-127
300		-117	-112
400		-91	-98
500		-34	-96
600		-10	-83
700		14	-79
800		41	-73
900		50	-76

Table B-3. Raw data for borosilicate particle-natural glass pipe system

Electric field (kV/m)	$q_{m,0}$ ($\mu\text{C}/\text{kg}$)	$q_m(L=1)$ ($\mu\text{C}/\text{kg}$)	
0		-274	-210
100		-198	-115
200		-152	-75
300		-117	-47
400		-91	9
500		-34	26
600		-10	50
700		14	72
800		41	88
900		50	98

Table B-4. Raw data for borosilicate particle-pyrex pipe system

Electric field (kV/m)	$q_{m,0}$ ($\mu\text{C}/\text{kg}$)	$q_m(L=1)$ ($\mu\text{C}/\text{kg}$)	
0		-286	-260
50		-239	-195
100		-196	-161
150		-171	-135
200		-146	-114
300		-105	-84
400		-82	-41
500		-50	-17
600		-17	13
700		15	31
800		34	56
900		46	60

Table B-5. Raw data for soda lime particle-copper pipe system

Electric field (kV/m)	$q_{m,0}$ ($\mu\text{C}/\text{kg}$)	$q_m(L=1)$ ($\mu\text{C}/\text{kg}$)	
0		-240	-174
100		-195	-152
200		-156	-119
300		-137	-106
400		-109	-83
500		-95	-73
600		-80	-67
700		-75	-56
800		-61	-50
900		-53	-41
1100		-48	

Table B-6. Raw data for soda lime particle-stainless steel pipe system

Electric field (kV/m)	$q_{m,0}$ ($\mu\text{C}/\text{kg}$)	$q_m(L=1)$ ($\mu\text{C}/\text{kg}$)	
0		-240	-99
100		-195	-92
200		-156	-82
300		-137	-72
400		-109	-69
500		-95	-66
600		-80	-61
700		-75	-58
800		-61	-59
900		-53	-56

Table B-7. Raw data for soda lime particle-natural glass pipe system

Electric field (kV/m)	$q_{m,0}$ ($\mu\text{C}/\text{kg}$)	$q_m(L=1)$ ($\mu\text{C}/\text{kg}$)	
0		-240	-194
100		-195	-162
200		-156	-125
300		-137	-101
400		-109	-86
500		-95	-67
600		-80	-58
700		-75	-44
800		-61	-34
900		-53	-26

Table B-8. Raw data for soda lime particle-pyrex pipe system

Electric field (kV/m)	$q_{m,0}$ ($\mu\text{C}/\text{kg}$)	$q_m(L=1)$ ($\mu\text{C}/\text{kg}$)	
0		-240	-202
100		-195	-169
200		-156	-133
300		-137	-104
400		-109	-86
500		-95	-72
600		-80	-62
700		-75	-50
800		-61	-40
900		-53	-37

Table B-9. Raw data for PMMA particle-copper pipe system

Electric field (kV/m)	$q_{m,0}$ ($\mu\text{C}/\text{kg}$)	$q_m(L=1)$ ($\mu\text{C}/\text{kg}$)
0		2249
100		967
200		766
300		579
400		509
500		537
600		407
700		352
800		326
900		211

Table B-10. Raw data for PMMA particle-stainless steel pipe system

Electric field (kV/m)	$q_{m,0}$ ($\mu\text{C}/\text{kg}$)	$q_m(L=1)$ ($\mu\text{C}/\text{kg}$)
0		2249
100		967
200		766
300		579
400		509
500		537
600		407
700		352
800		326
900		211

Table B-11. Raw data for PMMA particle-natural glass pipe system

Electric field (kV/m)	$q_{m,0}$ ($\mu\text{C}/\text{kg}$)	$q_m(L=1)$ ($\mu\text{C}/\text{kg}$)	
0		2249	1477
100		967	912
200		766	682
300		579	620
400		509	546
500		537	493
600		407	455
700		352	391
800		326	311
900		211	261

Table B-12. Raw data for PMMA particle-pyrex pipe system

Electric field (kV/m)	$q_{m,0}$ ($\mu\text{C}/\text{kg}$)	$q_m(L=1)$ ($\mu\text{C}/\text{kg}$)	
0		2249	1638
100		967	857
200		766	701
300		579	530
400		509	479
500		537	474
600		407	394
700		352	337
800		326	314
900		211	203

Table B-13. Raw data for crushed soda lime particle-copper pipe system

Electric field (kV/m)	$q_{m,0}$ ($\mu\text{C}/\text{kg}$)	$q_m(L=1)$ ($\mu\text{C}/\text{kg}$)	
0		-65	-45
100		-21	-22
150		-19	-11
200		-9	-2
300		13	11
400		27	26
500		44	36
600		51	47
700		59	51
800		61	47
900		60	55
1000		61	
1100		56	

Table B-14. Raw data for crushed soda lime particle-copper pipe system

Electric field (kV/m)	$q_{m,0}$ ($\mu\text{C}/\text{kg}$)	$q_m(L=1)$ ($\mu\text{C}/\text{kg}$)	
0		-65	-41
100		-21	-17
150		-19	-11
200		-9	-5
300		13	5
400		27	13
500		44	22
600		51	26
700		59	32
800		61	34
900		60	33

Table B-15. Raw data for crushed soda lime particle-copper pipe system

Electric field (kV/m)	$q_{m,0}$ ($\mu\text{C}/\text{kg}$)	$q_m(L=1)$ ($\mu\text{C}/\text{kg}$)	
0		-65	-39
100		-21	-13
150		-19	1
200		-9	8
300		13	27
400		27	41
500		44	54
600		51	67
700		59	70
800		61	70
900		60	72

Table B-16. Raw data for crushed soda lime particle-copper pipe system

Electric field (kV/m)	$q_{m,0}$ ($\mu\text{C}/\text{kg}$)	$q_m(L=1)$ ($\mu\text{C}/\text{kg}$)	
0		-65	-44
100		-21	-15
150		-19	-8
200		-9	6
300		13	24
400		27	41
500		44	54
600		51	63
700		59	68
800		61	70
900		60	73

Table B-17. Raw data for JSC-1A particle-copper pipe system

Electric field (kV/m)	$q_{m,0}$ ($\mu\text{C}/\text{kg}$)	$q_m(L=1)$ ($\mu\text{C}/\text{kg}$)
0	-189	-166
100	-93	-99
200	-31	-50
300	14	-15
400	44	3
500	61	22
600	69	29
700	70	31
800	63	
900	48	
1000	38	

Table B-18. Raw data for JSC-1A particle-Stainless steel pipe system

Electric field (kV/m)	$q_{m,0}$ ($\mu\text{C}/\text{kg}$)	$q_m(L=1)$ ($\mu\text{C}/\text{kg}$)
0	-189	-103
100	-93	-60
200	-31	-38
300	14	-22
400	44	-13
500	61	-4
600	69	0
700	70	1

Table B-19. Raw data for JSC-1A particle-natural glass pipe system

Electric field (kV/m)	$q_{m,0}$ ($\mu\text{C}/\text{kg}$)	$q_m(L=1)$ ($\mu\text{C}/\text{kg}$)	
0		-189	-131
100		-93	-58
200		-31	2
300		14	40
400		44	66
500		61	86
600		69	93
700		70	98

Table B-20. Raw data for JSC-1A particle-pyrex pipe system

Electric field (kV/m)	$q_{m,0}$ ($\mu\text{C}/\text{kg}$)	$q_m(L=1)$ ($\mu\text{C}/\text{kg}$)	
0		-189	-165
100		-93	-85
200		-31	-20
300		14	24
400		44	50
500		61	66
600		69	80
700		70	81

APPENDIX C PARAMETRIC STUDY

A parametric study was performed to determine the effect of each input on the collision number per unit length, n/L . Each input to the CFD simulation was change independent of other input. The effect of each input on n/L is summarized in Table C-1. The inputs that strongly affect the particle-wall collision are: the mass loading (m), the particle diameter (d_p), the pipe radius (R), the particle-wall coefficient of restitution (e_w), and the specular coefficient (ϕ). The coefficient of restitution and the specular coefficient are functions of particle-pipe system, thus these parameter is changes with different material uses. The important parameters for determining the collision number in the CFD simulation are mass loading, particle diameter, and pipe radius. Unlike what is shown in Chapter 3, the velocity did not affect the collision number per unit length. In the parametric study increasing the air velocity also increase the amount of particles in the system (mass loading is constant); thus the Effect seen in Chapter 2 is included in the mass loading term.

Ema et al (2003) indicated that the charging efficiency for each contact is depended upon the impact angle, (θ). Particle impacting at a certain angle can led up to five times as much charge transfer. The parametric study also looked at the impact angle to determine if this is an issue. The impact angle is found by

$$\tan\theta = \frac{v_s'}{v_s} \quad (C-1)$$

In the CFD model the impact velocity is the same as the fluctuating velocity. The impact angle was determined for each parameter used in the parametric study. The results are also in Table C-1. Impact angle is insensitive to the operating condition, it

change with the pipe radius, the particle-wall coefficient of restitution, and the specular coefficient. The coefficient of restitution and specular coefficient depend on the particle-pipe system. Changing the pipe radius ($R = 1.4\text{m}$ to 7 m) changes the impact angle by about 3° . This is small enough not to cause a significant change in the charge transfer for a straight pipe. The effects of each parameter are documented in Figure C-1 to C-10.

Table C-1. Inputs and outputs for the simulation

Input	Effect on n/L	Effect on impact angle
$\uparrow m$	\downarrow with m	no effect
$\uparrow R$	\downarrow with R	\uparrow with R
$\uparrow V_g$	no effect	no effect
$\uparrow v_0$	no effect	no effect
$\uparrow d_p$	\uparrow with d_p	no effect
$\uparrow \rho_s$	no effect	no effect
$\uparrow \Psi$	no effect	no effect
$\uparrow e_p$	no effect	no effect
$\uparrow e_w$	\uparrow with e_w	\downarrow with e_w
$\uparrow \phi$	\uparrow with ϕ	\downarrow with ϕ

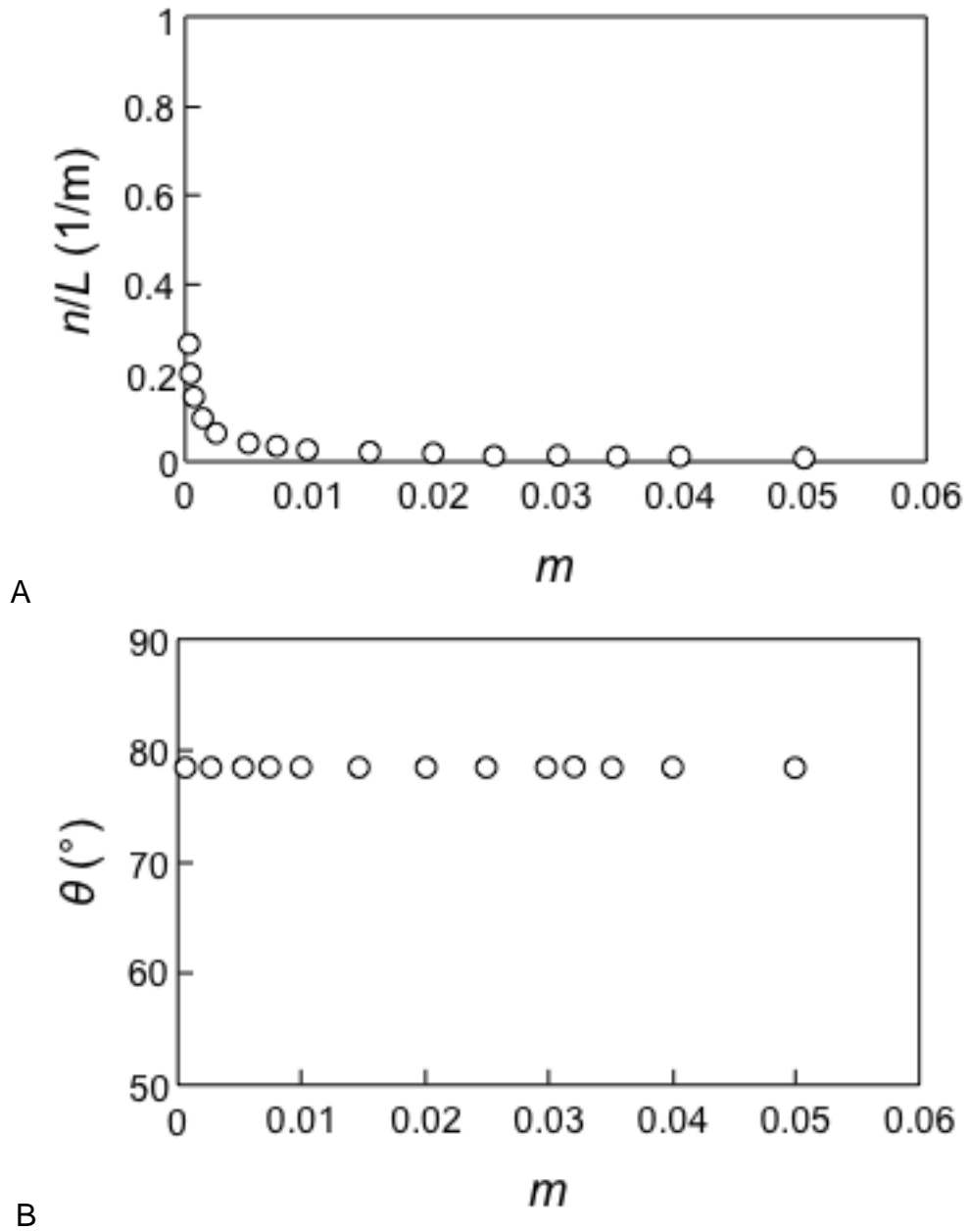


Figure C-1. The effect of mass loading on A) collision frequency per pipe length for a single particle, B) particle-wall impact angle

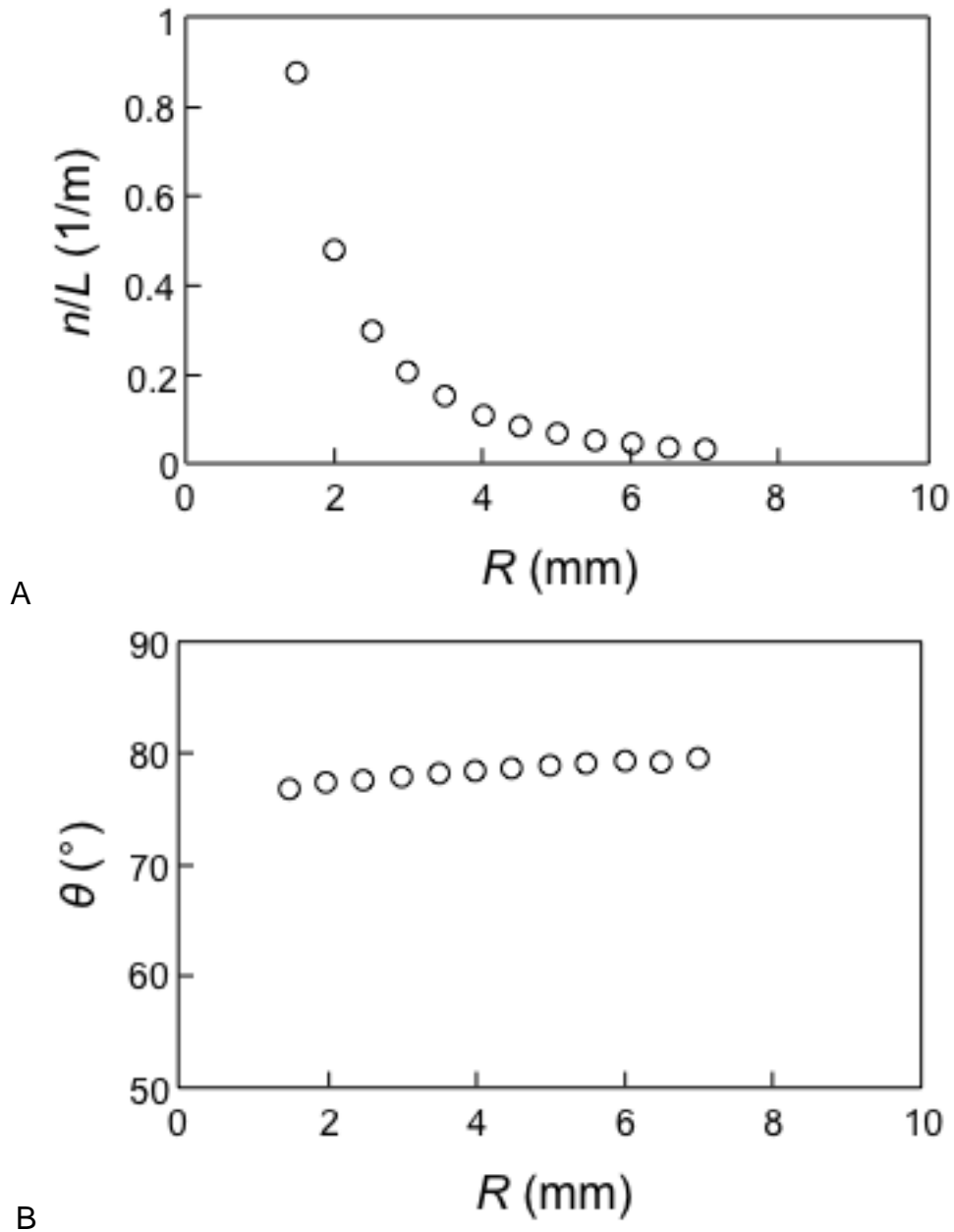


Figure C-2. The effect of pipe radius on A) collision frequency per pipe length for a single particle, B) particle-wall impact angle

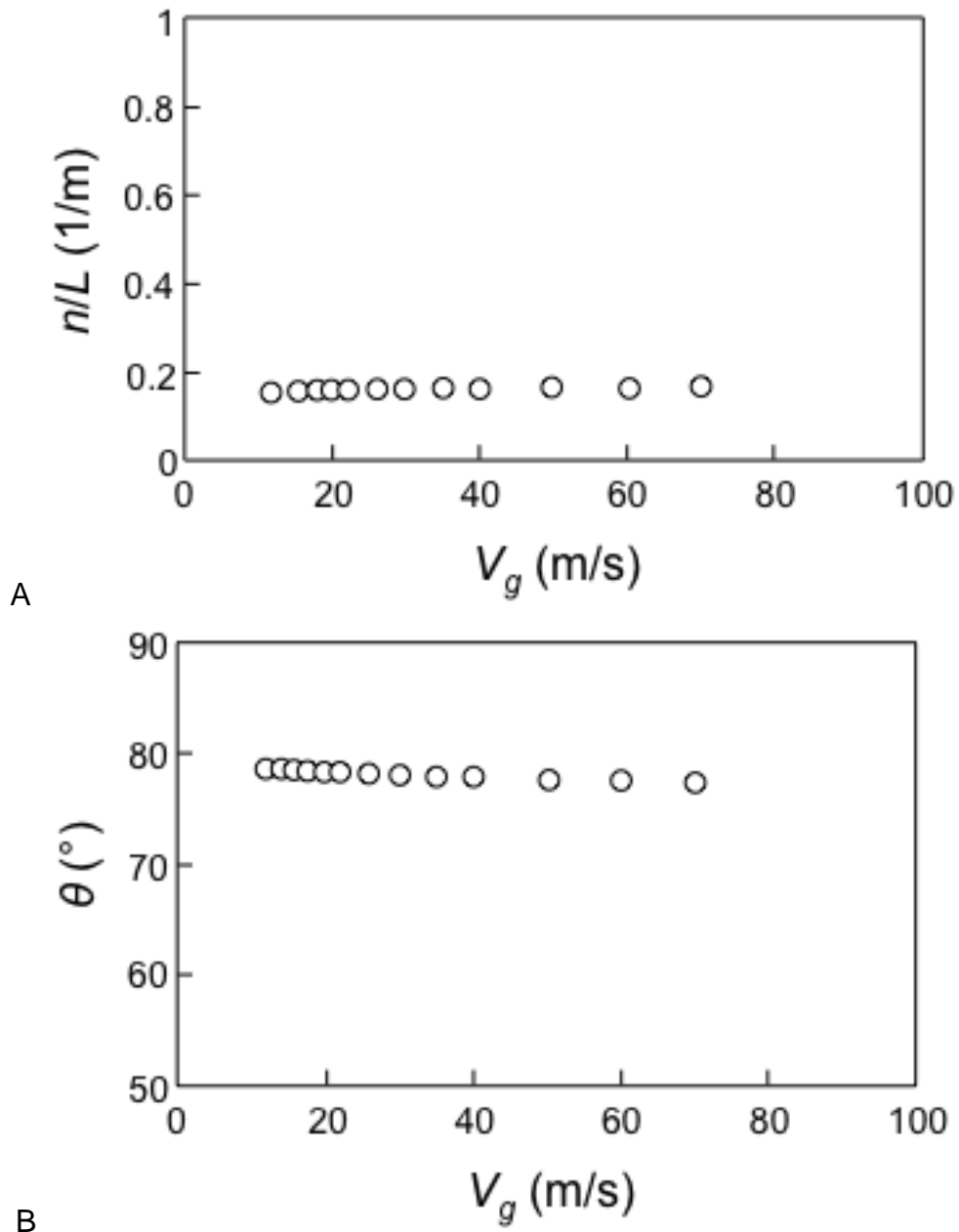


Figure C-3. The effect of mean gas velocity on A) collision frequency per pipe length for a single particle, B) particle-wall impact angle

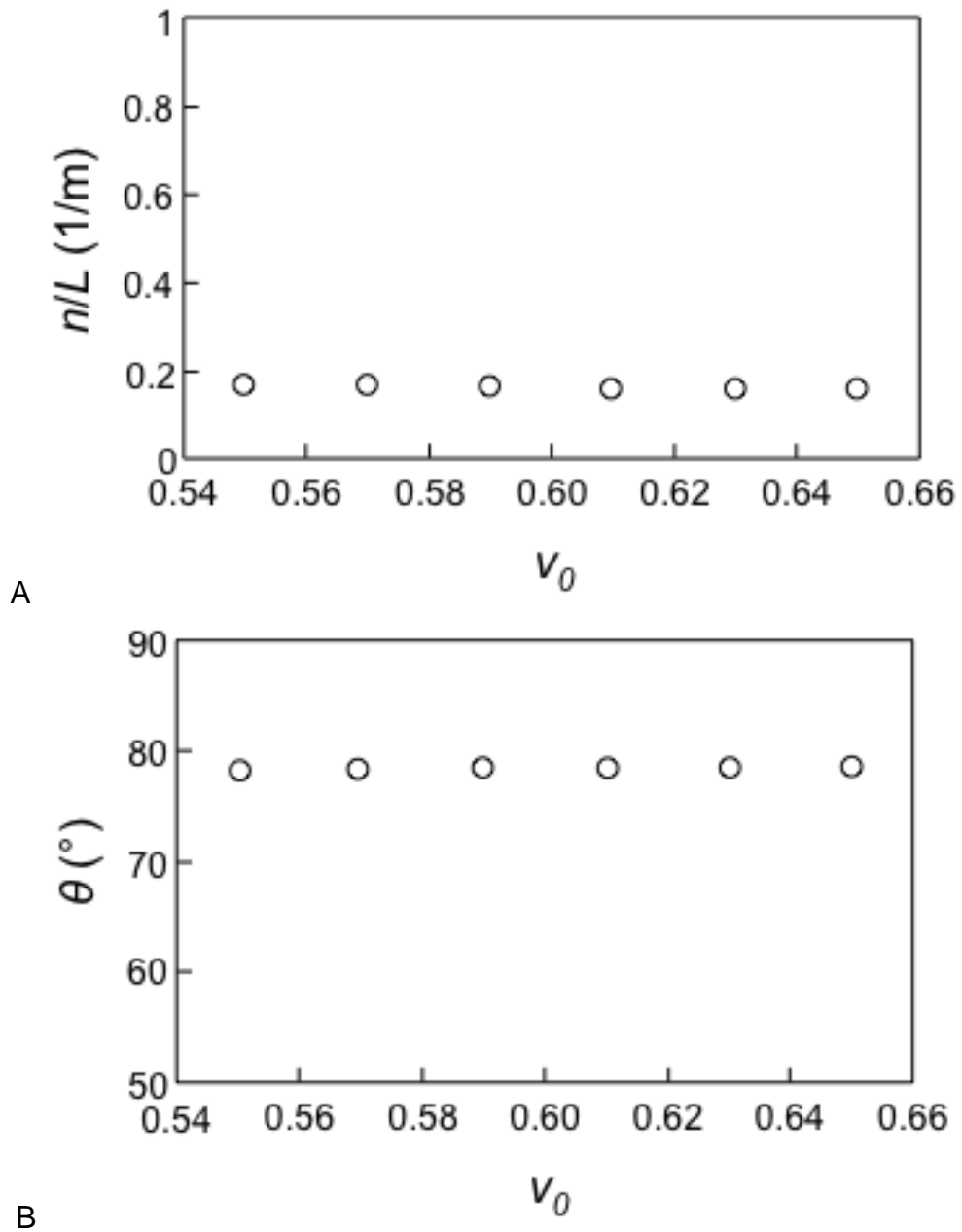


Figure C-4. The effect of maximum solid volume fraction on A) collision frequency per pipe length for a single particle, B) particle-wall impact angle

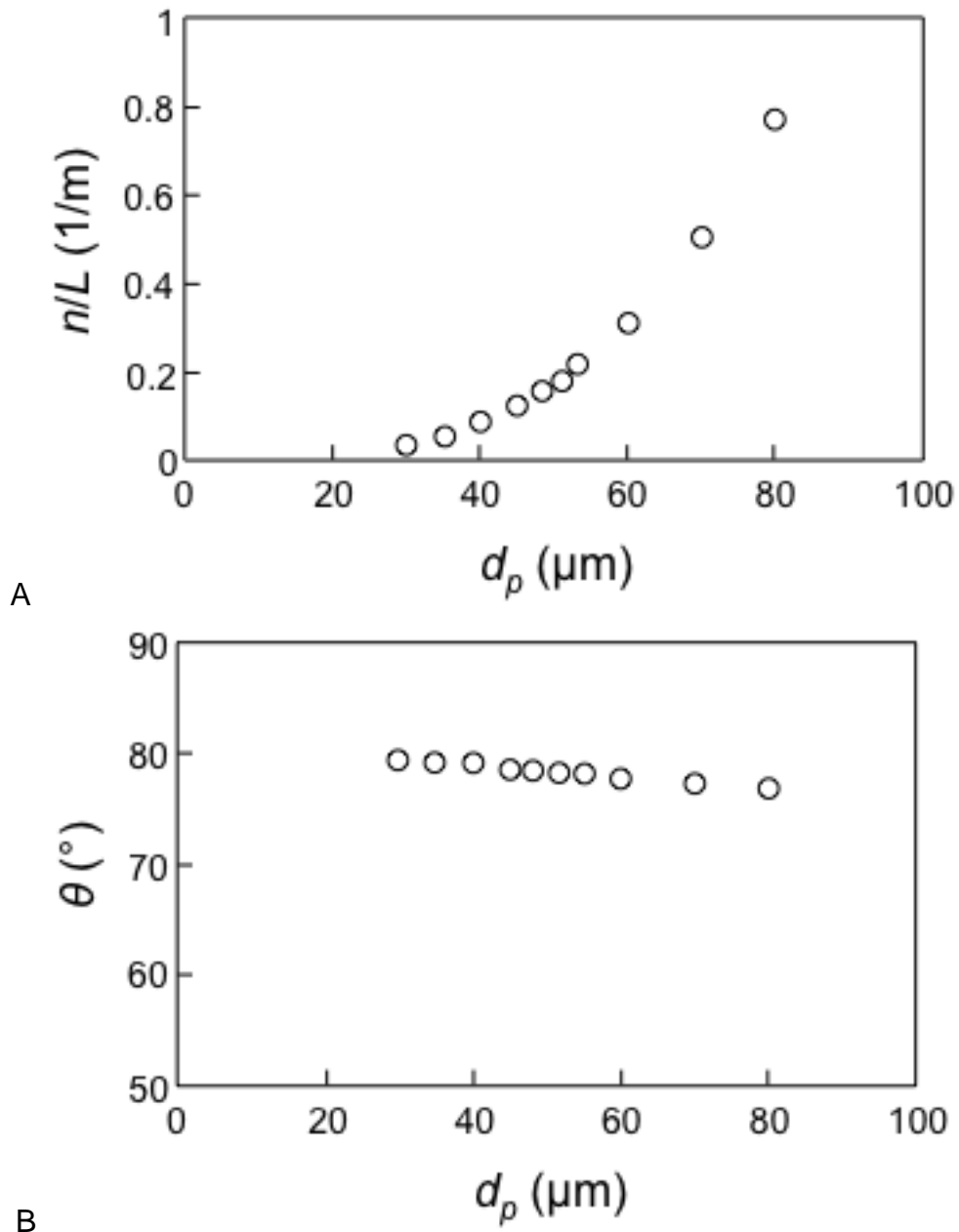


Figure C-5. The effect of particle diameter on A) collision frequency per pipe length for a single particle, B) particle-wall impact angle

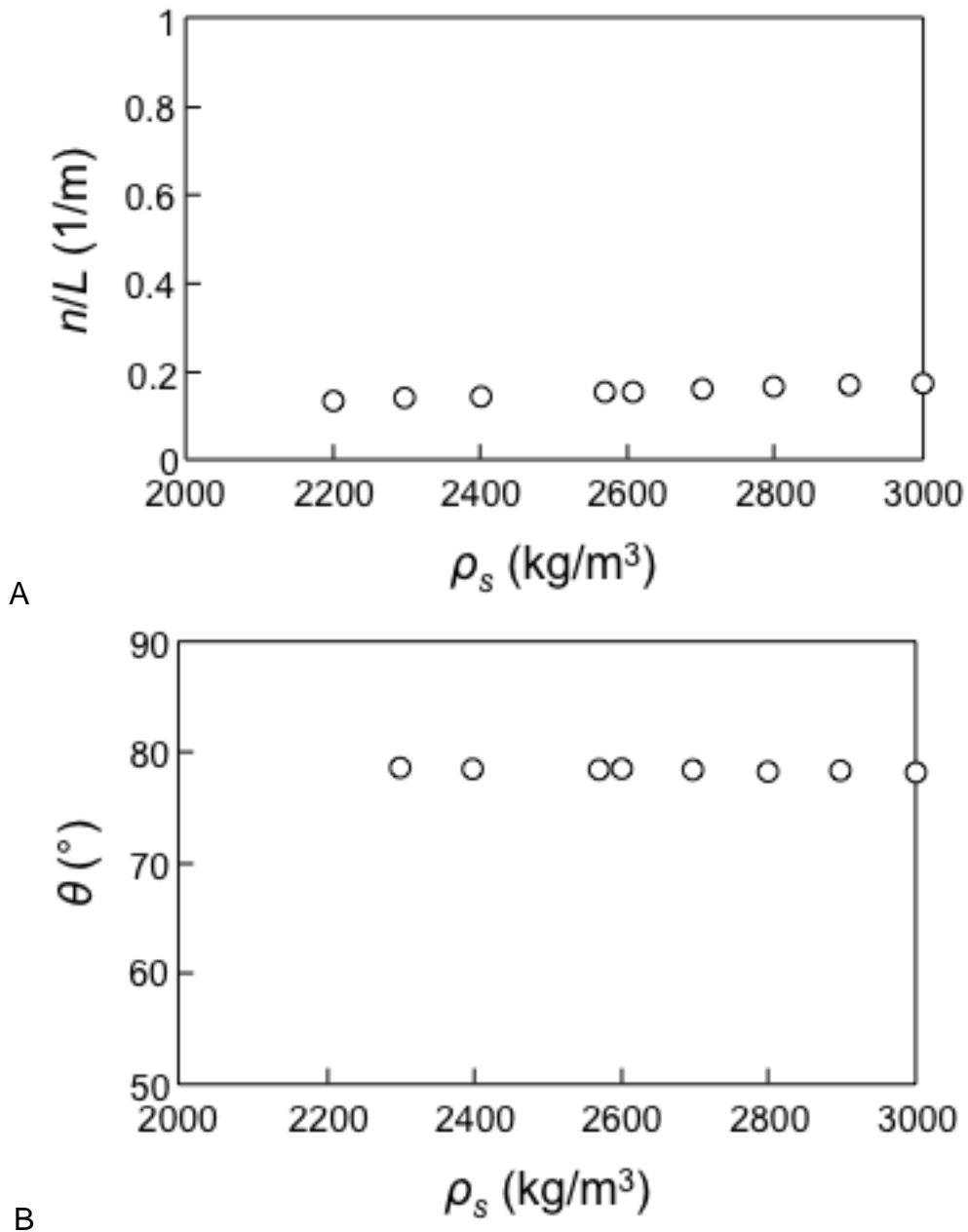


Figure C-6. The effect of particle density on A) collision frequency per pipe length for a single particle, B) particle-wall impact angle

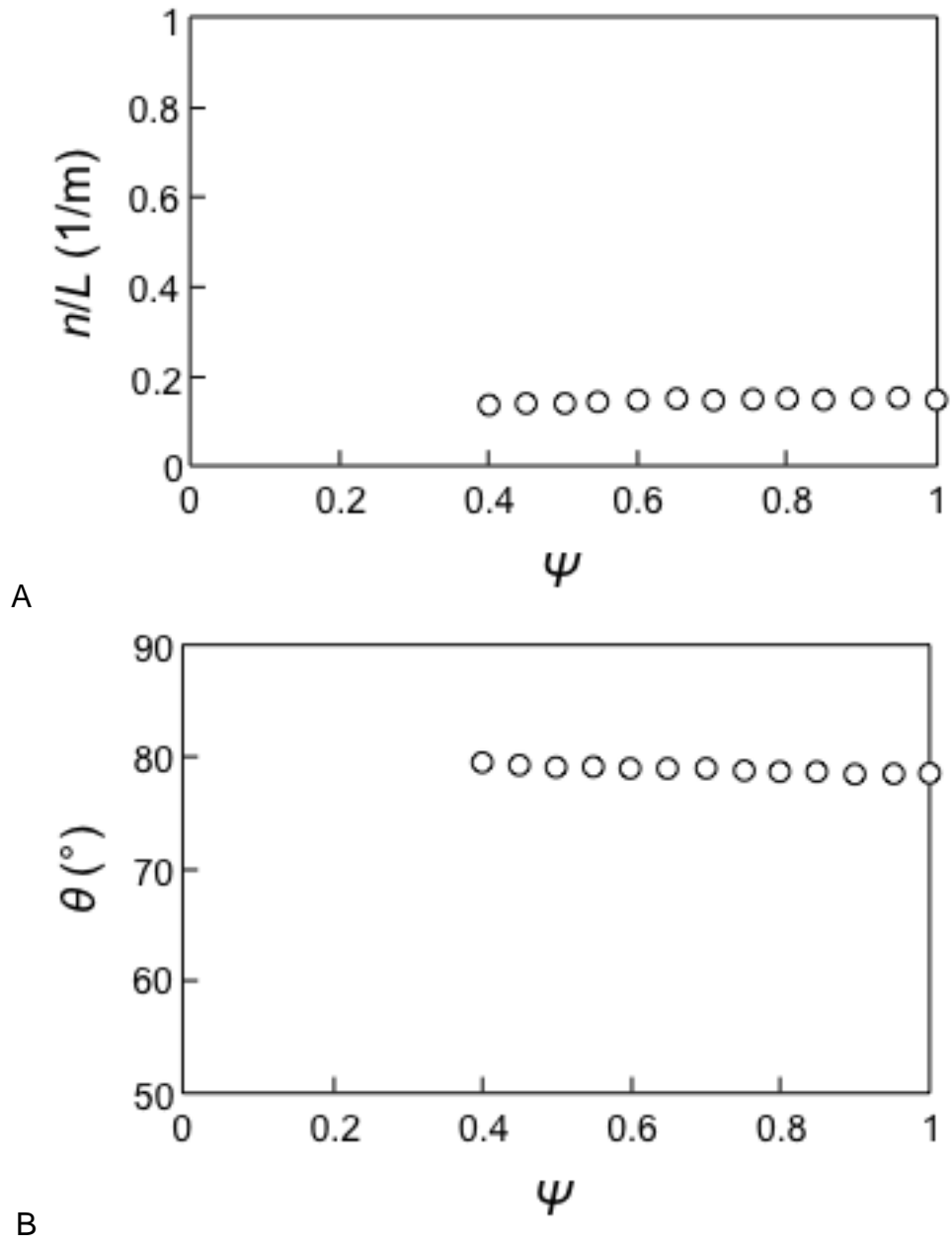


Figure C-7. The effect of particle sphericity on A) collision frequency per pipe length for a single particle, B) particle-wall impact angle

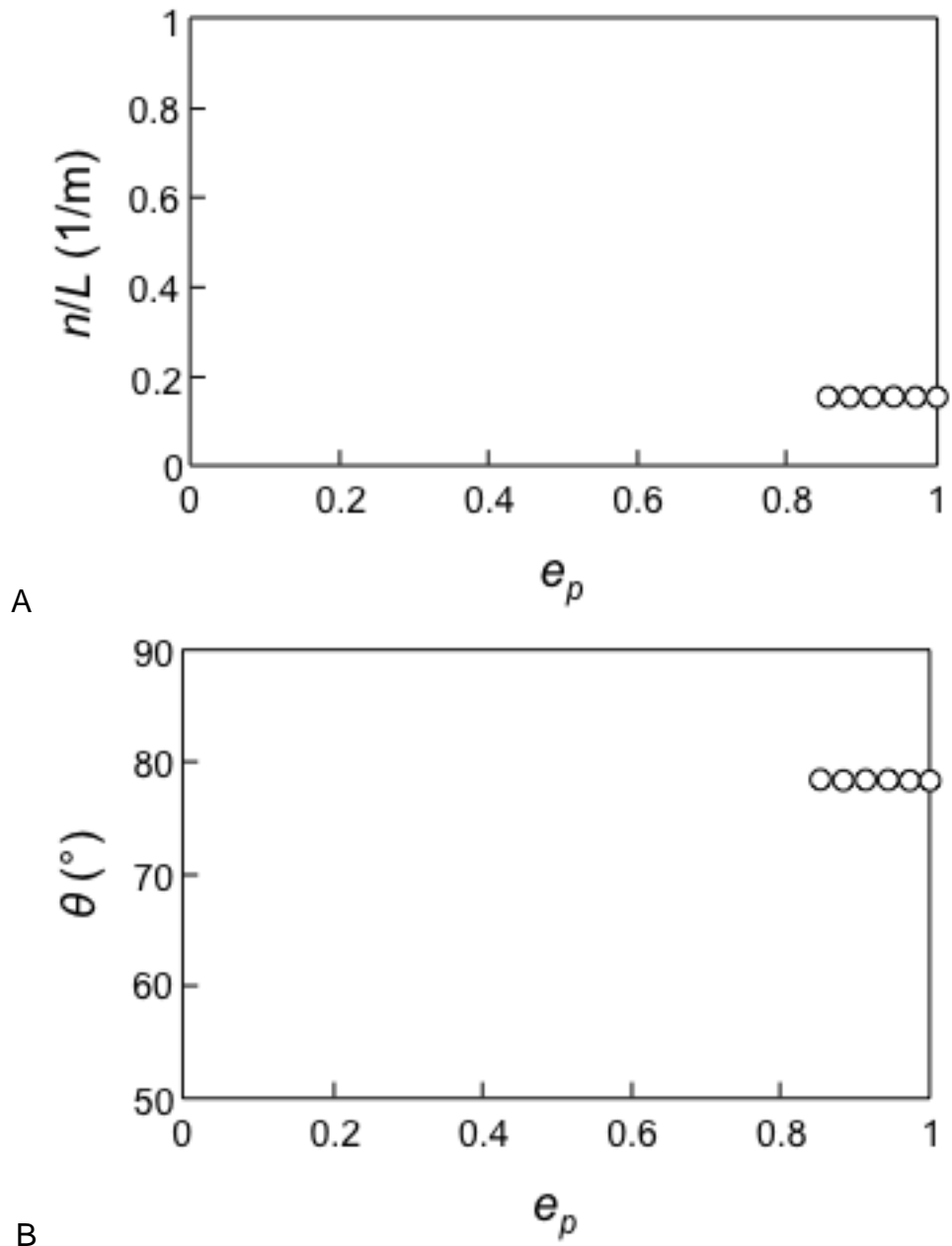


Figure C-8. The effect of particle-particle coefficient of restitution on A) collision frequency per pipe length for a single particle, B) particle-wall impact angle

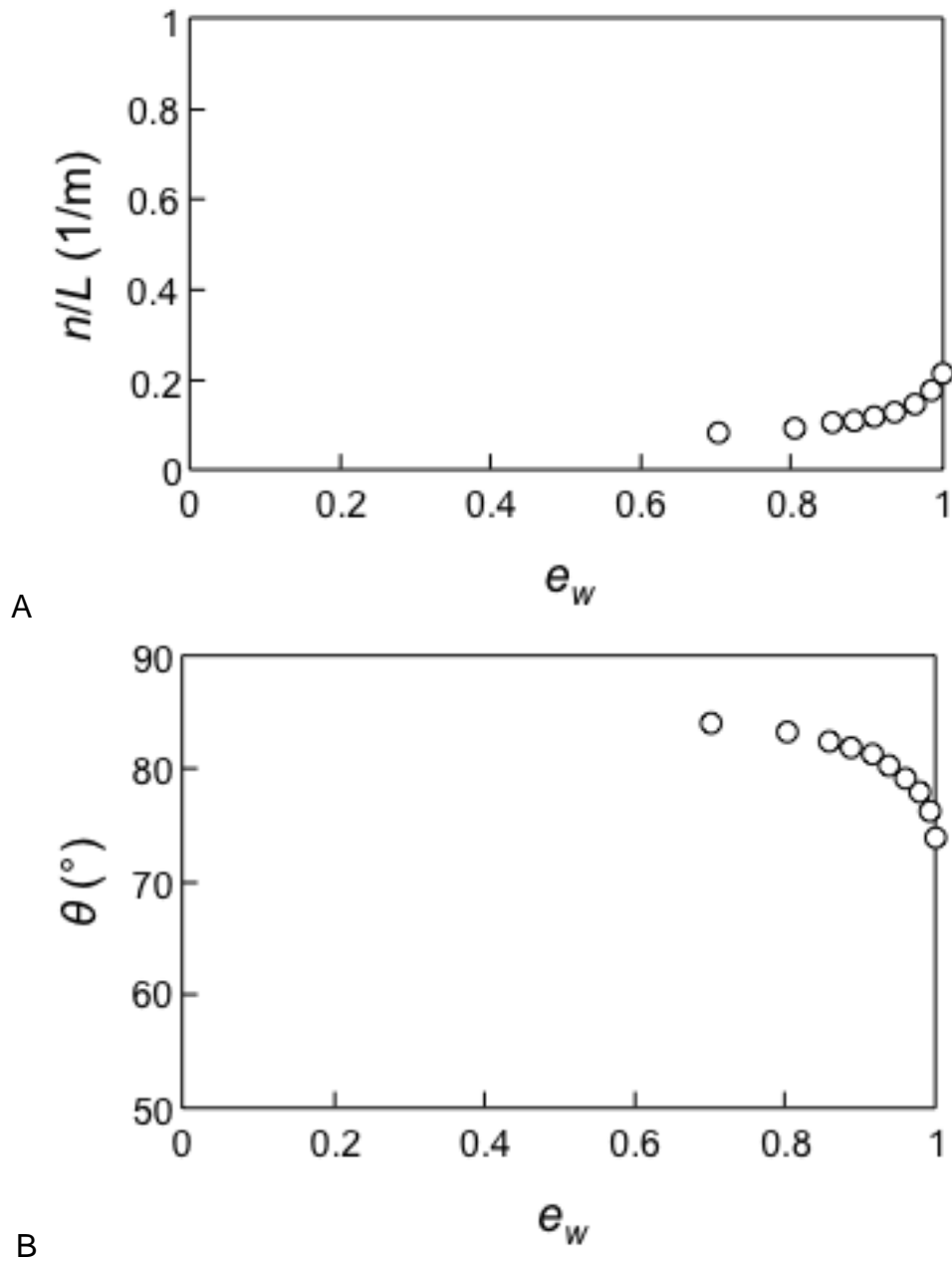


Figure C-9. The effect of particle-wall coefficient of restitution on A) collision frequency per pipe length for a single particle, B) particle-wall impact angle

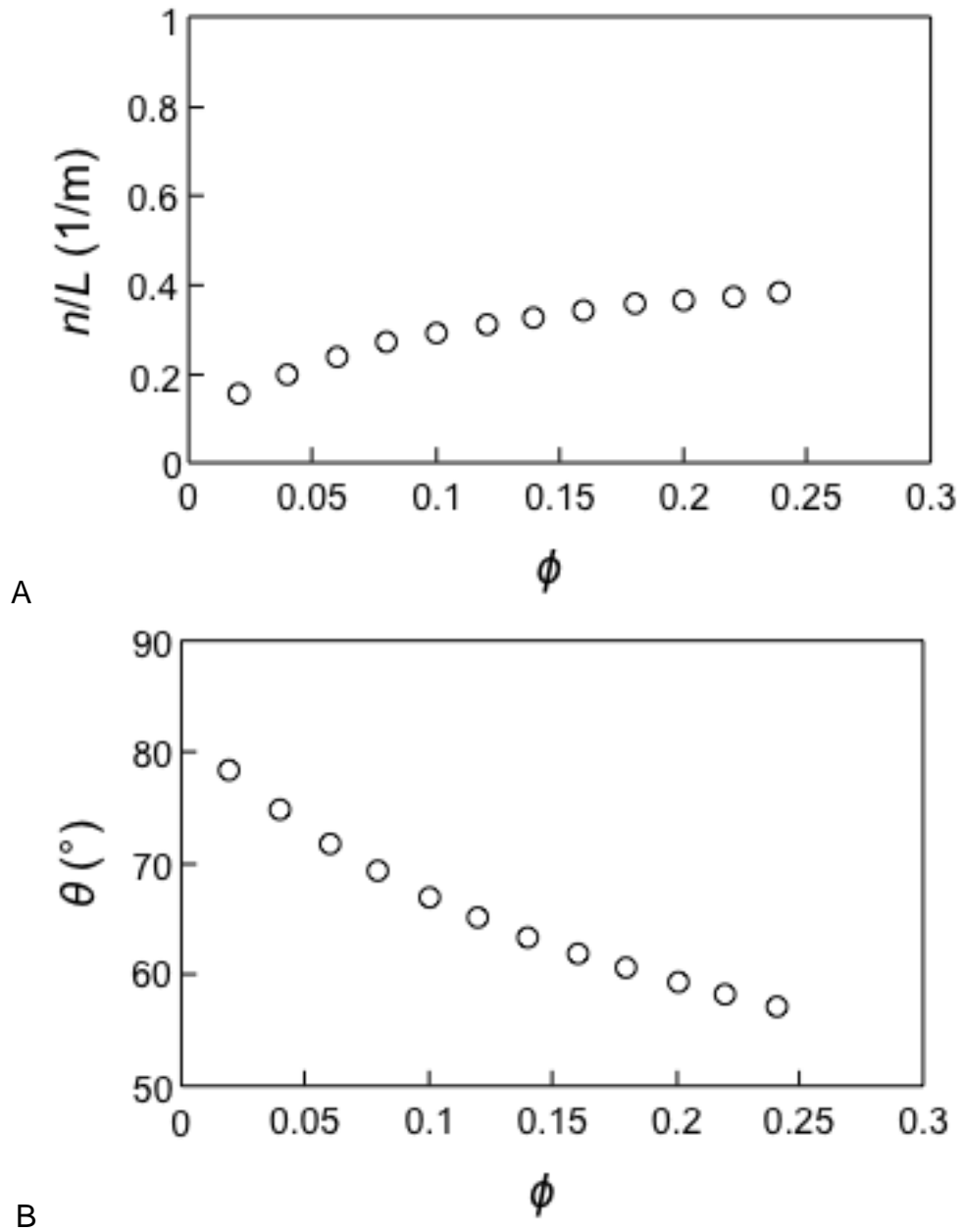


Figure C-10. The effect of wall specularity coefficient on A) collision frequency per pipe length for a single particle, B) particle-wall impact angle

APPENDIX D
ADDITIONAL COMPARISON FOR CHARGE MODEL VALIDATION

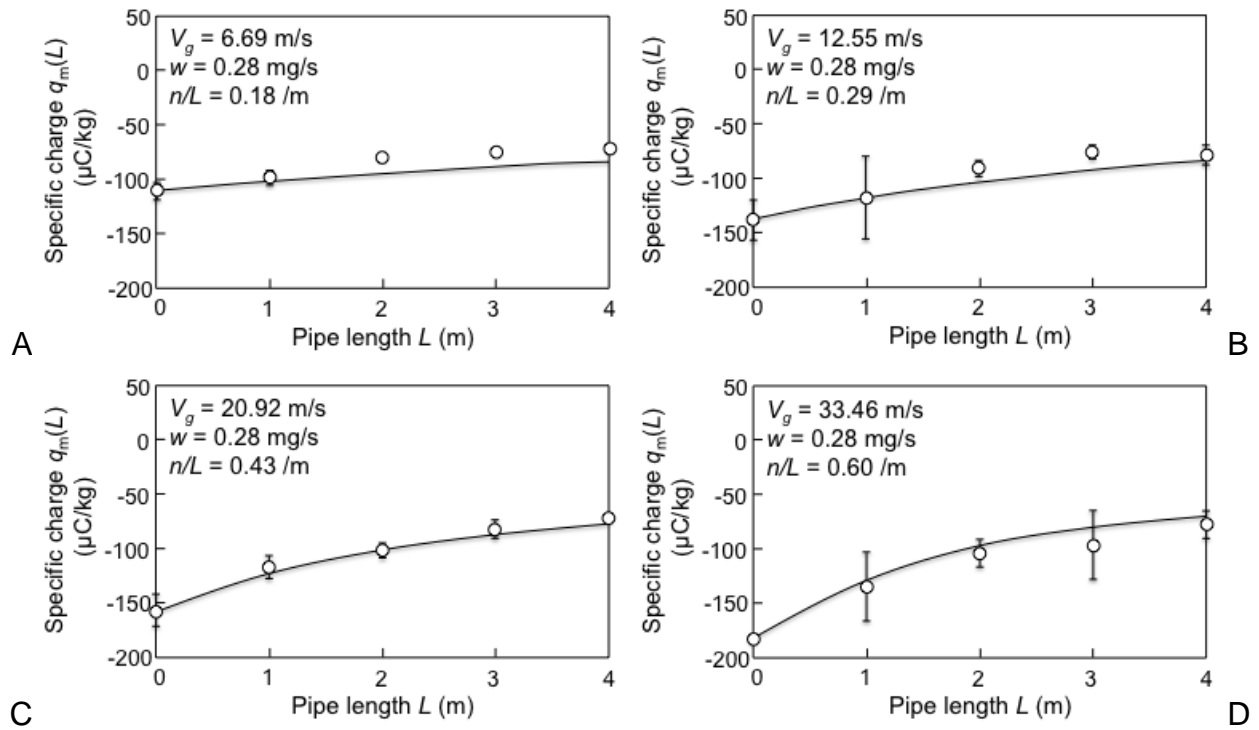


Figure D-1. Comparison for borosilicate particles and copper pipe for different air velocity and mass flow rate

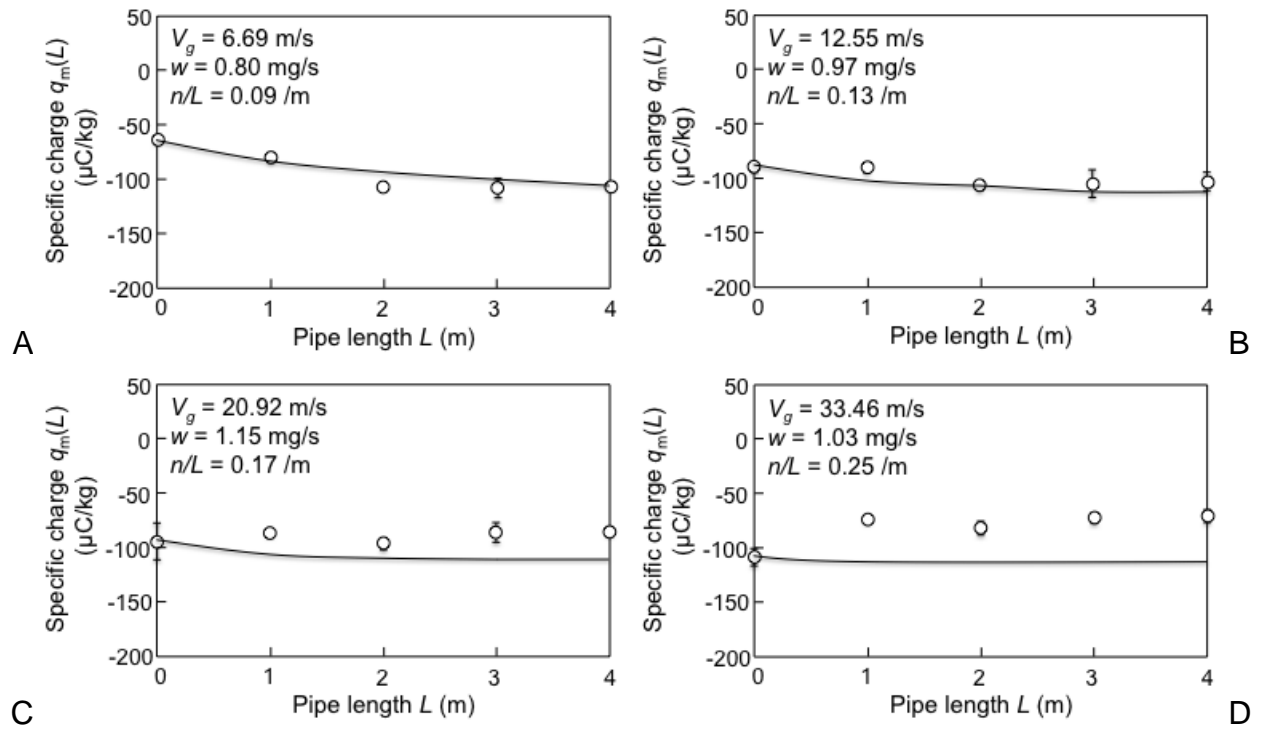


Figure D-2. Comparison for borosilicate particles and stainless steel pipe for different air velocity and mass flow rate

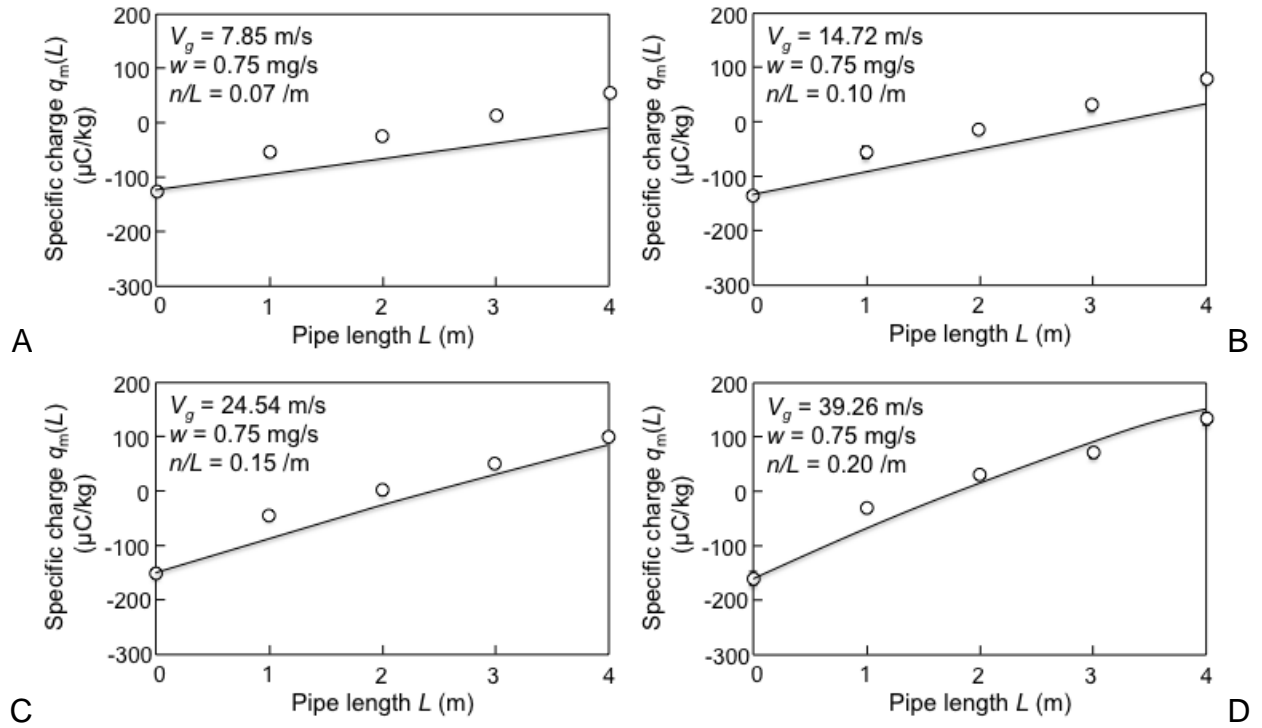


Figure D-3. Comparison for borosilicate particles and natural glass pipe for different air velocity and mass flow rate

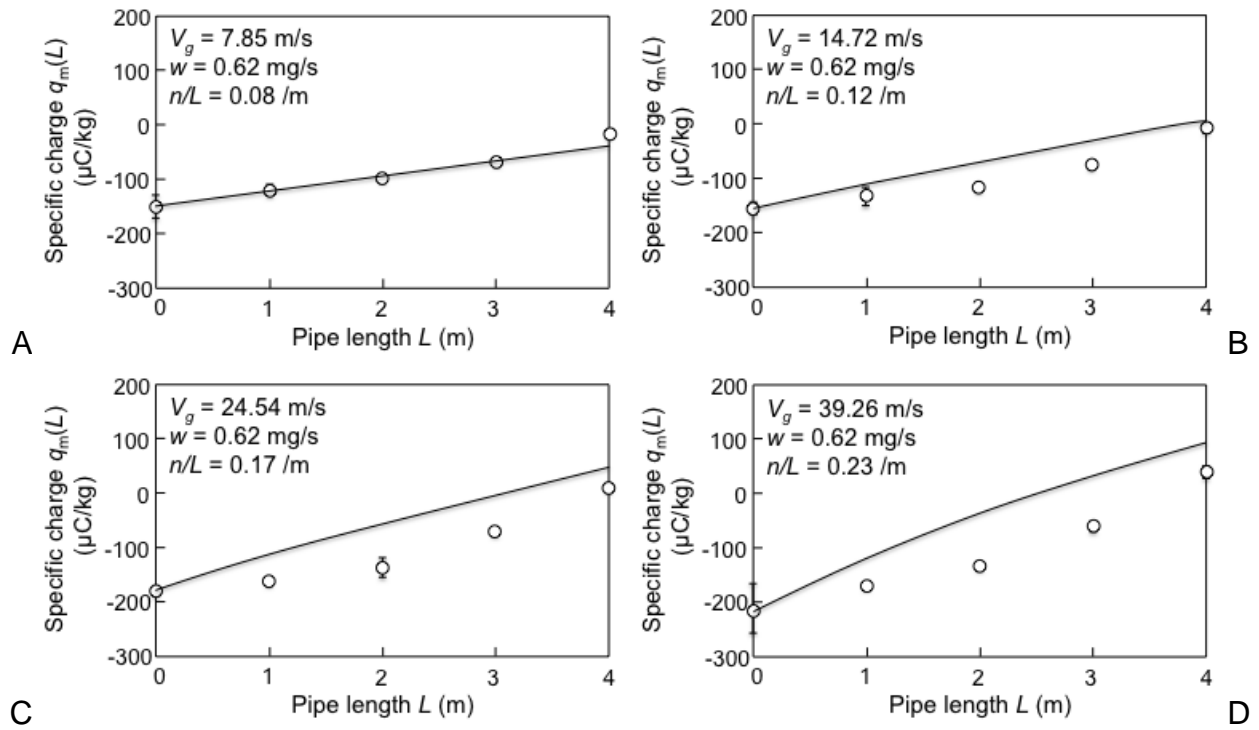


Figure D-4. Comparison for borosilicate particles and Pyrex pipe for different air velocity and mass flow rate

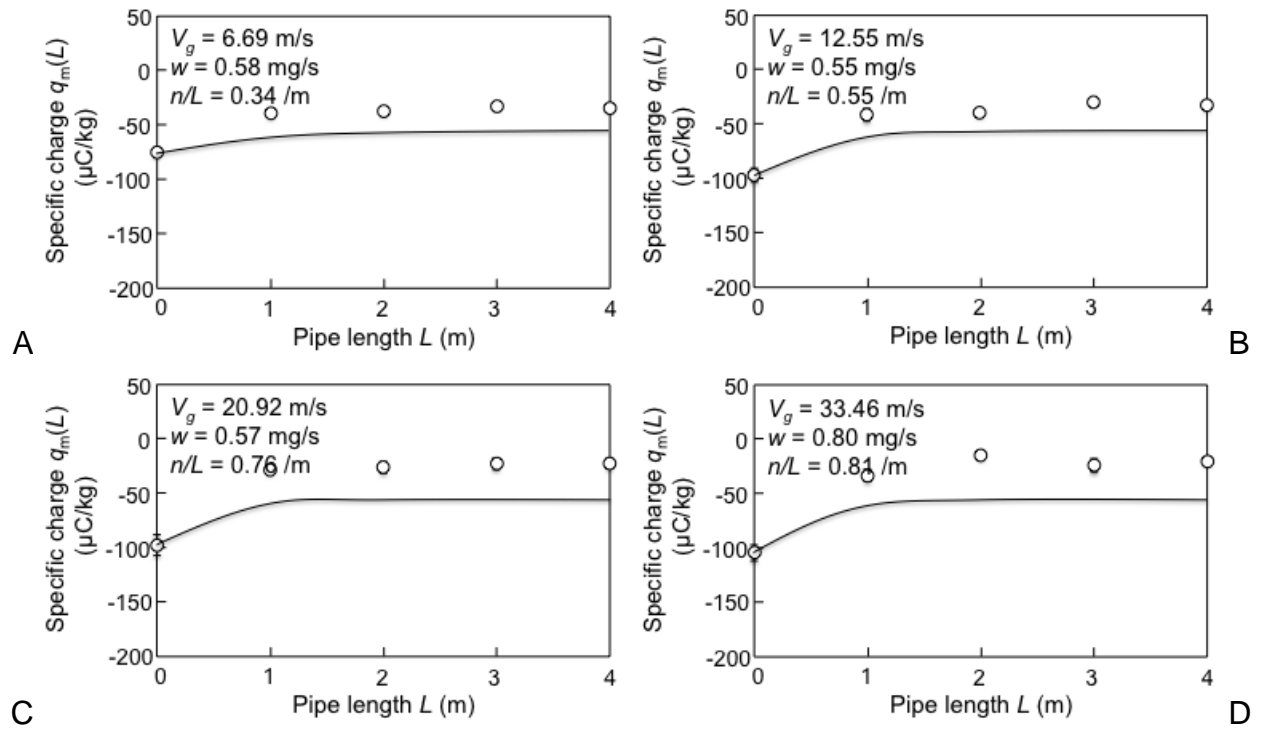


Figure D-5. Comparison for soda lime particles and stainless steel pipe for different air velocity and mass flow rate

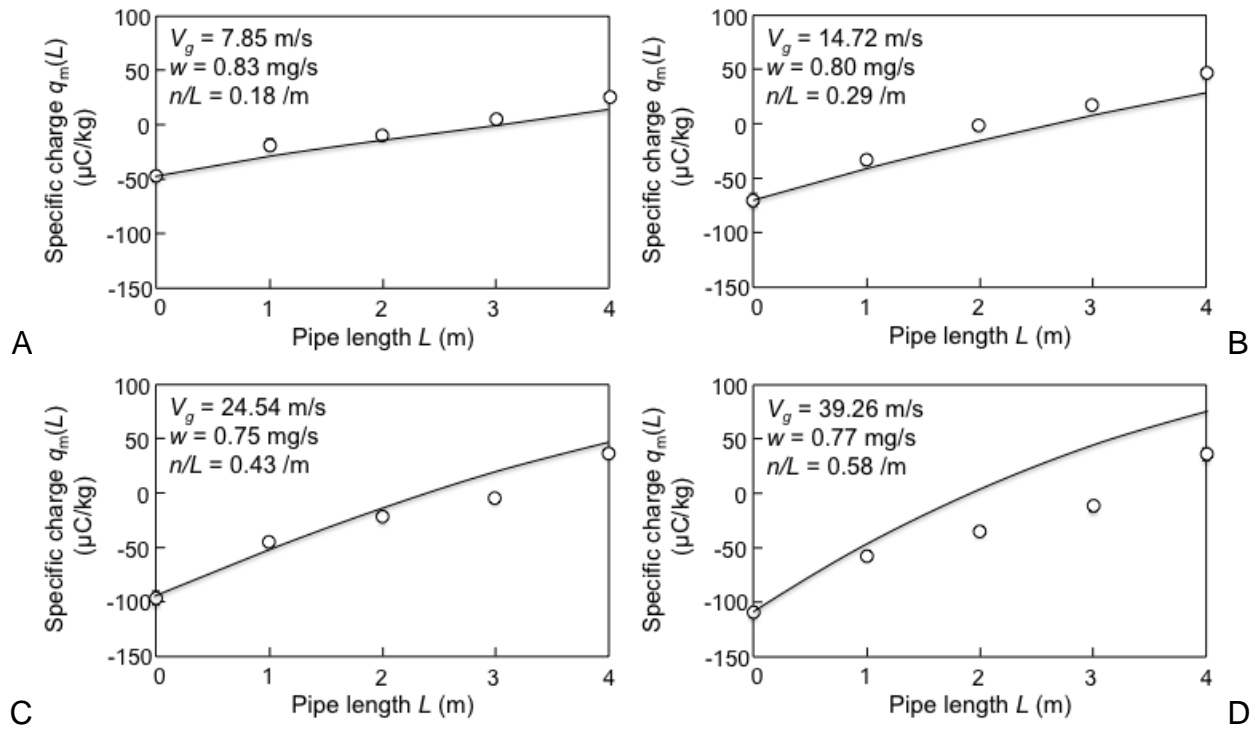


Figure D-6. Comparison for soda lime particles and natural glass pipe for different air velocity and mass flow rate

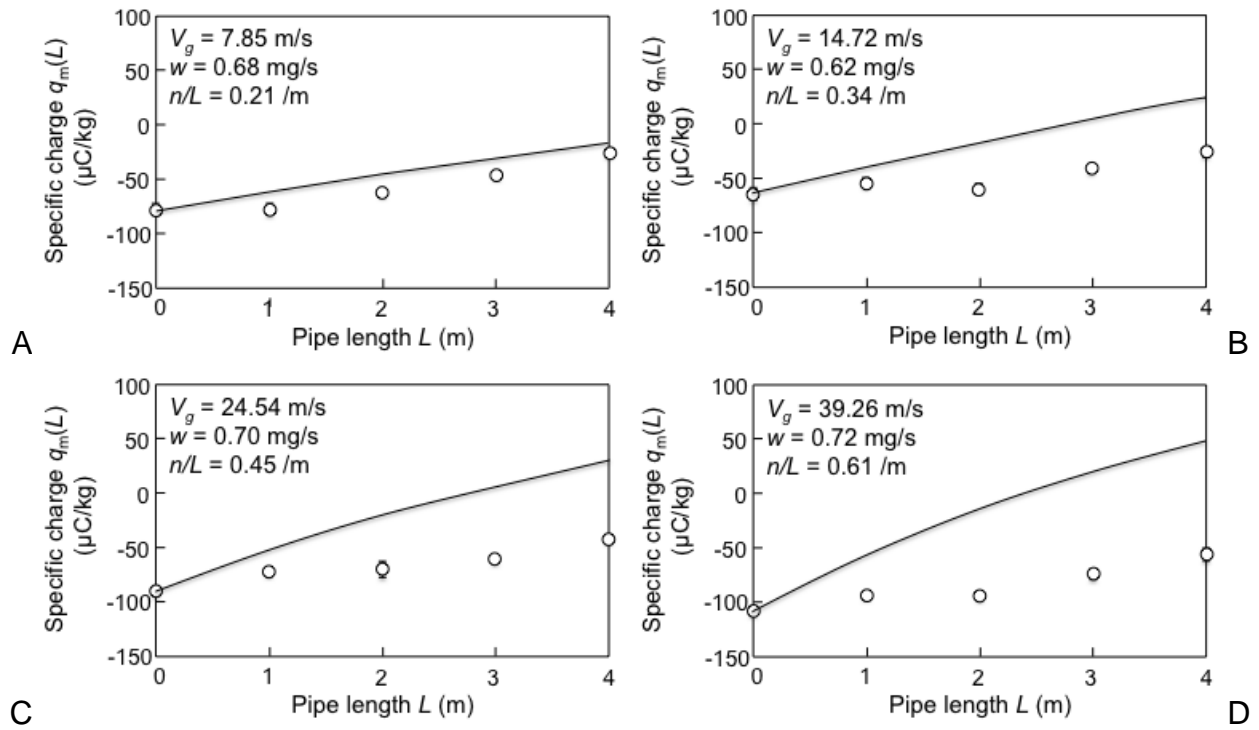


Figure D-7. Comparison for soda lime particles and Pyrex pipe for different air velocity and mass flow rate

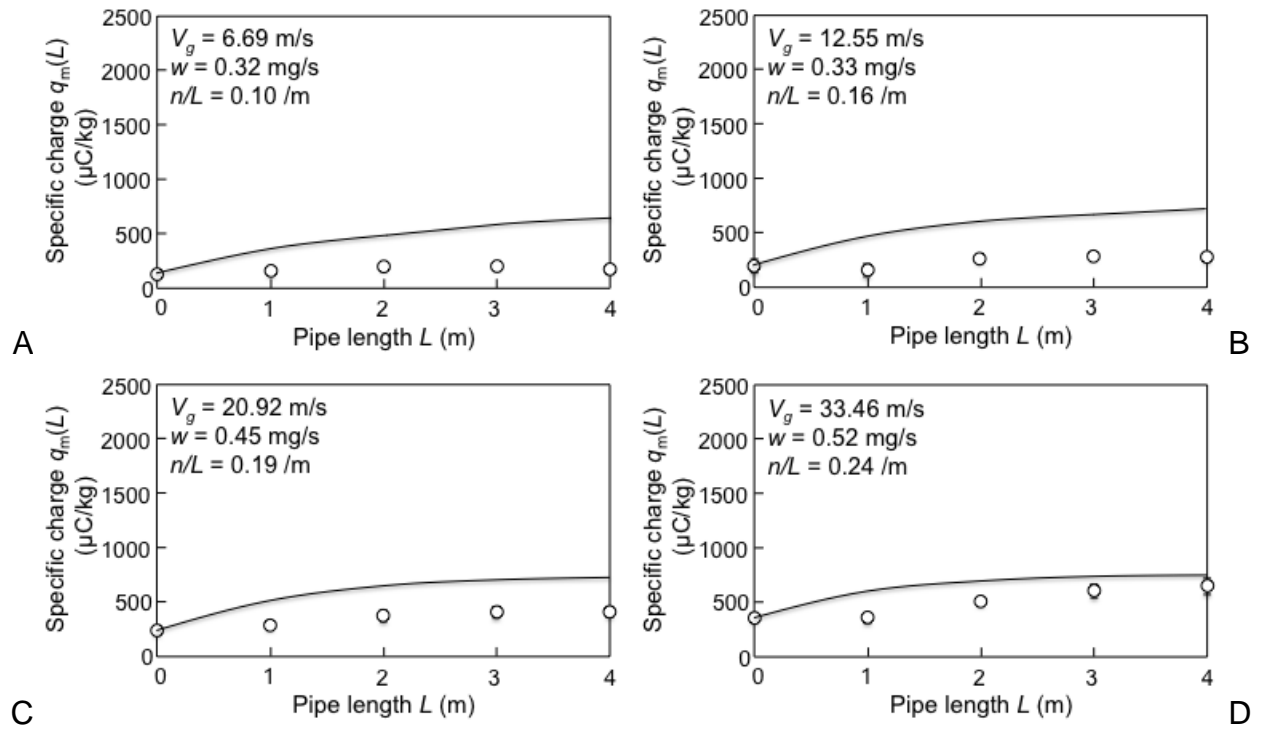


Figure D-8. Comparison for PMMA particles and copper pipe for different air velocity and mass flow rate

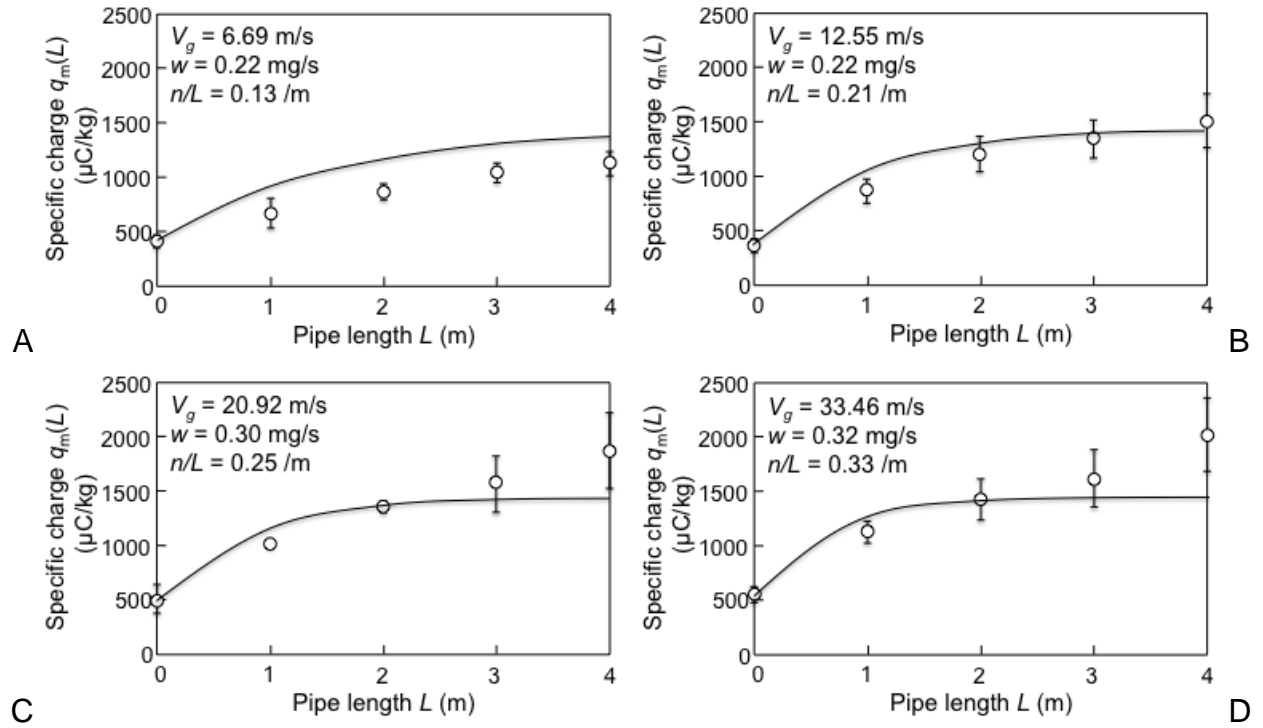


Figure D-9. Comparison for PMMA particles and stainless steel pipe for different air velocity and mass flow rate

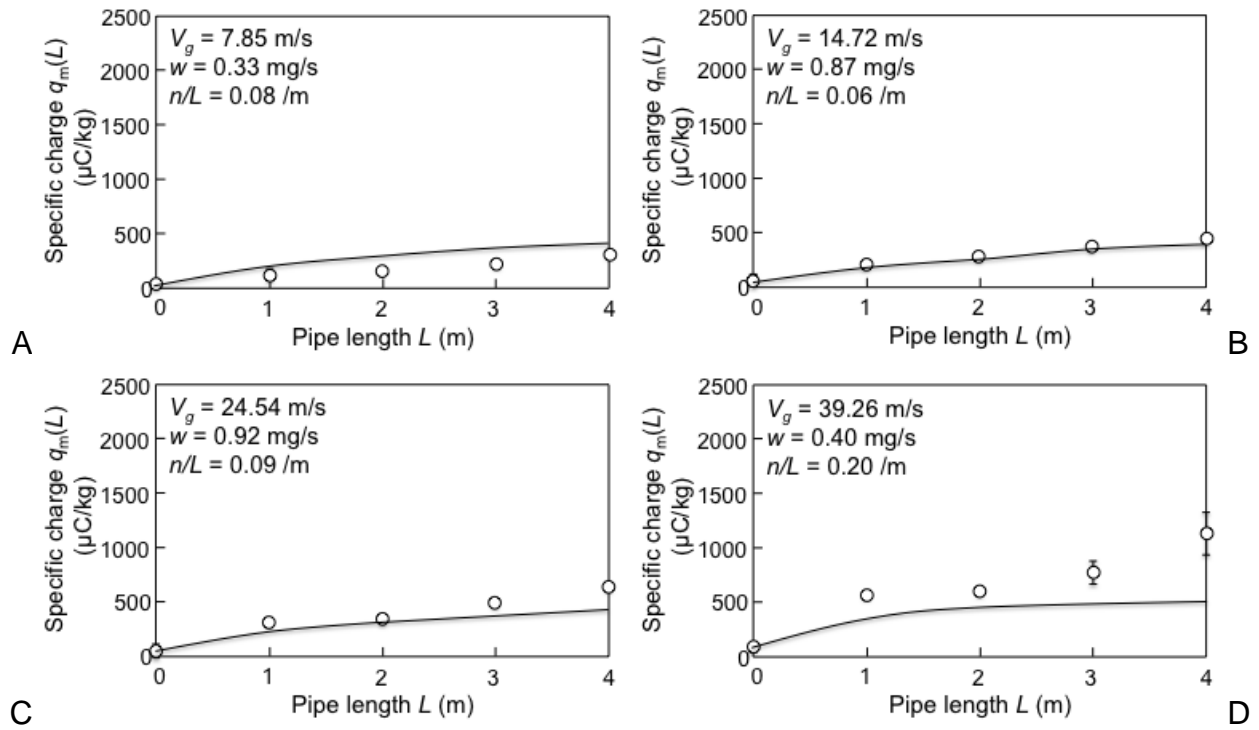


Figure D-10. Comparison for PMMA particles and natural glass pipe for different air velocity and mass flow rate

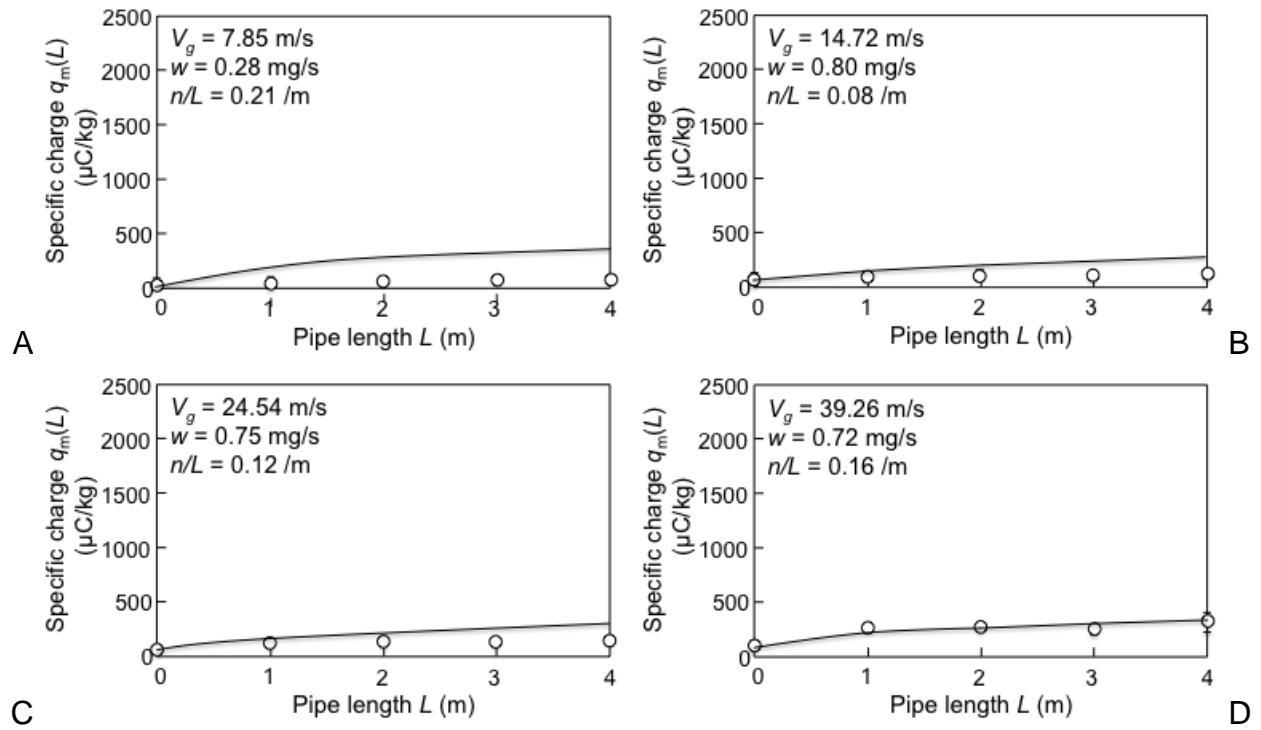


Figure D-11. Comparison for PMMA particles and Pyrex pipe for different air velocity and mass flow rate

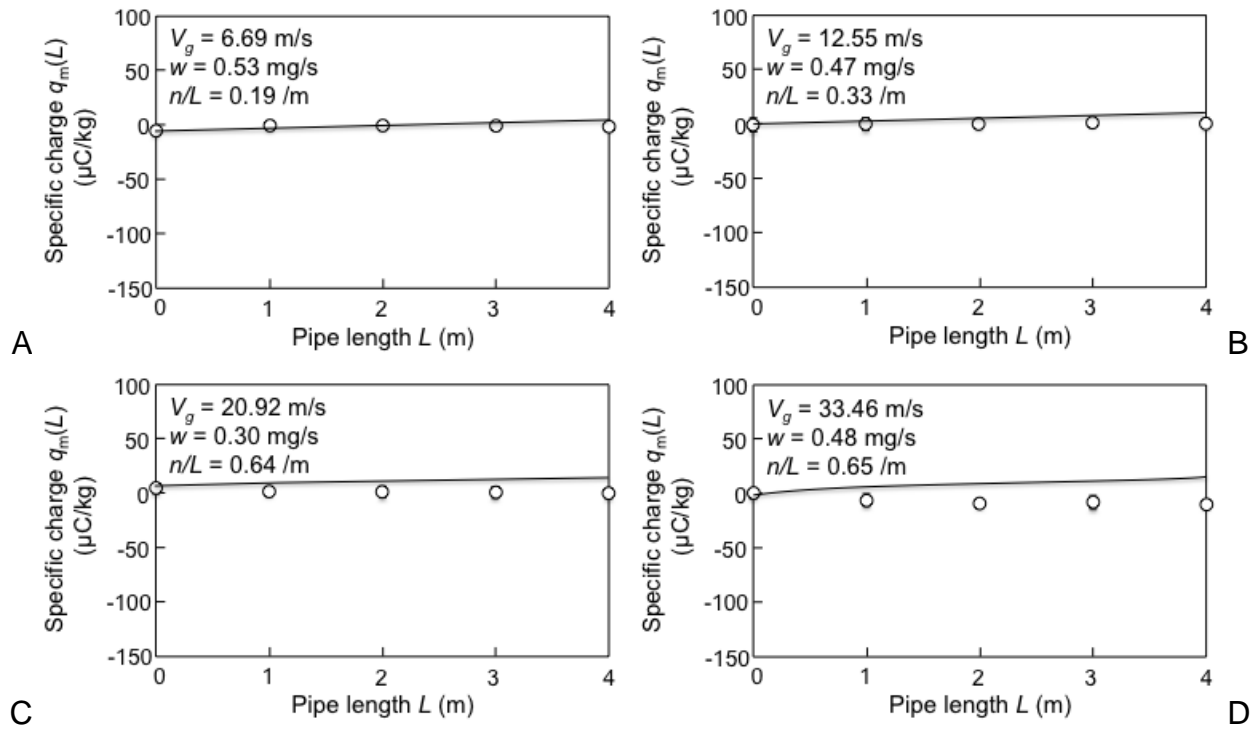


Figure D-12. Comparison for crushed soda lime particles and copper pipe for different air velocity and mass flow rate

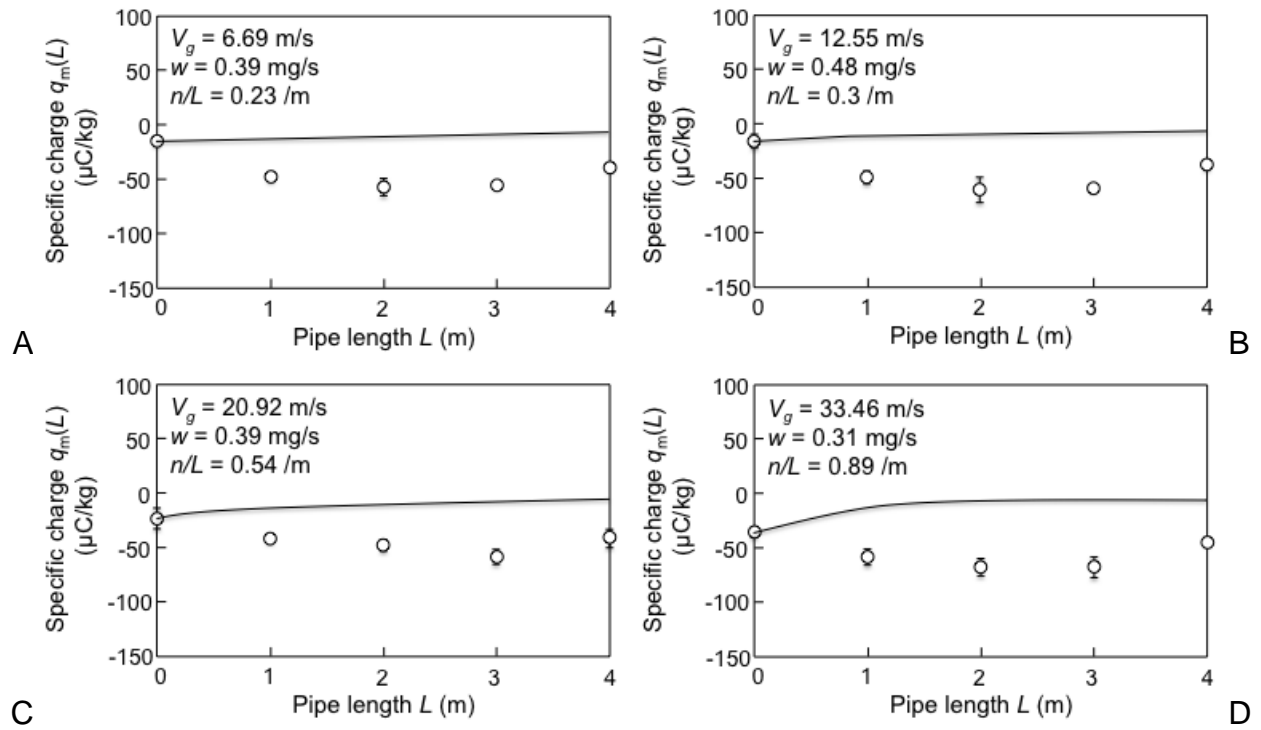


Figure D-13. Comparison for crushed soda lime particles and stainless steel pipe for different air velocity and mass flow rate

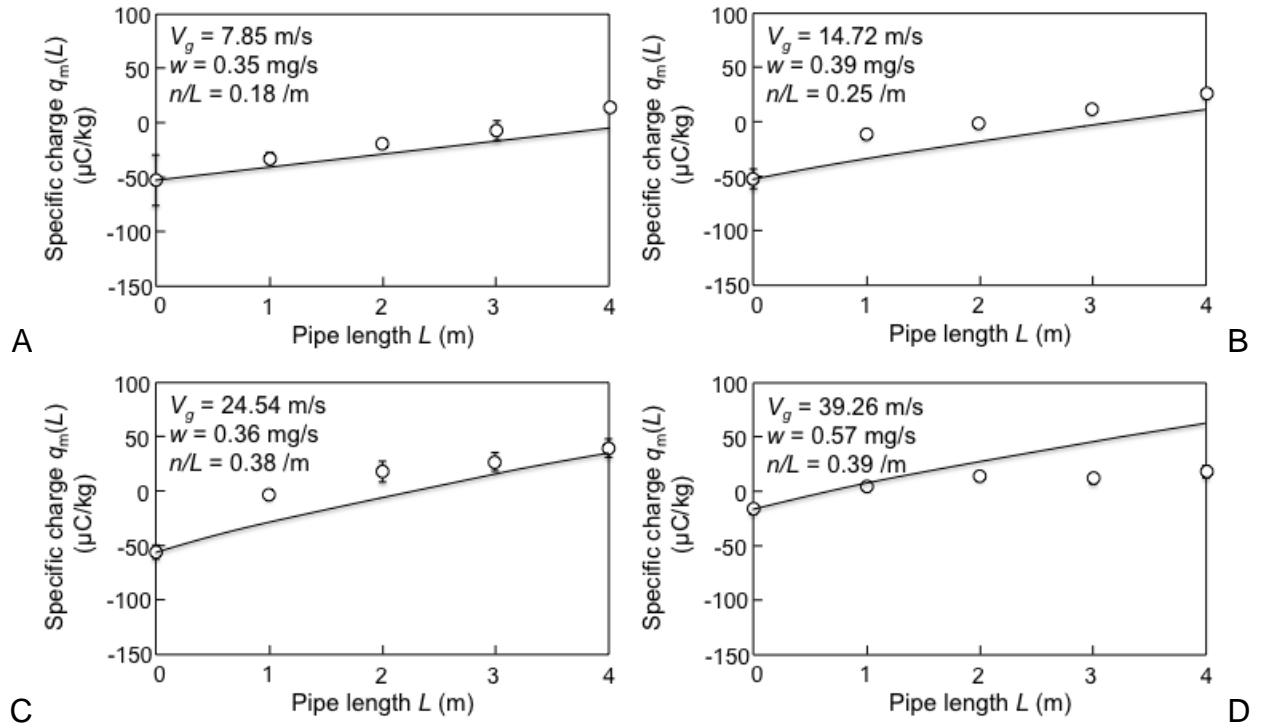


Figure D-14. Comparison for crushed soda lime particles and natural glass pipe for different air velocity and mass flow rate

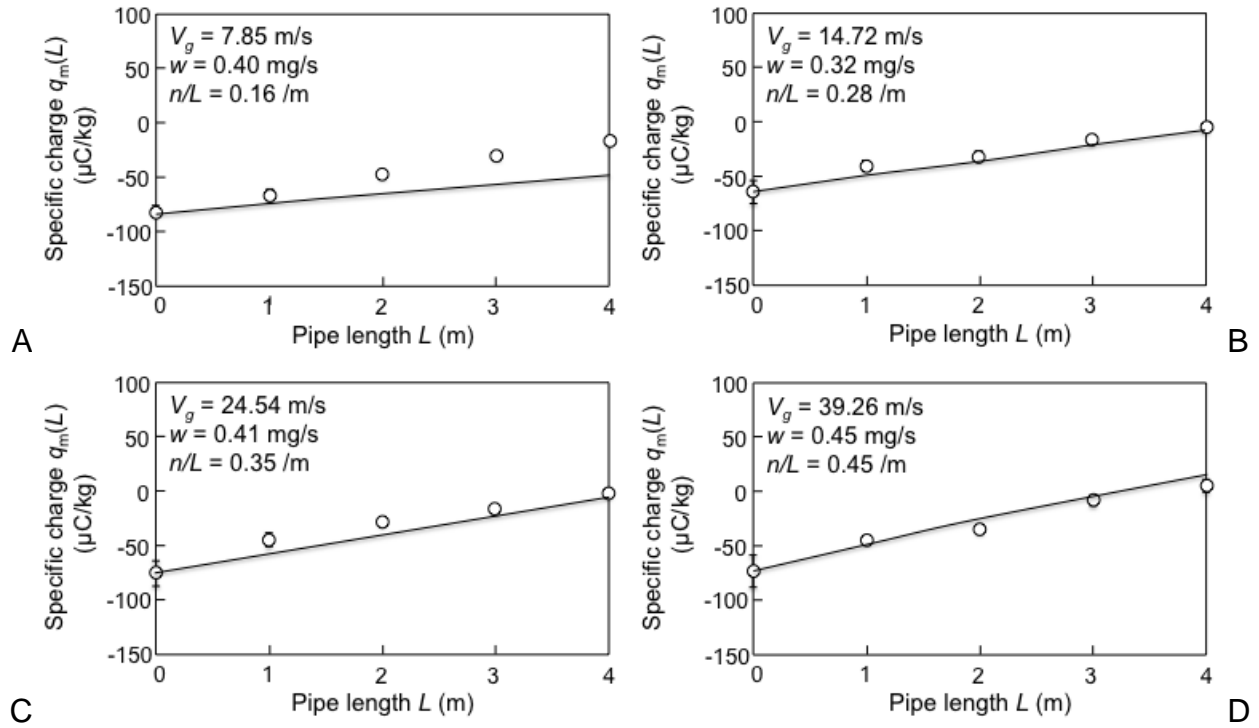


Figure D-15. Comparison for crushed soda lime particles and Pyrex pipe for different air velocity and mass flow rate

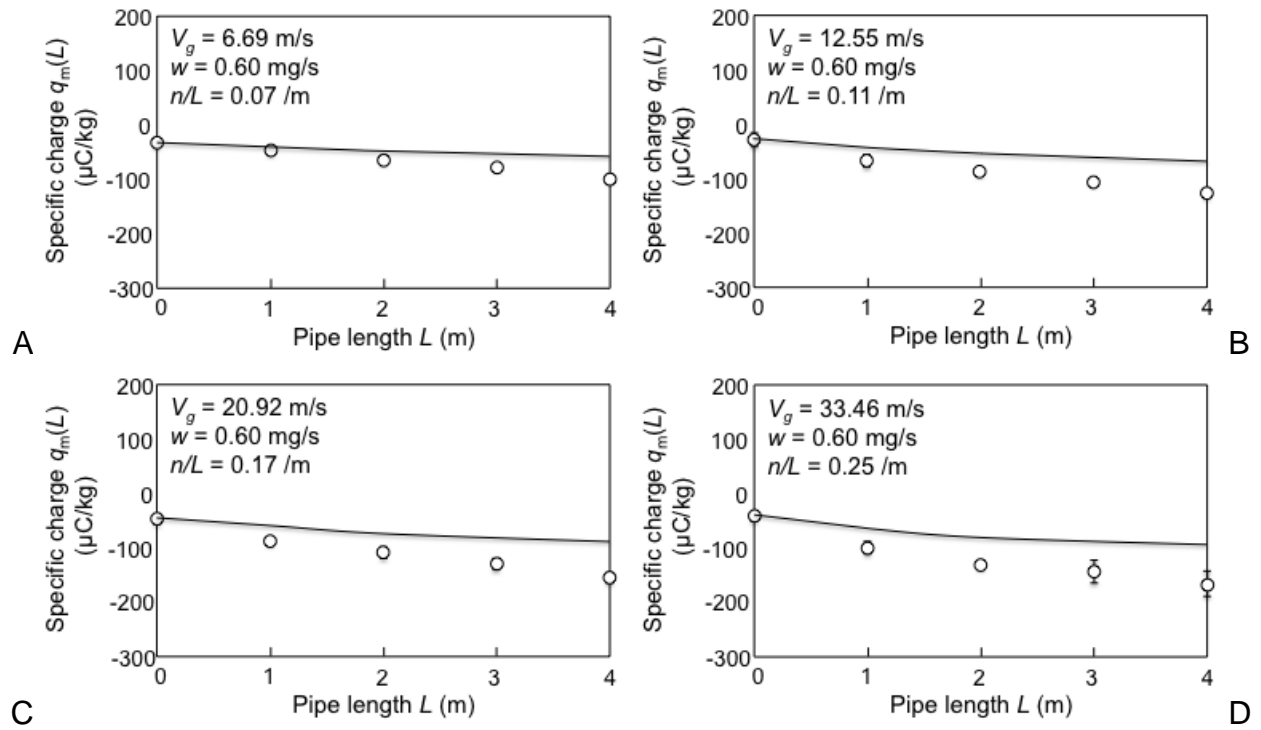


Figure D-16. Comparison for JSC-1A particles and copper pipe for different air velocity and mass flow rate

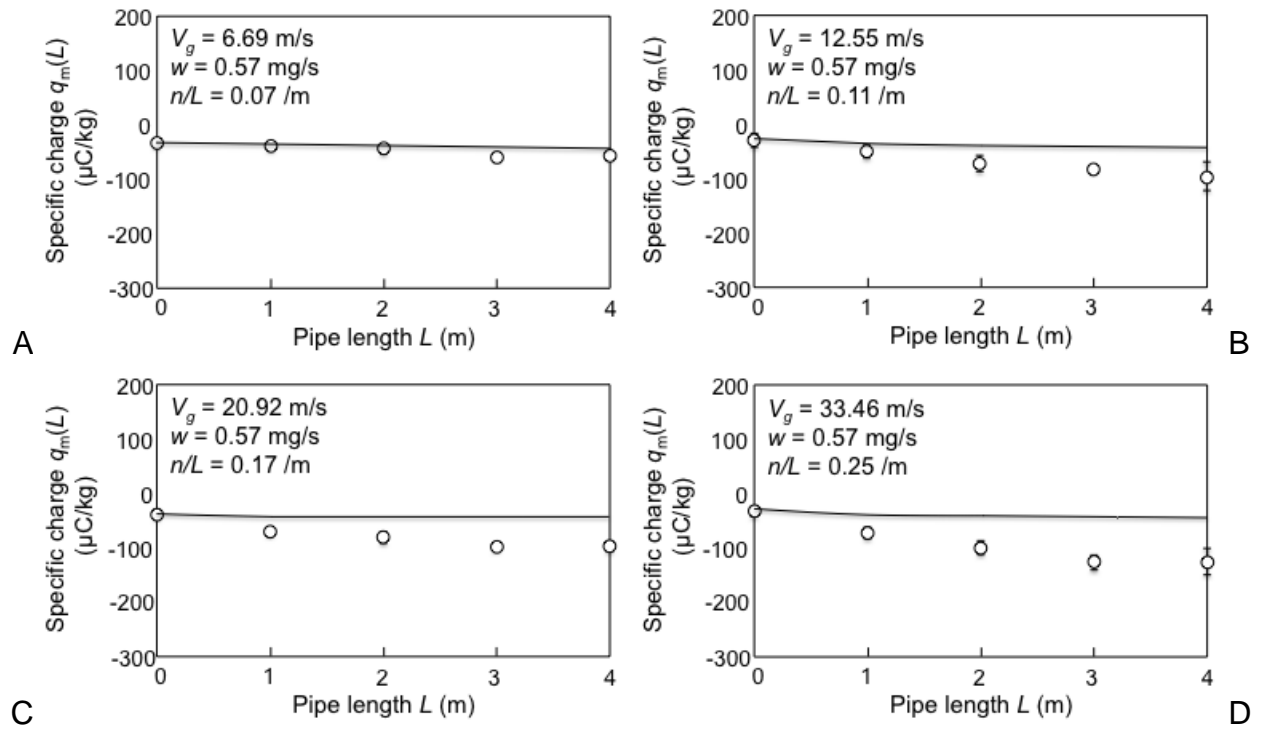


Figure D-17. Comparison for JSC-1A particles and stainless steel pipe for different air velocity and mass flow rate

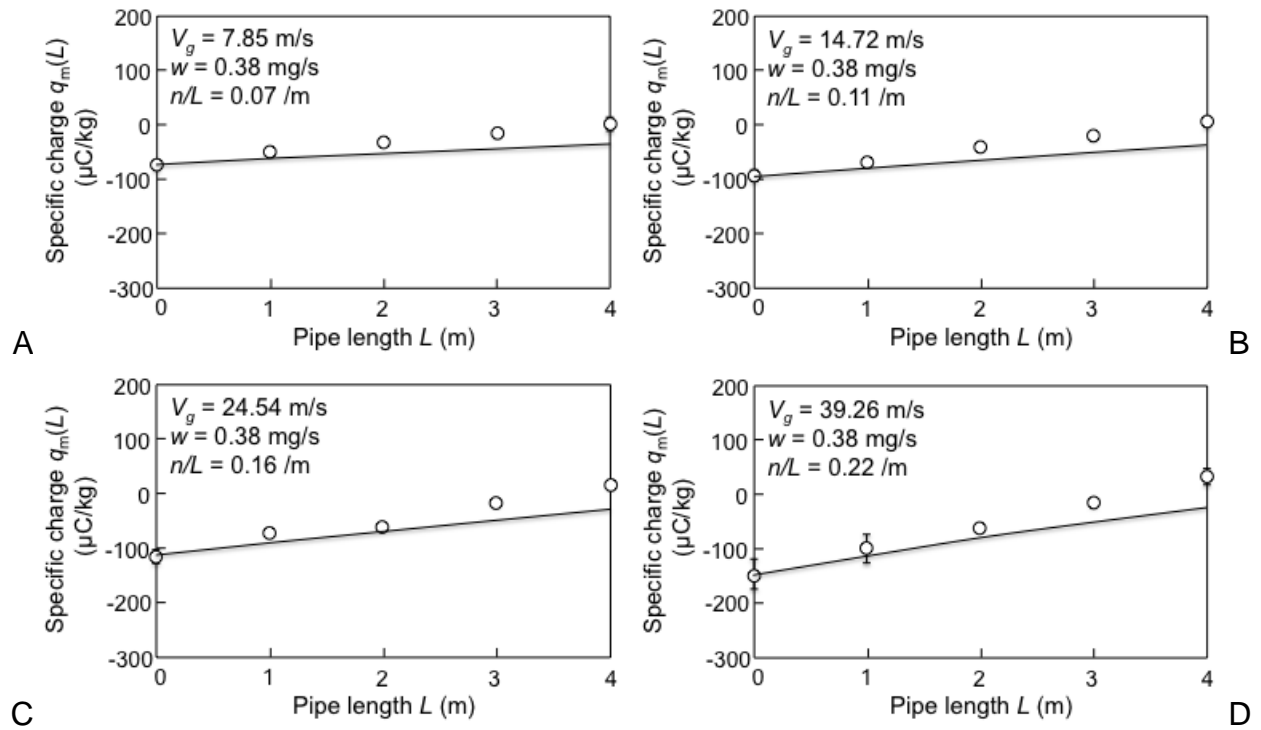


Figure D-18. Comparison for JSC-1A particles and Pyrex pipe for different air velocity and mass flow rate

APPENDIX E
ADDITIONAL IVIS IMAGES FOR DIFFERENT PARTICLE SHAPE

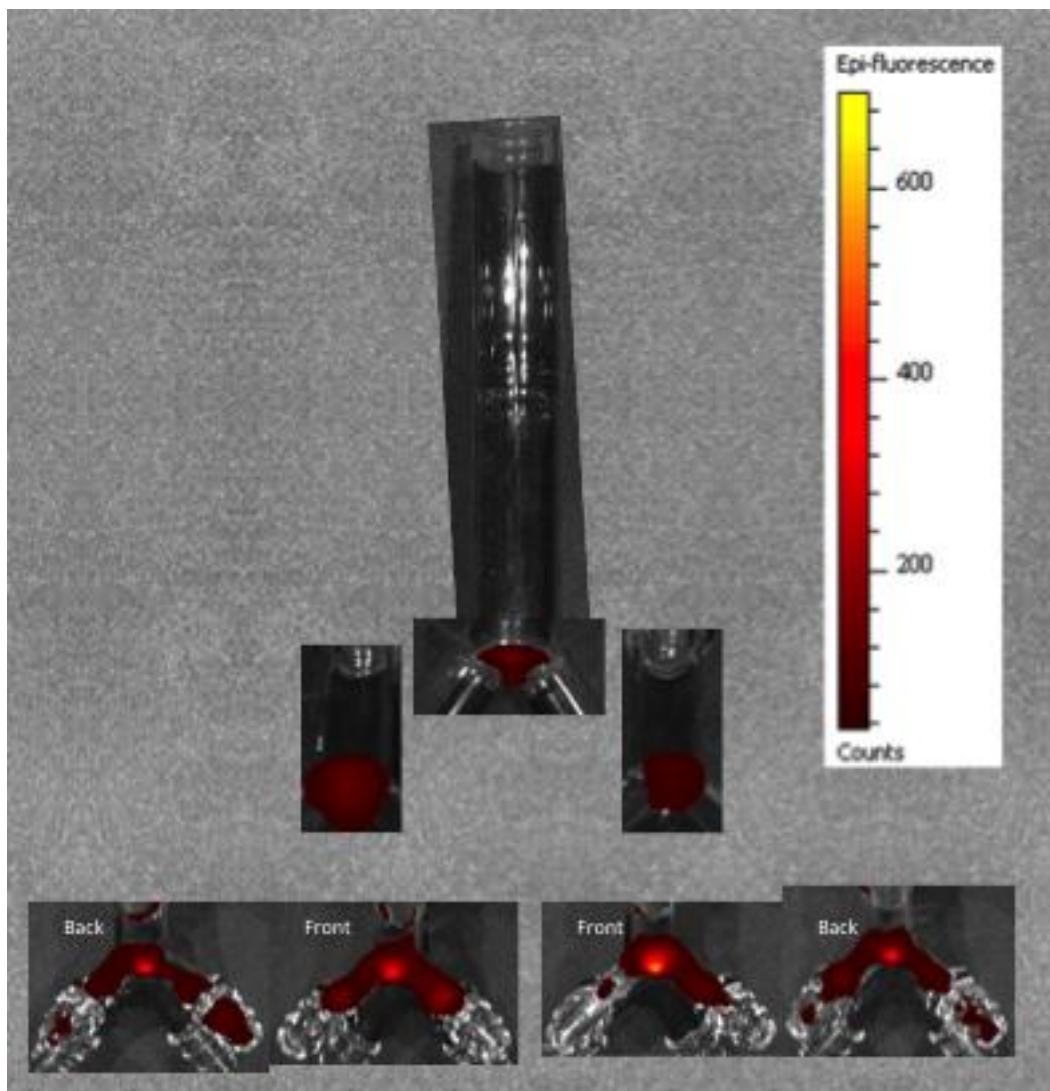


Figure E-1. IVIS Lumina images of hollow glass particles

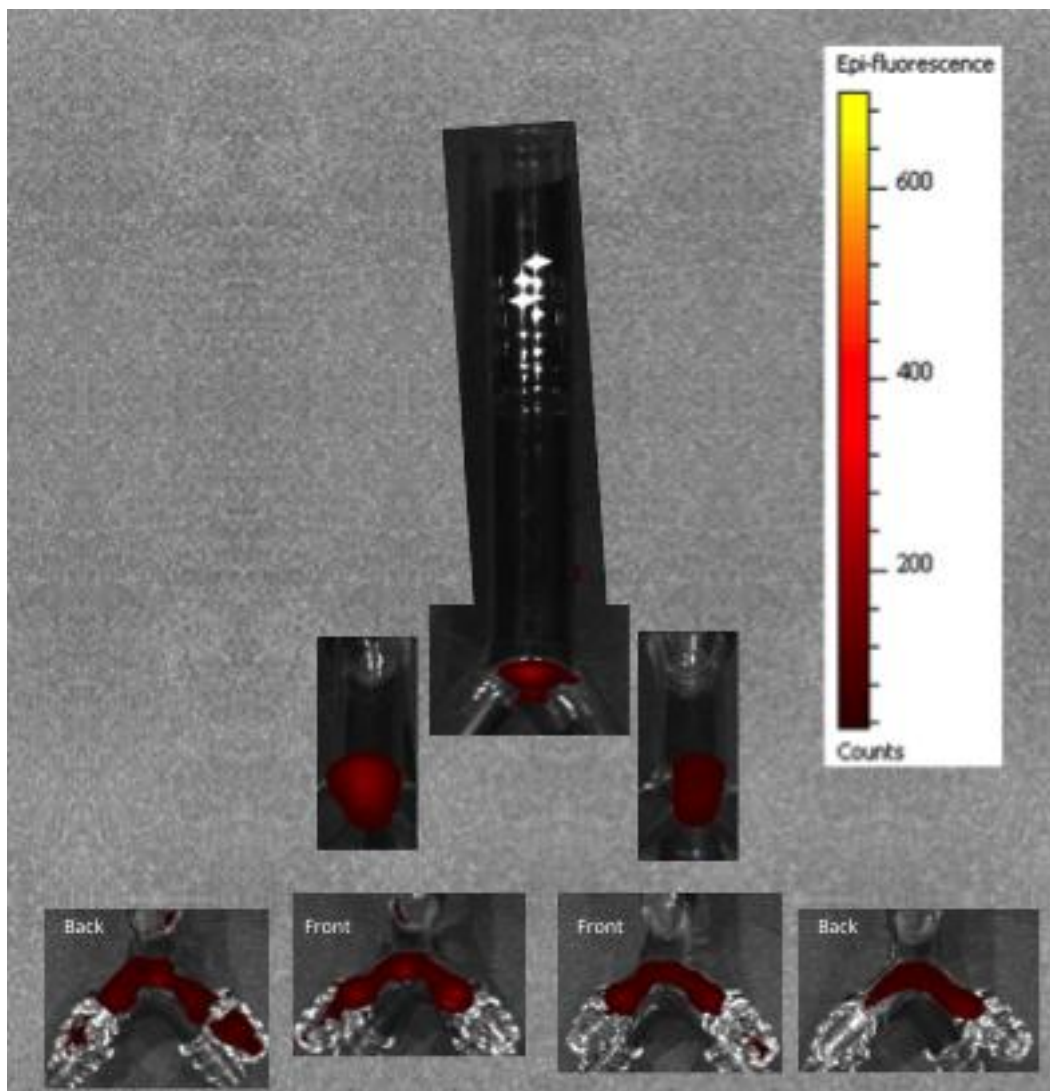


Figure E-2. IVIS Lumina images of glass rod particles

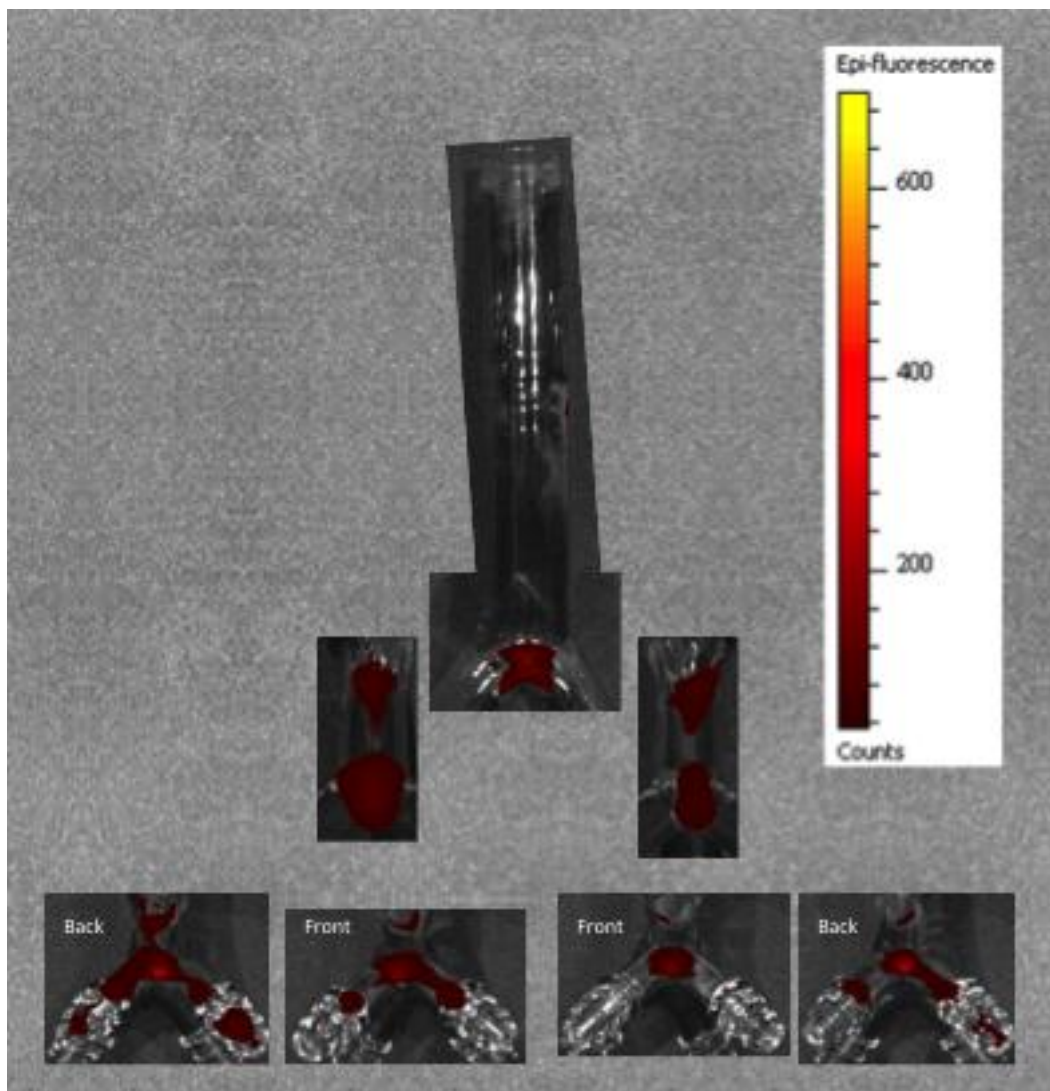


Figure E-3. IVIS Lumina images of glass flake 1 particles

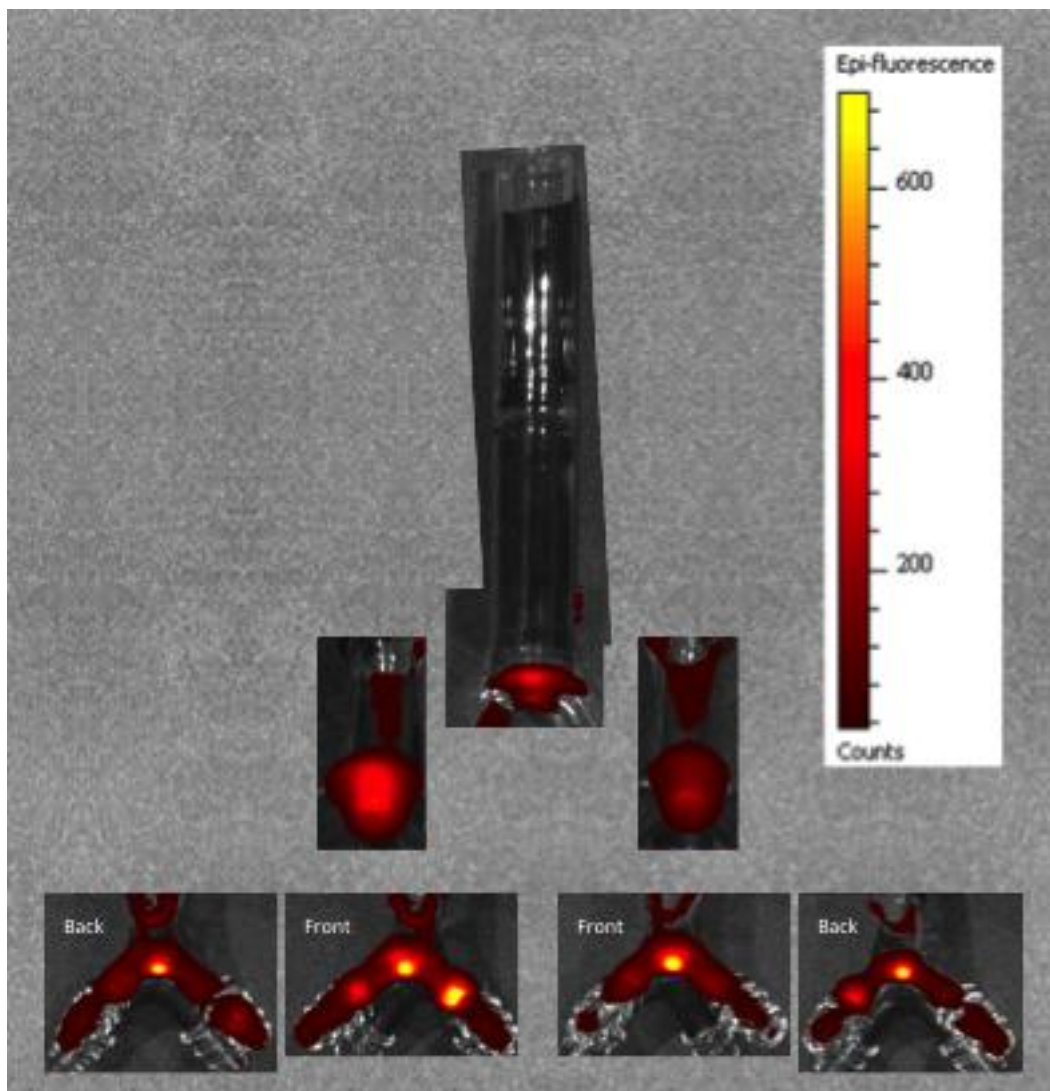


Figure E-4. IVIS Lumina images of glass flake 2 particles

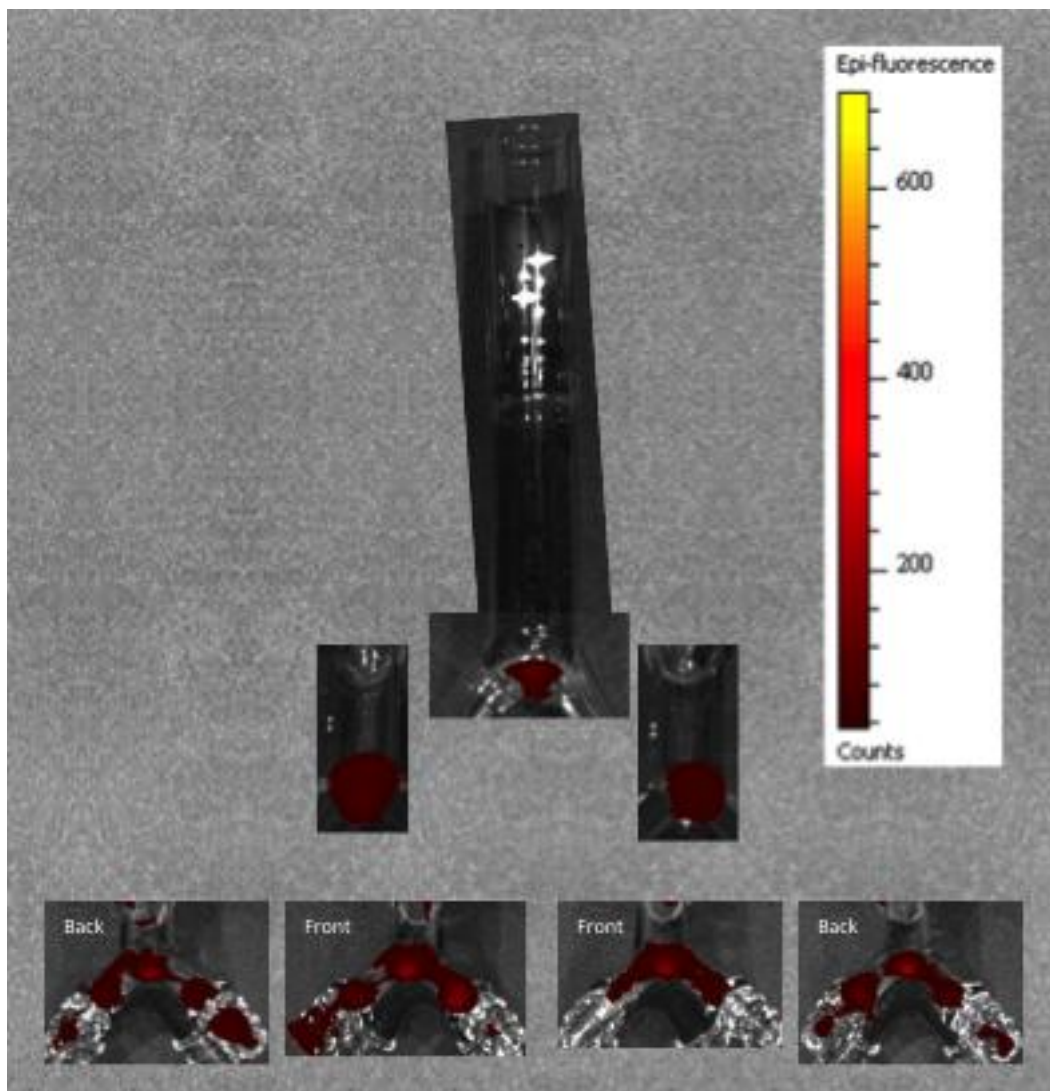


Figure E-5. IVIS Lumina images of crushed glass particles

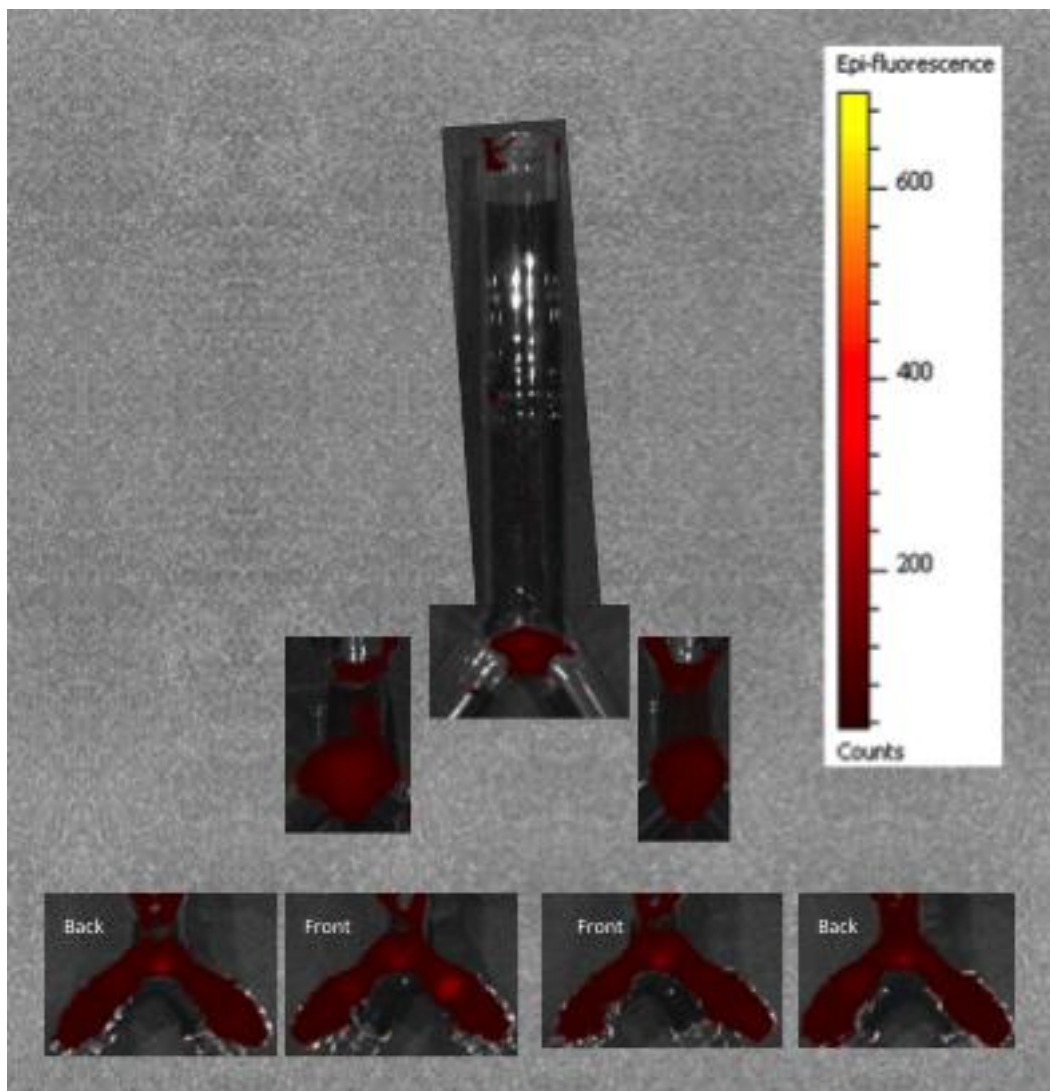


Figure E-6. IVIS Lumina images of silver flake particles

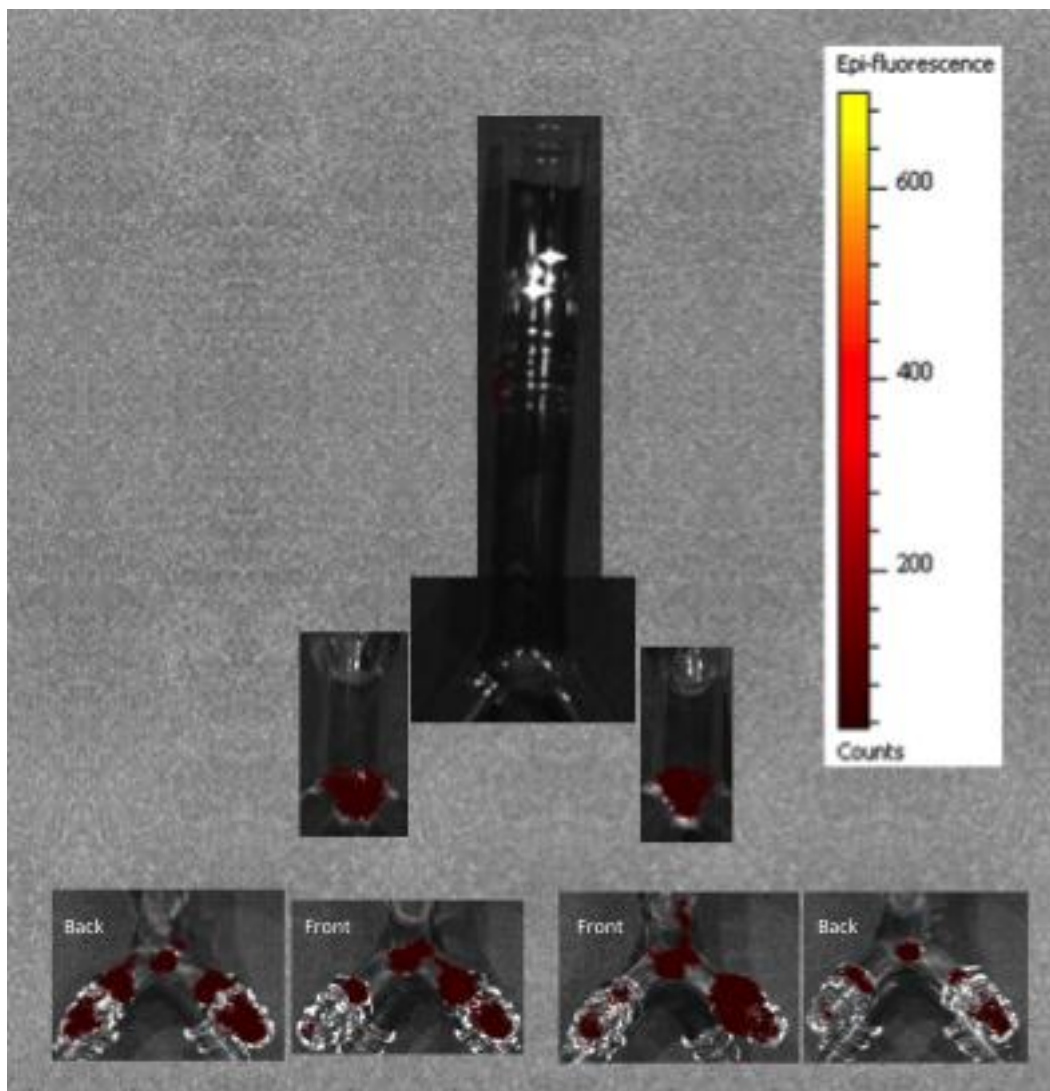


Figure E-7. IVIS Lumina images of Aluminum Oxide particles

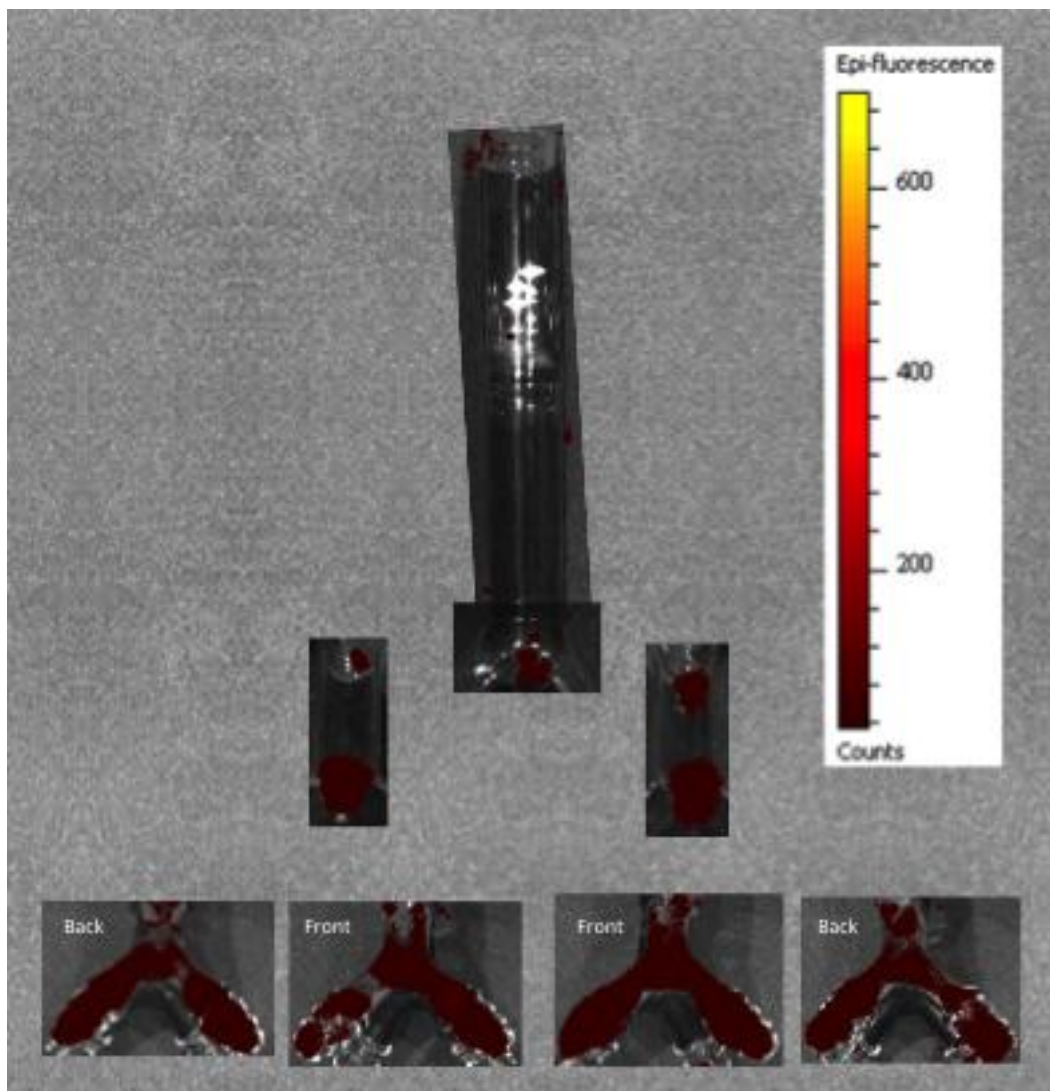


Figure E-8. IVIS Lumina images of JSC-1A particles

LIST OF REFERENCES

- Ali, M., Mazumder, M. K. and Martonen, T. B. (2009). Measurements of Electrodynamic Effect on the Deposition of MDI and DPI Aerosols in a Replica Cast of Human Oral-Pharyngeal-Laryngeal Airways, *J. Aerosol Med. Pulm. D* 22:35-44.
- Almeria, B., Deng, W., Fahmy, T. M. and Gomez, A. (2010). Controlling the Morphology of Electrospray-Generated PLGA Microparticles for Drug Delivery, *J. Colloid Interface Sci.* 343:125-133.
- Anderson, T. B. and Jackson, R. (1967). A Fluid Mechanical Description of Fluidized Bed, *Ind. Eng. Chem. Fundam.* 6:527-237.
- Bailey, A. G., Hashish, A. H. and Williams, T. J. (1998). Drug Delivery by Inhalation of Charged Particles, *J. Electrostat.* 44:3-10.
- Bhaskar, S., Pollock, K. M., Yoshida, M. and Lahann, J. (2010). Towards Designer Microparticles: Simultaneous Control of Anisotropy, Shape, and Size, *Small* 6:404-411.
- Bolio, E., Yasuna, J. and Sinclair, J. (1995). Diluted Turbulent Gas-Solid Flow in Riser With Particle-Particle Interaction, *AIChE J.* 41:1375-1388.
- Brand, P., Meyer, T., Haussermann, S., Schulte, M., Scheuch, G., Bernhard, T., Sommerauer, B., Weber, N. and Griese, M. (2005). Optimum Peripheral Drug Deposition in Patients With Cystic Fibrosis, *J. Aerosol. Med.* 18:45-54.
- Brauer, H. (1980). Report on Investigations on Particle Movement in Straight Horizontal Tubes, Particle/Wall Collision and Erosion of Tubes and Tube Bends, *J. Powder Bulk Solids Technol.* 4:3-12.
- Byron, P. R., Peart, J. and Staniforth, J. N. (1997). Aerosol Electrostatics I: Properties of Fine Powders Before and After Aerosolization by Dry Powder Inhalers, *Pharm. Res.* 14:698-705.
- Cangialosi, F., Liberti, L., Notarnicola, M. and Stencel, J. (2006). Monte Carlo Simulation of Pneumatic Tribocharging in Two-Phase Flow for High-Inertia Particles, *Powder Technol.* 165:39-51.
- Cartwright, P., Singh, S., Bailey, A. G. and Rose, L. J. (1985). Electrostatic Charging Characteristics of Polyethylene Powder During Pneumatic Conveying, *IEEE T. Ind. Appl.* 1A-21:541-546.
- Castle, G. S. P. (1997). Contact Charging Between Insulators, *J. Electrostat.* 40&41:13-20.

- Champion, J. A., Katare, Y. K. and Mitragotri, S. (2007). Particle Shape: A New Design Parameter for Micro- and Nanoscale Drug Delivery Carriers, *J. Control Release* 121:3-9.
- Chan, T. L., Lippmann, M., Cohen, V. R. and Schlesinger, R. B. (1978). Effect of Electrostatic Charges on Particle Deposition in a Hollow Cast of the Human Larynx-Tracheobronchial Tree, *J. Aerosol Sci.* 9:463-468.
- Chan, T. L., Schreck, R. M. and Lippmann, M. (1980). Effects of the Laryngeal Jet on Particle Deposition in the Human Trachea and Upper Bronchial Airways, *J. Aerosol Sci.* 11:447-459.
- Davies, C. N. (1973). Diffusion and Sedimentation of Aerosol Particles from Poiseuille Flow in Pipes, *J. Aerosol Sci.* 4:117-128.
- Deng, X., Chen, D. and Yang, W. (2011). Study on Electrodynamic Sensor of Multi-Modality System for Multiphase Flow Measurement, *Rev. Sci. Instrum.* 82:124701.
- Eckhoff, R. K. (2011). Are Enhanced Dust Explosion Hazards to be Foreseen in Production, Processing and Handling of Powders Consisting of Nano-Size Particles, in *Nanosafe 2010: International conference on safe production and use of nano materials*, J. Phys: Conf. Ser. 304.
- Edwards, D. A., Hanes, J., Caponetti, G., Hrkach, J., Ben-Jebria, A., Eskew, M. L., Mintzes, J., Deaver, D., Lotan, N. and Langer, R. (1997). Large Porous Particles for Pulmonary Drug Delivery, *Science* 276:1868-1871.
- Eggels, J. G. M., Unger, F., Weise, M. H., Adrian, R. J., Friedrich, R. and Nieuwstadt, F. T. M. (1994). Fully Developed Turbulent Pipe Flow: A Comparison Between Direct Numerical Simulation and Experiment, *J. Fluid. Mech.* 268:172-209.
- Ema, A., Yasuda, D., Tanoue, K. and Masuda, H. (2003). Tribo-Charge and Rebound Characteristics of Particles on Inclined or Rotating Metal Target, *Powder. Technol.* 135-136:2-13.
- Emmett, P., C., Aitken, R. J. and Hannan, W. J. (1982). Measurements of the Total and Regional Deposition of Inhaled Particles in the Human Respiratory Tract, *J. Aerosol Sci.* 13:549-560.
- Farkas, A. and Balashazy, I. (2007). Simulation of the Effect of Local Obstructions and Blockage on Airflow and Aerosol Deposition in Centralhuman Airways, *J. Aerosol Sci.* 38:865-884.
- Ferin, J., Mercer, T. T. and Leach, L. J. (1983). The Effect of Aerosol Charge on the Deposition and Clearance of TiO₂ Particles in Rats, *Environ. Res.* 31:148-151.

- Forward, K. M., Lacks, D. J. and Sankaran, R. M. (2009). Triboelectric Charging of Granular Insulator Mixtures Due Solely To Particle-Particle Interactions, *Ind. Eng. Chem. Res.* 48:2309-2314.
- Gajewski, J. B. and Szaynok, A. (1981). Charge Measurement of Dust Particles in Motion, *J. Electrostat.* 10:229-234.
- Gajewski, J. B. (1996). Electrostatic, Inductive Ring Probe Bandwidth, *Meas. Sci. Technol.* 7:1766-1775.
- Gajewski, J. B. (1997). Electric Charge Measurement in Pneumatic Installations, *J. Electrostat.* 40&41:231-236.
- Gajewski, J. B. (2006). Non-Contact Electrostatic Flow Probes for Measuring the Flow Rate and Charge in the Two Phase Gas-Solid Flows, *Chem. Eng. Sci.* 61:2262-2270.
- Gawronski, R. and Szewczyk, K. W. (1986). Inertial Deposition of Particles in the Human Branching Airways, *J. Aerosol. Sci.* 17:795-801.
- Geng, Y., Dalhaimer, P., Cai, S., Tsai, R., Tewari, M., Minko, T. and Discher, D. E. (2007). Shape Effects of Filaments Versus Spherical Particles in Flow and Drug Delivery, *Nat. Nanotechnol.* 2:249-255.
- Glor, M. (1985). Hazards Due To Electrostatic Charging of Powders, *J. Electrostat.* 16:175-191.
- Gondret, P., Lance, M. and Petit, L. (2002). Bouncing Motion of Spherical Particles in Fluids, *Phys. Fluids* 14:643-652.
- Haider, A. and Levenspiel, O. (1989). Drag Coefficient and Terminal Velocity of Sphere and Non-Spherical Particles, *Powder Technol.* 58:63-70.
- Hartman, R. P. A. (1998). Electrohydrodynamic Atomization in the Cone-Jet Mode. From Physical Modeling to Powder Production, in *Applied Sciences*, Delf University of Technology, Delft, The Netherlands.
- Hassan, M. S. and Lau, R. W. M. (2009). Effect of Particle Shape on Dry Particle Inhalation: Study of Flowability, Aerosolization, and Deposition Properties, *AAOS PharmSciTech.* 10:1252-1262.
- Hinds, W. C. (1982). *Aerosol technology: Properties, behavior, and measurement of airborne particles* 2nd eds. John Wiley & Sons, New York.
- Hirst, P. H., Pitcairn, G. R., Weers, J. G., Tarara, T. E., Clark, A. R., Dellamary, L. A., Hall, G., Shorr, J. and Newman, S. P. (2002). In Vivo Lung Deposition of Hollow Porous Particles from a Pressurized Metered Dose Inhaler, *Pharm. Res.* 19:258-264.

- Howatson Tawhai, M., Pullan, A. J. and Hunter, P. J. (2000). Generation of An Anatomically Based Three-Dimensional Model of the Conducting Airways, *Ann. Biomed. Eng.* 28:793-802.
- Hsieh, D. S. T., Rhine, W. D. and Langer, R. (1983). Zero-Order Controlled-Release Polymer Matrices for Micro- and Macromolecules, *J. Pharm. Sci.* 72:17-22.
- Hu, T. T., Zhao, H., Jiang, L. C., Le, Y., Chen, J. F. and Yun, J. (2008). Engineering Pharmaceutical Fine Particles of Budesonide for Dry Powder Inhalation (DPI), *Ind. Eng. Chem. Res.* 47:9623-9627.
- Itakura, T., Masuda, H. and Ohtsuka, C. (1996). The Contact Potential Difference of Powder and the Tribo-Charge, *J. Electrostat.* 38:213-226.
- Johnson, P. and Jackson, R. (1987). Frictional-Collisional Constitutive Relations for Granular Materials with Applications to Plane Shearing, *J. Fluid Mech.* 176:67-93.
- Kaialy, W., Alhalaweh, A., Velaga, S. and Nokhodchi, A. (2011). Effect of Carrier Particle Shape on Dry Powder Inhaler Performance, *Int. J. Pharm.* 421:12-23.
- Kanazawa, S., Ohkibo, T., Nomoto, Y. and Adachi, T. (1995). Electrification of a Pipe Wall During Powder Transport, *J. Electrostat.* 35:47-54.
- Kim, C. S. and Fischer, D. M. (1999). Deposition Characteristics of Aerosol Particles in Sequentially Bifurcating Airway Models, *Aerosol Sci. Technol.* 31:198-220.
- Kwok, P. C. L., Glover, W. and Chan, H. (2005). Electrostatic Charge Characteristics of Aerosols Produced from Metered Dose Inhalers, *J. Pharm. Sci.* 94:2789-2799.
- Labiris, N. R. and Dolovich, M. B. (2003). Pulmonary Drug Delivery. Part I: Physiological Factors Affecting Therapeutic Effectiveness of Aerosolized Medications, *Br. J. Clin. Pharmacol.* 56:588-599.
- LaMarche, C. Q., Curtis, J. S. and Metzger, P. T. (2011). Permeability of JSC-1A: A Lunar Soil Simulant, *Icarus* 212:383-389.
- Laufer, J. (1954). The Structure of Turbulence in Fully Developed Pipeflow, in *NACA Report*.
- Leong, F. Y., Smith, K. A., Wang, C., Matsusaka, S. and Hua, J. (2009). Electrostatic Effects on Inertial Particle Transport in Bifurcated Tubes, *AIChE J.* 55:1390-1401.
- Lim, E. W. C., Yao, J. and Zhao, Y. (2012). Pneumatic Transport of Granular Material with Electrostatic Effects, *AIChE J.* 58:1040-1059.

- Liu, J., Rasheed, A., Dong, H., Carr, W. W., Dadmun, M. D. and Kumar, S. (2008). Electrospun Micro- and Nanostructured Polymer Particles, *Macromol. Chem. Phys.* 209:2390-2398.
- Longest, P. W., Vinchurkar, S. and Martonen, T. (2006). Transport and Deposition of Respiratory Aerosols in Models of Childhood Asthma, *J. Aerosol. Sci.* 37:1234-1257.
- Louge, M., Mastorakos, E. and Jenkins, J. (1991). The Role of Particle Collision in Pneumatic Transport, *J. Fluid Mech.* 231:345-359.
- Lun, C., Savage, S., Jeffery, D. and Chepurniy, N. (1984). Kinetic Theory of Granular Flow: In Elastic Particles in Couette Flow and Slightly Inelastic Particle in General Flow Field, *J. Fluid Mech.* 140:223-256.
- Marianecci, C., Di Marzio, L., Rinaldi, F., Carafa, M. and Alhaique, F. (2011). Pulmonary Delivery: Innovative Approaches and Perspectives, *J. Biomater. Nanobiotech.* 2:567-575.
- Marijnissen, J. C. M., Yurteri, C. U., Erven, J. and Ciach, T. (2010). Medicine Nanoparticle Production by EHDA, in *Nanoparticles in Medicine and Environment, Inhalation and Health Effects*, J. C. M. Marijnissen and L. Gradon, eds., Springer Science, 39-58.
- Masuda, H., Komatsu, T. and Inoya, K. (1972). The Static Electrification of Particles in Gas-Solid Pipe Flow, *AIChE J.* 22:558-564.
- Matsusaka, S., Ghadiri, M. and Masuda, H. (2000). Electrification of an Elastic Sphere by Repeated Impacts on a Metal Plate, *J. Phys. D: Appl. Phys.* 33:2311-2319.
- Matsusaka, S., Umemoto, H., Nishitani, M. and Masuda, H. (2002). Electrostatic Charge Distribution of Particles in Gas-Solids Pipe Flow, *J. Electrostat.* 55:81-96.
- Matsusaka, S. and Masuda, H. (2006). Simultaneous Measurement of Mass Flow Rate and Charge-To-Mass Ratio of Particles in Gas-Solids Pipe Flow, *Chem. Eng. Sci.* 61:2254-2261.
- Matsusaka, S., Oki, M. and Masuda, H. (2007). Control of Electrostatic Charge on Particles by Impact Charging, *Adv. Powder. Technol.* 19:229-244.
- Matsusaka, S., Fukuda, H., Sakura, Y., Masuda, H. and Ghadiri, M. (2008a). Analysis of Pulsating Electric Signals Generated in Gas-Solids Pipe Flow, *Chem. Eng. Sci.* 63:1353-1360.
- Matsusaka, S., Ando, K. and Tanaka, Y. (2008b). Development of Electrostatic Charge Controller for Particles in Gases Using Centrifugal Contact, *J. Soc. Powder Technol.* 45:380-386.

- Matsusaka, S., Maruyama, H., Matsuyama, T. and Ghadiri, M. (2010). Triboelectric Charging of Powders: A Review, *Chem. Eng. Sci.* 65:5781-5807.
- Matsusaka, S. (2011). Control of particle tribocharging, *KONA* 29:27-38.
- Matsuyama, T. and Yamamoto, H. (1995). Characterizing the Electrostatic Charging of Polymer Particle by Impact Charging Experiments, *Adv. Powder Technol.* 6:211-220.
- Matsuyama, T., Ogu, M., Yamamoto, H., Marijnissen, J. C. M. and Scarlett, B. (2003). Impact Charging Experiments with Single Particles of Hundred Micrometre Size, *Powder Technol.* 135-136:14-22.
- Maynard, A. D. and Kuempel, E. D. (2005). Airborne Nanostructured Particles and Occupational Health, *J. Nanopart. Res.* 7:587-614.
- Melandri, C., Tarroni, G., Prodi, V., De Zaiacomo, T., Formignani, M. and Lombardi, C. C. (1983). Deposition of Charged Particles in the Human Airways, *J. Aerosol Sci.* 14:657-669.
- Nieh, S. and Nguyen, T. (1988). Effects of Humidity, Conveying Velocity, and Particle Size on Electrostatic Charges of Glass Beads in a Gaseous Suspension Flow, *J. Electrostat.* 21:99-114.
- Oldham, M. J. (2000). Computational Fluid Dynamic Predictions and Experimental Results for Particle Deposition in an Airway Model, *Aerosol. Sci. Technol.* 32:61-71.
- Patankar, S. and Spadling, D. (1967). *Heat and Mass Transfer in Boundary Layer*. Morgan-Grampain, London.
- Pavia, D., Thomson, M. L., Clarke, S. W. and Shannon, H. S. (1977). Effect of Lung Function and Mode of Inhalation on Penetration of Aerosol into the Human Lung, *Thorax* 32:194-197.
- Peart, J., Kulphaisal, P. and Orban, J. C. (2003). Relevance of Electrostatics in Respiratory Drug Delivery, *Business Briefing: Pharmagenetics*:84-87.
- Prodi, V. and Mularoni, A. (1985). Electrostatic Lung Deposition Experiments with Humans and Animal, *Ann. Occup. Hyg.* 29:229-240.
- Rao, A., Curtis, J., S., Hancock, B. C. and Wassgres, C. (2011). Numerical Simulation of Dilute Turbulent Gas Particle Flow with Turbulence Modulation, *AIChE J.*
- Rhodes, M., ed. (2008). *Introduction to particle technology*. John Wiley & Sons Inc., Hoboken, NJ.

- Sanders, M. (2011). Pulmonary drug delivery: An historical overview, in *Controlled pulmonary drug delivery*, H. D. C. Smyth and A. J. Hickey, eds., Springer, New York, NY, 51-73.
- Schlesinger, R. B., Bohning, D. E., Chan, T. L. and Lippmann, M. (1977). Particle Deposition in a Hollow Cast of the Human Tracheobronchial Tree, *J. Aerosol. Sci.* 8:429-445.
- Sinclair, J. and Mallo, T. (1998). Describing Particle-Turbulence Interaction in a Two-Fluid Modeling Framework, in *ASME Fluid Engineering Division Summer Meeting*, ASME Press, New Yorks, 7-14.
- Smeltzer, E. E., Weaver, M. L. and Klinzing, G. E. (1982). Individual Electrostatic Particle Interaction in Pneumatic Transport, *Powder Technol.* 33:31-42.
- Sommerfield, M. and Huber, N. (1999). Experimental Analysis and Modeling of Particle-Wall Collisions, *Int. J. Multiphas. Flow* 25:1457-1489.
- Su, W. C. and Cheng, Y. C. (2009). Deposition of Man-Made Fibers in Human Respiratory Airway Casts, *J. Aerosol. Sci.* 40:270-284.
- Supuk, E., Hassanpour, A., Ahmadian, H., Ghadiri, M. and Matsuyama, T. (2011). Tribo-Electrification and Associated Segregation of Pharmaceutical Bulk Powders, *KONA* 29:208-223.
- Tanoue, K., Tanaka, H., Kitano, H. and Masuda, H. (2001). Numerical Simulation of Tribo-Electrification of Particles in a Gas-Solids Two-Phase Flow, *Powder Technol.* 118:121-129.
- Timbrell, V. (1965). The Inhalation of Fibrous Dusts, *Ann. NY Acad. Sci.* 132:255-273.
- Vercoulen, P. H. W. (1995). Electrostatic Processing of Particles. A Tool in Particle Technology, in *Applied Sciences*, Delf University of Technology, Delft, The Netherlands.
- Watanabe, H., Ghadiri, M., Matsuyama, T., Ding, Y. L., Pitt, K. G., Maruyama, H., Matsusaka, S. and Masuda, H. (2007). Triboelectrification of Pharmaceutical Powders by Particle Impact, *Int. J. Pharm.* 334:149-155.
- Watano, S., Saito, S. and Suzuki, T. (2003). Numerical Simulation of Electrostatic Charge in Powder Pneumatic Conveying Process, *Powder Technol.* 135-136:112-117.
- Weibel, E. R. (1963). *Morphometry of the Human Lung*. Springer, Berlin.
- Yao, J., Zhang, Y., Wang, C. H. and Liang, Y. C. (2006). On the Electrostatic Equilibrium of Granular Flow in Pneumatic Conveying System, *AIChE J.* 52:3775-3793.

- Zeng, X. M., Martin, G. P., Marriott, C. and Pritchard, J. (2000). The Influence of Carrier Morphology on Drug Delivery by Dry Powder Inhalers, *Int. J. Pharm.* 200:93-106.
- Zhang, Z. and Kleinstreuer, C. (2001). Effect of Particle Inlet Distributions on Deposition in a Triple Bifurcation Lung Airway Model, *J. Aerosol Med.* 14:13-29.

BIOGRAPHICAL SKETCH

Pongpumin Poom Bunchatheervate was born in Bangkok, Thailand in 1998. He later move o Kentucky, USA. It was in Kentucky that received his bachelor's degree in chemical engineering (2006) and his MBA (2007) at the University of Kentucky. In 2007, he joined the University of Florida to pursue his PhD in chemical engineering.